Deuteron Breakup $\vec{p}d \to (pp)n$ with a Fast Forward Diproton Studied at ANKE–COSY

Den Naturwissenschaftlichen Fakultäten
der Friedrich–Alexander–Universität Erlangen–Nürnberg
zur
Erlangung des Doktorgrades

vorgelegt von
Sergey Yashchenko
aus Wolgograd, Russland

Als Dissertation genehmigt von den Naturwissenschaftlichen
Fakultäten der Universität Erlangen–Nürnberg

Tag der mündlichen Prüfung:	26.07.2004
Vorsitzender der Promotionskommision:	Prof. Dr. L. Dahlenburg
Erstberichterstatter:	Prof. Dr. E. Steffens
Zweitberichterstatter:	Prof. Dr. H. Ströher

Abstract

In the framework of this thesis the first measurements of the differential cross section and the vector analyzing power of the deuteron breakup reaction $pd \to (pp)n$ with emission of a fast forward proton pair (diproton) have been carried out. The physics motivation, the experimental setup, the data analysis procedures, the experimental results and their comparison with theoretical predictions are presented.

The deuteron breakup reaction $pd \to ppn$ at GeV projectile energies in kinematics similar to backward elastic scattering $pd \to dp$ provides a new tool to investigate the short–range NN interaction and the pd dynamics at high–momentum transfer. It is the aim of the experimental program at the ANKE spectrometer at COSY–Jülich to obtain insight into nuclear systems composed of more than two nucleons by providing a complete set of observables.

An exclusive measurement of the $pd \to (pp)n$ reaction with forward emission of a fast proton pair with small excitation energy $E_{pp} < 3$ MeV has been performed at ANKE. The experiment was carried out with a deuterium cluster jet target at the internal beam of COSY at energies $T_p = 0.6$, 0.7, 0.8, 0.95, 1.35, and 1.9 GeV by reconstructing the momenta of the two ejectile protons. The differential cross section of the breakup reaction, averaged from 0° to 8° over the c.m. polar angle of the total momentum of the pp pairs, has been obtained. The experimental investigation of the deuteron breakup with a fast forward diproton was stimulated by the development of a theoretical model, including one nucleon exchange, single scattering and double scattering with excitation of a Δ isobar (ONE + SS + Δ), previously applied to the $pd \to dp$ process. However, the measured cross section only at $T_p = 0.6$–0.7 GeV is reproduced by this model when the Reid soft core or Paris potential is used. Recently, it was shown that the use of the CD Bonn potential results in a much better agreement between data and theory in the full energy range $T_p = 0.6$–1.9 GeV.

In addition, a first experiment with the polarized proton beam has been carried out at ANKE for two beam energies $T_p = 0.5$ and 0.8 GeV with the aim to measure the vector analyzing power A_y^p of the deuteron breakup reaction $\vec{p}d \to (pp)n$. The concurrent measurement of the asymmetry in small angle $\vec{p}d$ elastic scattering allowed us to determine the beam polarization. The angular dependence of A_y^p was deduced for the neutron emission angle $\theta_n^{c.m.} = 166°$ to 180°. At 0.5 GeV a large analyzing power was observed for neutron emission angles around $\theta_n^{c.m.} = 166°$, while at 0.8 GeV

A_y^p vanishes. This behavior of A_y^p differs from that of *pd* backward elastic scattering. Although the ONE+SS+Δ model reproduces the sign of A_y^p and the fast decrease from 0.5 to 0.8 GeV, the model significantly underpredicts the observed maximum of A_y^p.

A more critical test of the theoretical approach is expected in a measurement of the tensor analyzing power. This aim can be achieved with the polarized internal storage cell deuterium gas target which is being installed at ANKE.

Zusammenfassung

Im Rahmen der vorgelegten Doktorarbeit wurden die ersten Messungen des differentiellen Wirkungsquerschnitts und der Vektoranalysierstärke der Deuteronen–Aufbruchsreaktion $pd \to (pp)n$ durchgeführt. Die untersuchte Reaktion ist gekennzeichnet durch die Emission eines Paars schneller Protonen, eines Di–Protons, in Vorwärtsrichtung. Der theoretische Hintergrund, der experimentelle Aufbau und die Verfahren der Datenanalyse werden dargelegt. Die experimentellen Ergebnisse werden diskutiert und mit den Ergebnissen theoretischer Modellvorhersagen verglichen.

Die Deuteronen–Aufbruchsreaktion $pd \to ppn$, in der Kinematik ähnlich derjenigen bei der elastischen Rückwärtsstreuung $pd \to dp$, eröffnet bei Projektilenergien von GeV einen neuen Weg, die kurzreichweitige Nukleon–Nukleon–Wechselwirkung und die pd–Dynamik bei hohem Impulsübertrag zu untersuchen. Das experimentelle Programm am Spektrometer ANKE, installiert als interne Einrichtung an der Beschleunigeranlage COSY–Jülich, zielt darauf ab, durch die Gewinnung von vollständigen Sätzen von Observablen Einsicht in Systeme mit mehr als zwei Nukleonen zu gewinnen.

Eine zur Bestimmung der Wechselwirkungskinematik vollständige Messung zu der Reaktion $pd \to (pp)n$ mit Vorwärtsemission eines schnellen Protonenpaars kleiner Anregungsenergie $E_{pp} < 3$ MeV wurde am Magnetspektrometer ANKE durchgeführt. Die Untersuchungen wurden mit dem Clusterstrahl–Target am internen Strahl von COSY bei Strahlenergien $T_p = 0.6$, 0.7, 0.8, 0.95, 1.35 und 1.9 GeV durchgeführt. Aus den gewonnenen Daten wurden die Impulse der beiden Ejektil–Protonen ermittelt. Der differentielle Wirkungsquerschnitt der Aufbruchsreaktion, gemittelt über den Polarwinkelbereich 0° bis 8° des Gesamtimpulses des Protonenpaars im Schwerpunktsystem, wurde bestimmt. Die experimentelle Untersuchungen des Deuteronen–Aufbruchs mit Emission eines schnellen Di–Protons wurde angeregt durch neuere Entwicklungen des theoretischen Modells, das ehemals unter Berücksichtigung von 1–Nukleon–Austausch (ONE), Einzelstreuung (SS) sowie Doppelstreuung mit Anregung eines Δ–Isobars — daher bekannt als (ONE+SS+Δ)–Modell — zur Beschreibung des Prozesses $pd \to dp$ verwandt wurde. Durch dieses Modell wird der in der vorgelegten Arbeit erhaltene Wirkungsquerschnitt jedoch nur im Bereich $T_p = 0.6$–0.7 GeV richtig wiedergegeben, solange das Reid–Soft–Core– oder das Paris–Potential benützt wird. Kürzlich wurde gezeigt, daß mit dem Potential CD–Bonn eine wesent-

lich bessere übereinstimmung über den gesamten Energiebereich $T_p = 0.6$–1.9 GeV erzielt wird.

Weiterhin wurde am Spektrometer ANKE ein erstes Experiment mit dem polarisierten Protonenstrahl bei $T_p = 0.5$ und $T_p = 0.8$ GeV durchgeführt mit dem Ziel, die Vektoranalysierstärke A_y^p der Deuteronen–Aufbruchsreaktion $\vec{p}d \to (pp)n$ zu bestimmen. Die gleichzeitig gewonnenen Daten zur Asymmetrie in der elastischen $\vec{p}d$–Streuung bei kleinen Winkeln erlaubten die Bestimmung der Strahlpolarisation. Die Winkelabhängigkeit von A_y^p wurde bestimmt für einen Winkelbereich des Protonenpaares, der Emissionswinkeln des nicht nachgewiesenen Neutrons im Schwerpunktsystem von $\theta_n^{c.m.} = 166°$ bis $180°$ entspricht. Bei $T_p = 0.5$ GeV wurde im Bereich um $\theta_n^{c.m.} = 166°$ ein großer Wert der Analysierstärke A_y^p gemessen, während diese bei $T_p = 0.8$ GeV einen verschwindend kleinen Wert annimmt. Dieses Verhalten von A_y^p weicht ab von dem, das bei der elastischen pd–Rückwärtsstreuung beobachtet wurde. Während das (ONE+SS+Δ)–Modell das Vorzeichen von A_y^p und das starke Absinken von $T_p = 0.5$ GeV nach $T_p = 0.8$ GeV richtig vorhersagt, liegt die Vorhersage des Absolutwerts signifikant unter dem gemessenen Maximalwert.

Ein weiterer und kritischerer Test der theoretischen Herangehensweise ist zu erwarten aus der Messung der Tensoranalysierstärke. Dieses Ziel kann erreicht werden unter Einsatz des polarisierten Speicherzellen–Deuterium–Gastargets, dessen Einsatz am Spektrometer ANKE in Vorbereitung ist.

Contents

1. Physics Motivation

The structure of the lightest nuclei at short distances $r_{NN} < 0.5$ fm, i.e. at high relative momenta $q_{NN} \sim 1/r_{NN} > 0.4$ GeV/c between the nucleons, and the NN interaction in the nucleon overlap region are fundamental problems of nuclear physics. Experimentally, these problems can be studied in processes with high momenta transferred to the nucleus $Q \geq 1$ GeV/c. Electromagnetic probes are considered as the cleanest instruments for such studies [1, 2]. In particular, the deuteron as the only $A = 2$ particle was intensively investigated in reactions with electron and photon beams. The existing data on elastic electromagnetic form factors of the deuteron at $Q \leq 1$ GeV/c are in reasonable agreement with the conventional nuclear model, in which nuclei and nuclear interactions are explained as baryons interacting through the exchange of mesons. The situation becomes much less clear for $Q \geq 1$ GeV/c because of the increasing contribution from meson–exchange currents (MEC) in *ed* interactions and theoretical uncertainties in their treatment. Moreover, the conventional nuclear model fails to explain the data on photo disintegration $\gamma d \to np$ at photon energies $E_\gamma \geq 1$ GeV. It seems that the interactions at short distances well below the size of the nucleon require explicit consideration of the quark substructure of the nucleons. The reactions with hadronic probes at high momentum transfer can be considered as a complementary tool in the investigation of short–distance phenomena and as a source of information unavailable in electromagnetic reactions. The investigation of nucleon resonances, the check of non–relativistic effective models, of meson–nucleon theories, and of NN potentials are very interesting in this context.

1.1 Backward Elastic *pd* Scattering

One of the simplest hadronic processes with a high momentum transfer already at intermediate energies is the *pd* backward elastic scattering. For this reason *pd* backward elastic scattering has been studied intensively from theoretical and experimental sides with the aim to extract information about the dynamics of high–momentum transfer in few-nucleon systems and about the short–range structure of the NN interaction. Concepts have been discussed as e.g. the one nucleon exchange (ONE), the presence of nucleon resonances (N^*) inside the deuteron [3], the importance of virtual pions [4], and three–baryon resonances [5].

Only at low energies, where the ONE mechanism dominates, the differential cross section, the tensor analyzing power T_{20}, and the spin transfer coefficient κ are reasonably well described [4–8]. At higher energies, where internal momenta above 0.3 GeV/c are probed in the deuteron, the dynamics becomes more complicated because of the possible excitation of N^* and Δ resonances in the intermediate states. These effects are taken into account to some extent in the one pion exchange model, but adding the ONE amplitude causes the problem of double counting [4, 11, 12]. The excitation of the $\Delta(1232)$ resonance in the intermediate state (Δ mechanism) is explicitly included in a model [5, 7], which also takes into account coherently ONE and single pN scattering (SS) in a consistent way [13] (Fig. 1.1).

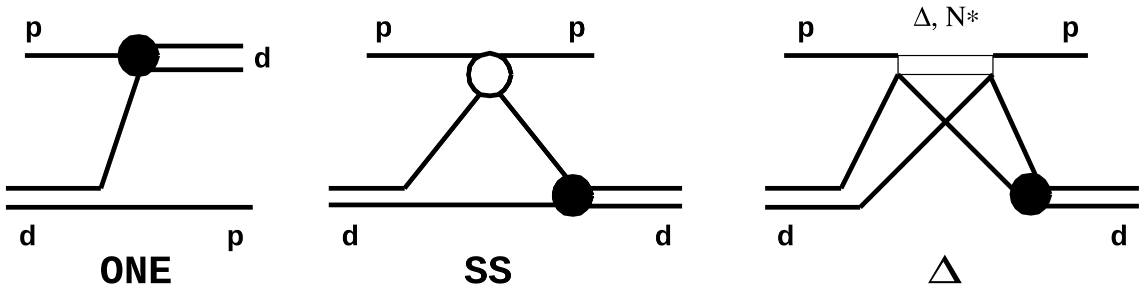

Figure 1.1: Mechanisms included in the ONE+SS+Δ model for the $pd \to dp$ process [13].

This model, improved in Ref. [13] with respect to the Δ contribution through the analysis of $pp \to pn\pi^+$ data [14], describes the gross features of the $pd \to dp$ spin–averaged differential cross section. After further refinement also the tensor analyzing power at beam energies below 0.5 GeV is reproduced qualitatively [7]. Above the region, where the $\Delta(1232)$ dominates, the role of intermediate excitations of heavier baryon resonances is expected to increase. This makes the theoretical interpretation of this process much more ambiguous. These three–body effects are similar to MEC in electromagnetic processes and have similar uncertainties.

1.2 Deuteron Breakup $pd \to (pp)n$ with Emission of a Fast Proton Pair

In view of the above mentioned complications, it would be very important to study a process, where contributions from the N^* and Δ resonance excitation are suppressed.

For that purpose, an appropriate reaction is the deuteron breakup

$$p + d \to (pp) + n$$

with emission of the two protons (diproton) in forward direction ($\theta_{pp} \approx 0°$) at low excitation energy $E_{pp} < 3$ MeV (see Appendix A for description of the deuteron breakup kinematics). With the neutron emitted backward, the kinematics of this reaction is quite close to that of pd backward elastic scattering. Therefore, the same mechanisms can be applied in the analysis of both processes. They are shown in Fig. 1.2.

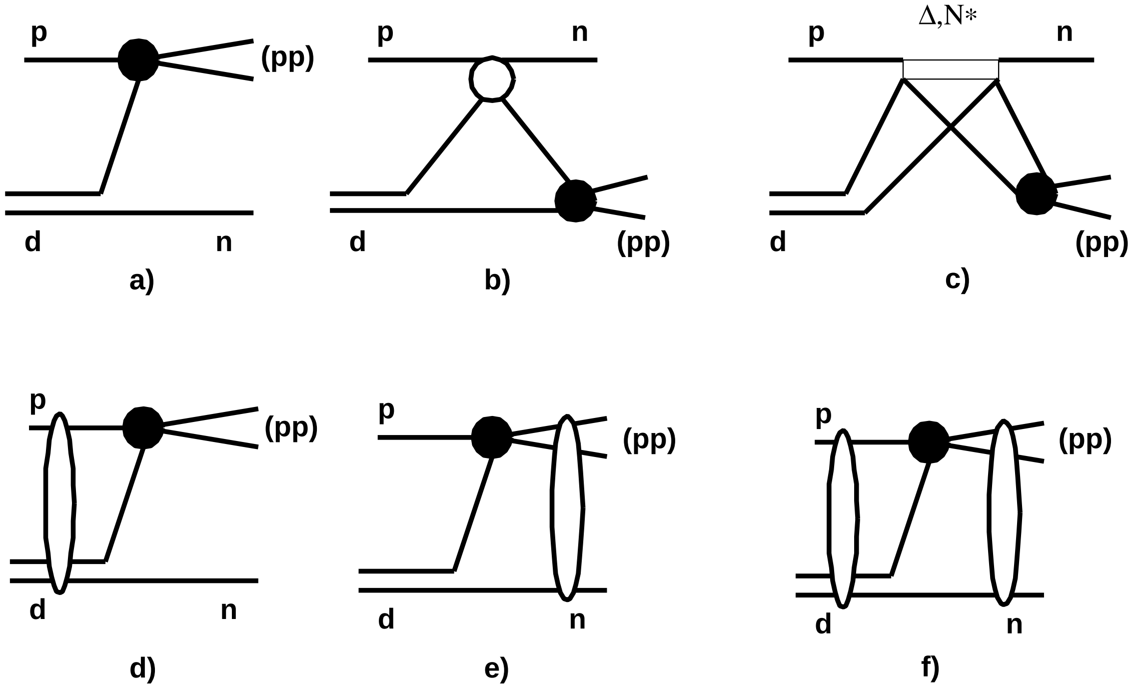

Figure 1.2: Mechanisms of the reaction $pd \to (pp)n$: (a) — one nucleon exchange (ONE), (b) — single scattering (SS), (c) — double pN scattering (Δ) with excitation of the Δ or N^* isobar. The rescatterings are shown for the one nucleon exchange in the initial (d), final (e) and initial plus final (f) states [18].

According to the ONE+SS+Δ model calculations [15, 16], which implicitly include the pp final state interaction (fsi), the pp pair is expected to be mainly in a $^1S_0$ state. Due to isospin invariance, the isovector nature of the pp pair leads to a suppression of the amplitude of the Δ mechanism by a factor of three in comparison to the ONE amplitude for all partial waves of the pp system [15]. The same suppression factor also applies for a broad class of diagrams with isovector meson–nucleon rescattering in the intermediate state, including excitation of N^* resonances [17]. As a result, the contribution of the ONE mechanism, which is sensitive to the NN potential at short distances, becomes more pronounced than in $pd \to dp$ scattering. Furthermore, the node in the half–off–shell pp scattering amplitude in the $^1S_0$ state at an off–shell momentum of about 0.4 GeV/c, shown in Fig. 1.3, would lead to a dip in the differential cross section of the deuteron breakup near T_p = 0.7–0.8 GeV beam energy [15, 18] (see Fig. 1.4a). At higher energies T_p =1–3 GeV, the cross section is expected to be dominated by the ONE mechanism and there it decreases rather smoothly.

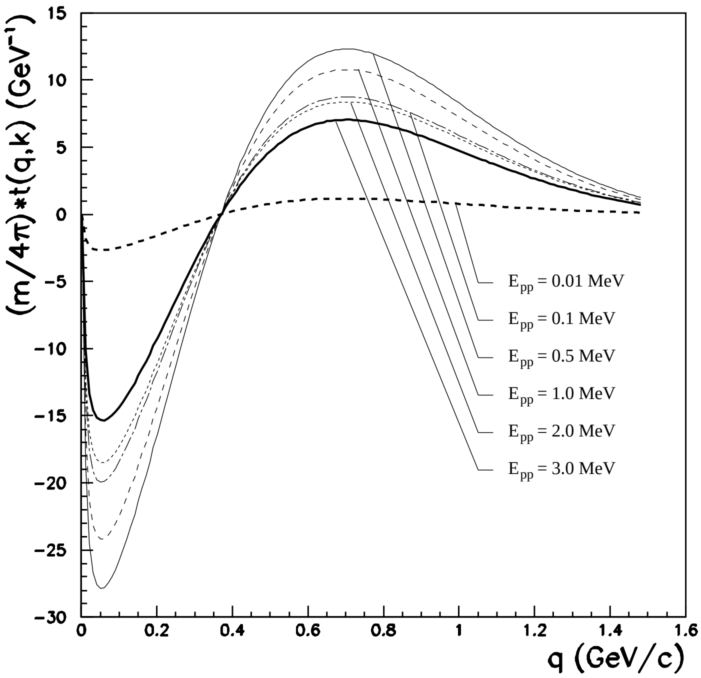

Figure 1.3: The half–off–shell $pp(^1S_0)$ scattering amplitude $(m/4\pi)\, t(q, k)$ as a function of the off–shell momentum q for different excitation energies of the proton pair E_{pp}: 0.01 MeV (dashed thick line), 0.1 MeV (dashed–dotted), 0.5 MeV (full thin), 1.0 MeV (dashed), 2.0 MeV (dotted), 3 MeV (full thick) [18].

Another attractive feature of the process is the simplicity of its phenomenological description, since in collinear kinematics it requires only two spin amplitudes. Therefore, a model–independent amplitude analysis becomes possible through the measurement of a few polarization observables. The theoretical predictions for the energy dependence of the differential cross section and for the polarization observables T_{20} and $C_{y,y}$ in the framework of ONE+SS+Δ model are shown in Fig. 1.4.

(The polarization observables are discussed in Appendix B.) The angular dependence of the analyzing power A_y^p from the ONE+SS+Δ model is shown in Fig. 1.5 for different incident kinetic energies.

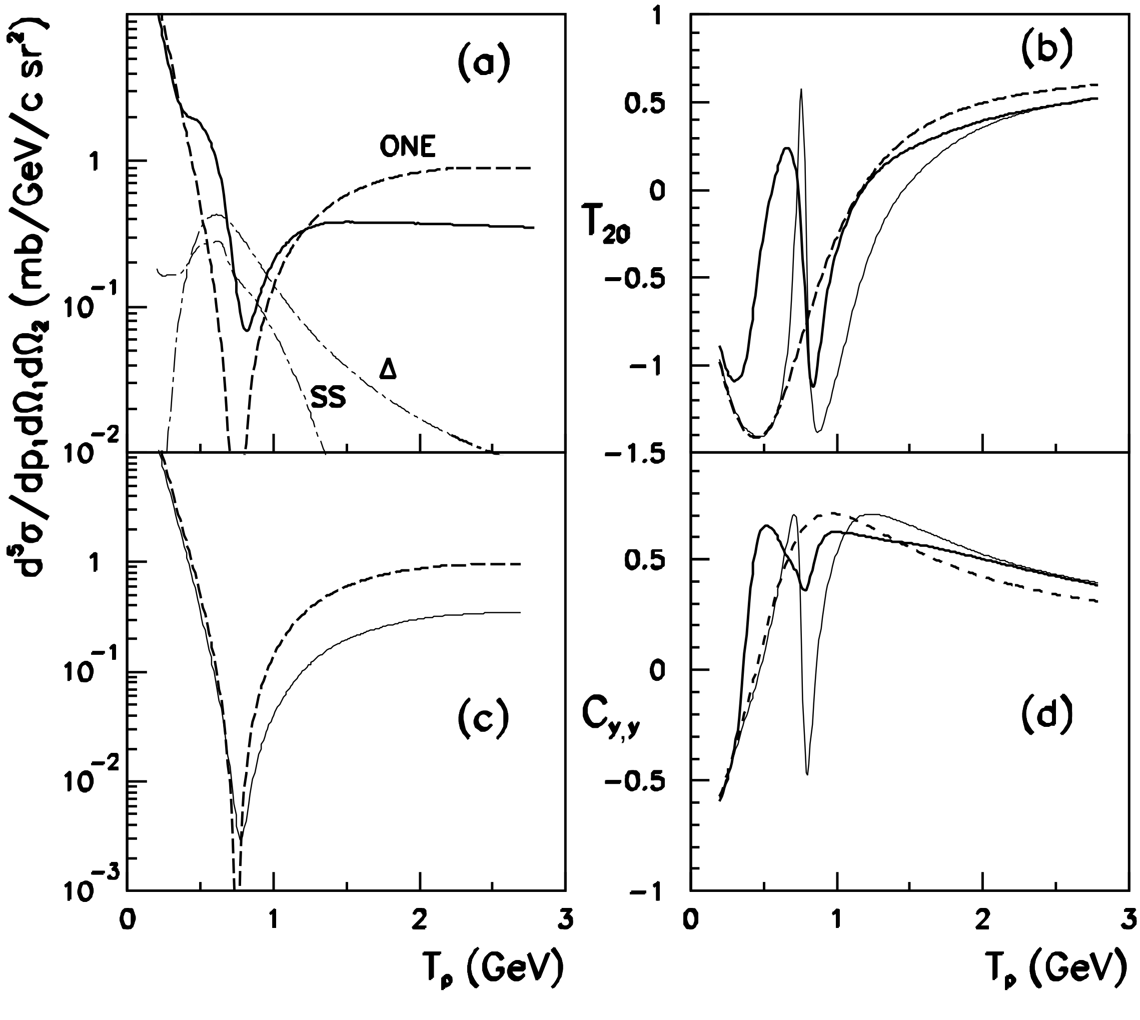

Figure 1.4: Calculated [18] laboratory cross section (a,c), tensor analyzing power T_{20} (b) and spin–spin correlation parameter $C_{y,y}$ (d) of the reaction $pd \to (pp)n$ versus the kinetic energy of the proton beam T_p for the neutron scattering angle $\theta_n^{c.m.} = 180°$ and the excitation energy of the pp pair $E_{pp} = 3$ MeV (dashed lines: ONE without rescatterings; thin full lines: ONE with all rescatterings taken into account in the distorted wave Born approximation (DWBA ONE) in the initial and final states; thick full lines: coherent sum of the DWBA ONE+Δ+SS mechanisms; dash–dotted lines (a): SS and Δ contributions).

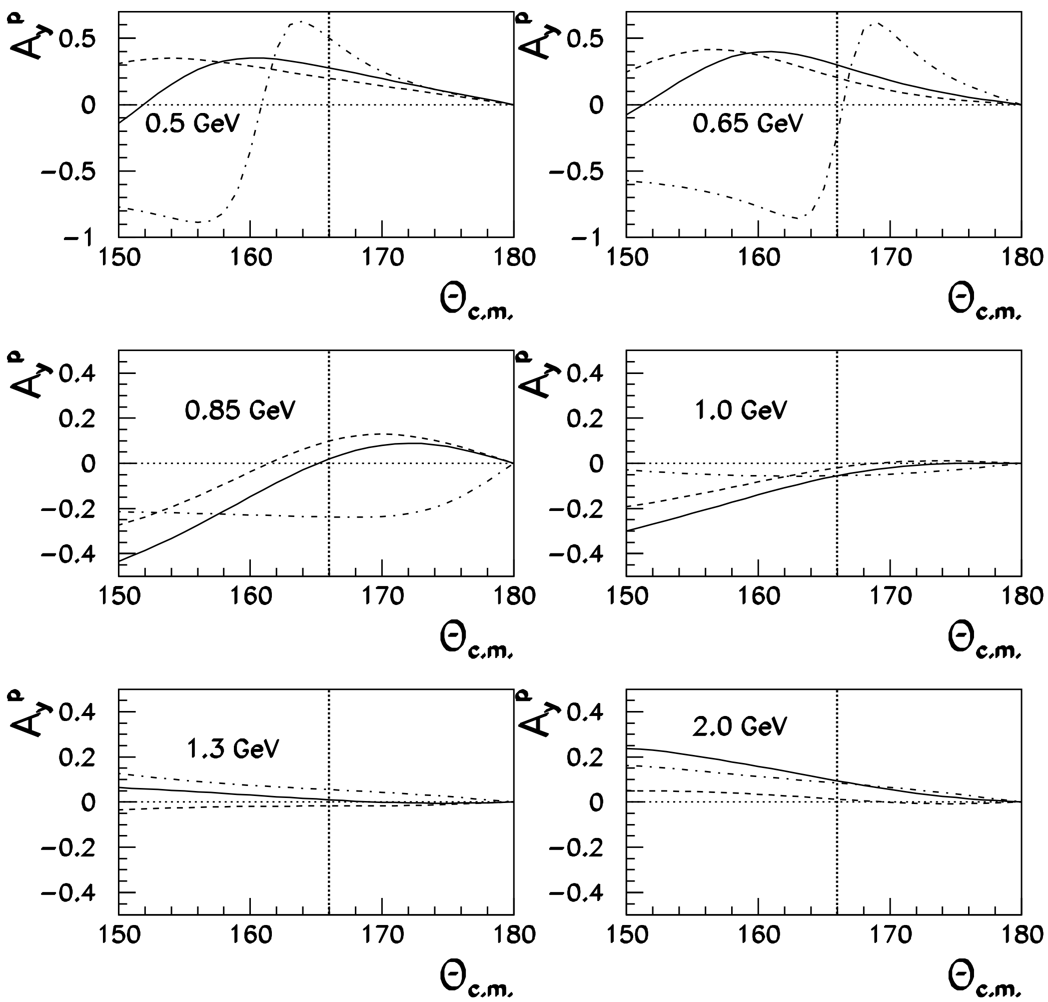

Figure 1.5: Calculated [19] vector analyzing power A_y^p in the $\vec{p}d \rightarrow (pp)n$ reaction at $E_{pp} = 3$ MeV for the different mechanisms at kinetic energies T_p between 0.5 and 2.0 GeV versus the c.m. scattering angle of the neutron (dashed–dotted lines: ONE(DWBA) with rescatterings; dotted lines: Δ excitation; dashed lines: ONE+Δ+SS; full lines: ONE(DWBA)+Δ+SS).

1.3 Deuteron Breakup Studies at ANKE

The experimental study of the deuteron breakup $pd \to (pp)n$ with emission of a fast proton pair at ANKE [20] consists of two main stages. The first stage includes the experiments with unpolarized target and unpolarized and polarized proton beam to measure the differential cross section and the vector analyzing power in those energy regions where the contributions of the reaction mechanisms are expected to be different. The second stage requires the polarized internal gas target with the aim to perform measurement of the tensor analyzing power and of several spin–spin and spin–tensor observables.

A first measurement of the differential cross section at six beam energies in the interval 0.6–1.9 GeV was done during one week of beam time in February 2001. In September 2001 a first experiment with polarized proton beam at ANKE was carried out (one week of beam time). In this experiment the vector analyzing power in $\vec{p}d \to (pp)n$ was measured at 0.5 GeV. The beam polarization was measured with the EDDA detector [21]. Unfortunately, the intensity of polarized beam was low because of difficulties with the polarized source. However, the techniques to measure the beam polarization was developed and the on– and off–line analysis procedures were developed and tested. These procedures were used during one week of beam time in July 2003, when the measurement of the vector analyzing power in $\vec{p}d \to (pp)n$ at two beam energies of 0.5 and 0.8 GeV was carried out. The beam polarization was measured as well at EDDA as at ANKE.

2. Experimental Setup

The experiments have been performed at the magnet spectrometer ANKE at the COoler SYnchrotron COSY. For the deuteron breakup study the ANKE forward detector system and the silicon–detector telescope were used. The forward system provides the detection of particles emitted at small angles and high momenta. The silicon–detector telescope was used for selection of deuterons from elastic *pd* scattering with the aim to determine the beam polarization. In this chapter a technical overview of the detector system is given and the trigger and the data acquisition systems are described.

2.1 ANKE Spectrometer at COSY

The COoler SYnchrotron COSY-Jülich [22] provides high quality unpolarized and polarized proton and deuteron beams ($\Delta p/p = 10^{-4} - 10^{-3}$) in the momentum range from 300 MeV/c up to 3.7 GeV/c. An electron cooling system can be applied up to a beam momentum of 600 MeV/c and is complemented by a stochastic cooling system that covers the upper range from 1.5 to 3.7 GeV/c. In Fig. 2.1 the layout of COSY is shown. Polarized beams are produced at COSY using a polarized ion source developed by a collaboration of the universities of Bonn, Erlangen, and Köln [23]. The source provides a vector polarized proton beam and deuteron beams with all possible combinations of vector and tensor polarization. The polarized H^- and D^- ion beam delivered by this source is pre-accelerated in the cyclotron JULIC and injected by charge exchange in a thin carbon foil into the COSY ring. In a strong focusing synchrotron like COSY, imperfection and intrinsic resonances cause polarization losses during acceleration (see Appendix C for details). The magnet system of COSY allows one to overcome all imperfection resonances by exciting adiabatic spin flips without polarization losses. A tune-jump system, consisting of two fast quadrupoles, has been developed to handle intrinsic resonances in COSY. This magnetic system is being successfully utilized at all intrinsic resonances in the momentum range of COSY. The main diagnostic tool to develop polarized beams in COSY is the EDDA detector [21]. The polarization is determined at EDDA by measuring the asymmetry of scattering of circulating COSY–beam particles by

CH_2–fiber targets. Additional polarimeters are installed in the injection beamline to COSY, in the COSY ring, and in the extraction beamline of COSY (Fig. 2.1). The intensity of the polarized beam in COSY can be increased by stacking injection with the electron–cooler and the beam quality can be further improved with stochastic cooling systems [24, 25]. COSY beams are delivered to four internal (ANKE, COSY–11, EDDA, PISA) and five external experiments (TOF, MOMO, GEM, NESSY and JESSICA).

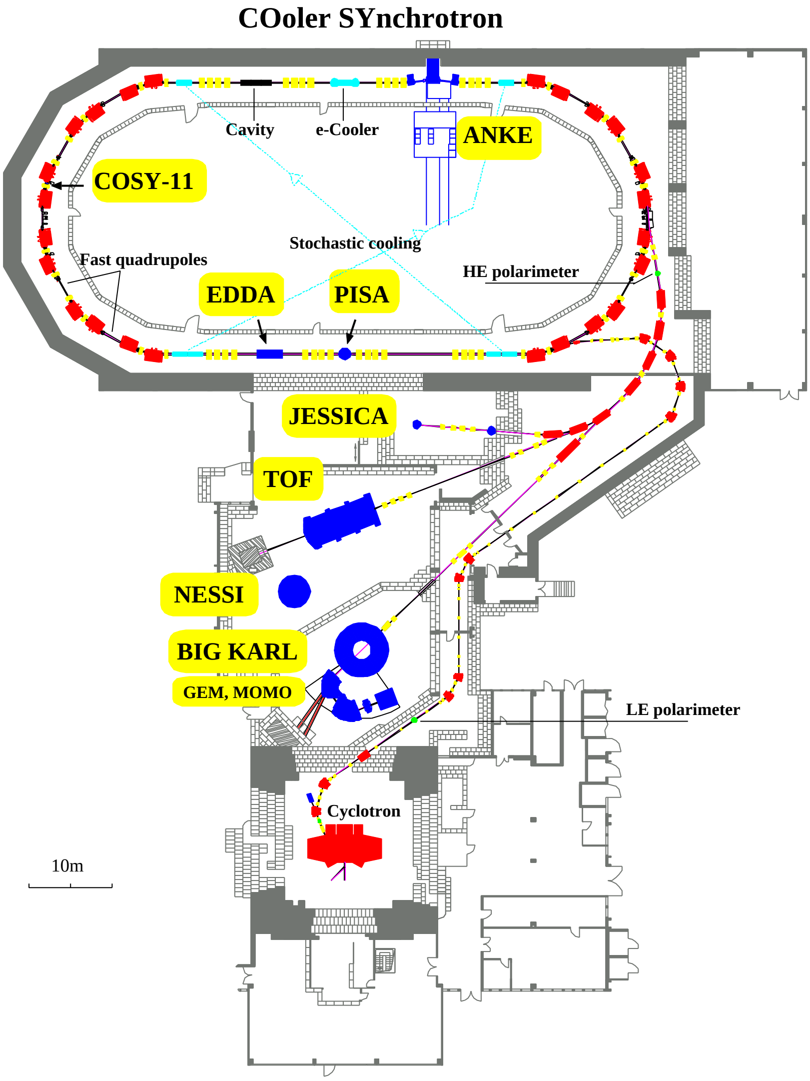

Figure 2.1: The Cooler Synchrotron COSY at Forschungszentrum Jülich with the injection system, the internal installations, and the beam lines to the external experiments.

The ANKE ("Apparatus for studies of Nucleon and Kaon Ejectiles") is a magnet spectrometer located at an internal target position of the storage ring COSY [26]. In Fig. 2.2 the schematic view of ANKE is shown.

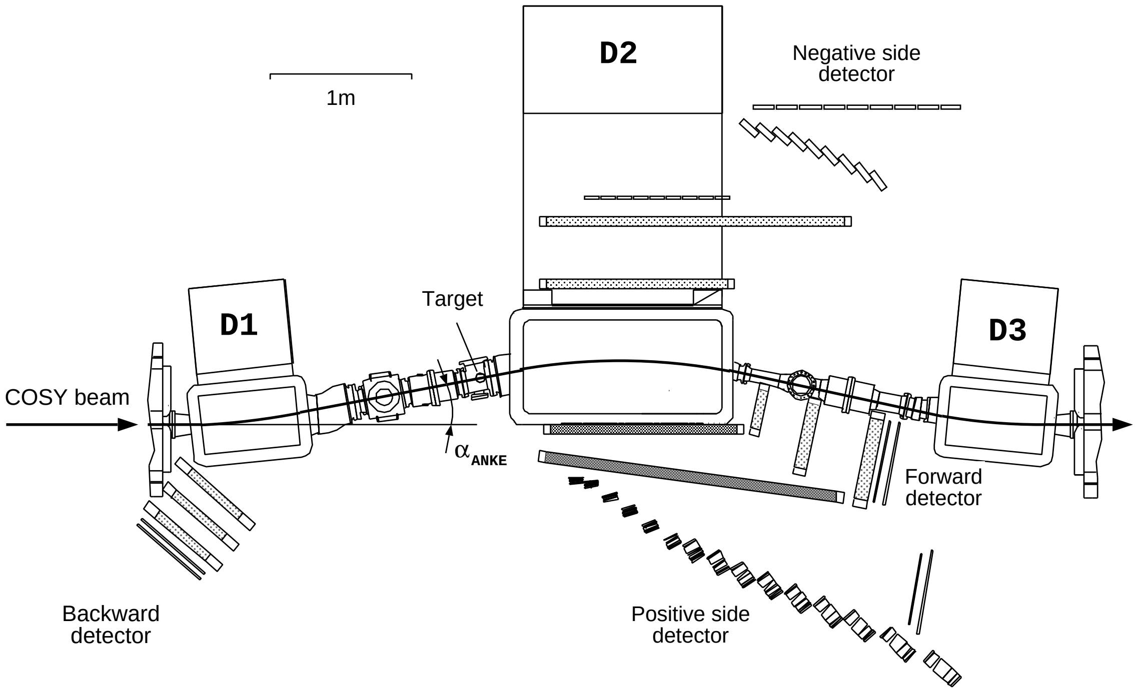

Figure 2.2: Top view of the ANKE spectrometer. The circulating COSY beam, the target chamber, the dipole magnets D1–D3, and four detector systems are shown.

The main components of ANKE are: a magnet system, an internal target, and four detection systems: side detectors for positive and negative particles, forward and backward detectors. The magnet system consists of the dipole magnet D1 which deflects the circulating COSY beam, the large spectrometer dipole magnet D2, and a third dipole magnet D3, identical to D1, to deflect the beam back to the nominal orbit. The deflection angle of the beam (α_{ANKE}) can be adjusted to optimize the magnetic field in D2 up to 1.56 T independently of the COSY beam momentum. Two types of targets are available: strip targets (carbon, polyethylene or any other solid material) and a cluster beam target [27], i.e. a beam of hydrogen or deuterium clusters crossing the COSY beam. A polarized storage–cell gas target [28], fed by an atomic beam source for measurements with polarized hydrogen and deuterium is being developed. The target will be ready for use at the ANKE target position at the end of 2004. The positive side detector has been developed for the study of subthreshold K^+ production from nuclei [29], and it provides an excellent kaon identification [30]. The negative side detector was developed for the investigation of K^- production from nuclei [31] and ϕ–meson production [32]. The momentum acceptance of the positive and negative side detectors is in the range of about 0.3 to 0.8 GeV/c. The backward detector is planned to be used for detection of backward scattered particles like protons with momenta 0.3–0.6 GeV/c from the deuteron breakup [20]. The forward detector, allowing one to detect positively charged particles in momentum range 0.3–3.7 GeV/c, is used in a number of experiments like a_0 production [33], ω and η production on deuterium used as an effective neutron target [34, 35], polarized charge exchange [36], and the variety of proton–induced deuteron breakup studies [20] which include the present work.

2.2 Forward Detector System

The ANKE forward detector (FD) system [37, 38] consists of three multiwire proportional chambers (MWPCs) and two layers of scintillation hodoscopes. In Fig. 2.3 only those parts of the spectrometer are shown that are relevant for the deuteron breakup study.

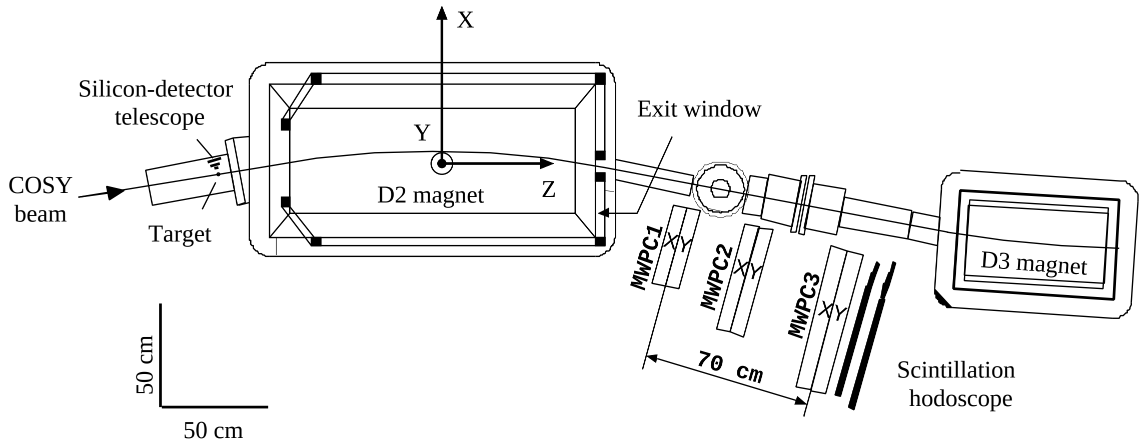

Figure 2.3: Components of the ANKE–spectrometer setup used for the present deuteron breakup study. Indicated are the circulating COSY beam, the target chamber, the spectrometer dipole D2, dipole D3, the forward detection system, and the silicon–detector telescope.

2.2.1 Multiwire Proportional Chambers

The forward detector is located between the spectrometer dipole D2 and the dipole D3. The available space is rather limited. The distance between the dipole magnets is 1.6 m and the distance between the accelerator beam tube and the ANKE side detector is about 0.7 m. Such a location results in severe requirements for the tracking system. Due to closeness to the beam pipe, it must be able to operate at rather high counting rates ($> 10^5 s^{-1}$). In addition, because of the short distance between the MWPCs, one has to achieve a sufficiently high spatial resolution (better than 1 mm). Such spatial resolution leads to a momentum resolution of about 1% which allows one to identify reliably the deuteron breakup events by missing mass (see Secs. 4.4 and 5.4) and to select proton pairs with small excitation energy $E_{pp} < 3$ MeV (see Sec. 3.3). Particles emitted at small angles and high momenta pass the detector region close to the beam pipe, which means that the width of the chamber frame must be minimized on the side of the beam pipe.

These requirements are fulfilled by the multiwire proportional chambers [42, 43] with a small anode–cathode gap, filled with a fast gas mixture of CF_4 + iso–C_4H_{10} and containing a supporting foil for anode wires.

To provide the required spatial resolution a signal wire step of 1 mm was chosen which is usually difficult to combine with a rather large wire length of up to 60 cm. Good electrostatic stability of the chambers [44] is achieved by use of a high resistance foil that supports the wires. The chamber assembling technology is described in Ref. [45].

The FD system comprises three MWPCs in total. Each of them is composed of one X and one Y module. Every module contains a wire and a strip plane. In the following, the planes located in an $X(Y)$ module will be referred to as the $X(Y)$. Wires are oriented vertically in the X wire planes, and horizontally in the Y planes. The strips are inclined by 18° with respect to the vertical axis in the X planes, and by −18° in the Y planes. The MWPCs are mounted on a support frame together with the hodoscope.

The layout of the chamber module is shown in Fig. 2.4, the design parameters are given in Table 2.1.

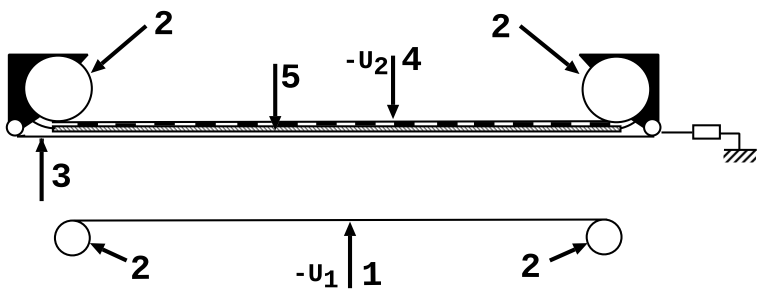

Figure 2.4: Schematic layout of a MWPC module. 1 — drift electrode; 2 — support rods; 3 — anode wires; 4 — mylar cathode foil with strips; 5 — high resistance foil.

The drift electrode, labeled 1 in Fig. 2.4, is made of a carbon–coated mylar foil, which is fastened to the rods (2). Negative voltage $U_1 = -2.8$ kV at the electrode provides the electric field for the electron drift towards the anode wires which are kept at zero potential. The cathode plane (4) consists of a mylar foil covered with conductive silver paint strips. The strips are held at a negative potential $U_2 = -1.7$ kV, and are separated from the anode wires (3) by a foil of the necessary resistance (5) made of varnished cloth. The foil becomes conducting by initial diffusion of iodine from an iodine alcoholic solution. To keep the foils resistance in the required range, an isopropyl alcohol was later added to the gas mixture. The resulting gas mixture is 80% CF_4 + 17% C_4H_{10} + 3% C_3H_8O.

	MWPC1	MWPC2	MWPC3
Sensitive area [cm^2]	33×26	44×34	53×41
Anode wires	20μ diameter, gold plated W+Re		
Anode wire spacing [mm]	1.05		
Strip width [mm]	3.15		
Drift electrode to wire plane distance [mm]	1.5	2.0	2.5
Final resistance of the foil [Ohm $\cdot$ cm]	10^9		
Thickness in units of radiation length	0.46% each MWPC		

Table 2.1: Parameters of the MWPCs

The chamber operation differs significantly from that of conventional proportional chambers as described in Ref. [46]. The chambers produce signals 6 ns long (FWHM) for the wire planes and 30 ns long for the strip ones. The time jitter of the signals is small, being around 8 ns for the wire pulses. This allows effective operation with short strobe signals. In the present setup, the time resolution of the tracking system is limited by the readout electronics [47], which requests a strobe length > 50 ns (while the chambers themselves could work with much shorter strobe pulses). The average number of wires fired by a crossing particle (cluster width) is close to one, which leads to a high precision of the coordinate measurements.

2.2.2 Scintillation Hodoscope

The forward scintillation hodoscope (FH) consists of two planes (FH1 and FH2) with 8 and 9 vertically oriented counters in planes FH1 and FH2, respectively (Fig. 2.5). The counters of one plane are shifted by half a counter width with respect to the counters of the other plane. The vertical length of all scintillators is 360 mm, the width is 80 mm for most counters and it gradually decreases to 40 mm for the counters in the high momentum region near the beam pipe, where higher counting rates are expected. The scintillator thickness is 20 mm for the 80 mm wide counters and 15 mm for the others. The scintillators are viewed from both ends via lightguides with secondary electron multipliers (SEM) of the types XP4222 (2 inch diameter) and XP2972 (1 inch diameter)[1] for the 20 mm and 15 mm counters, respectively. The counters, being independent units, are assembled in a common frame.

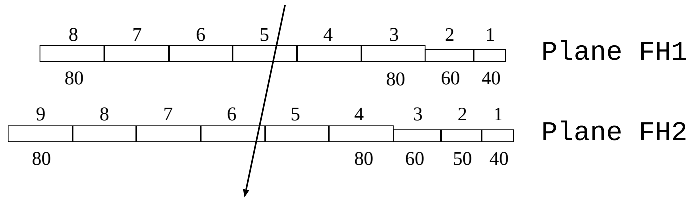

Figure 2.5: Schematic top view of the forward scintillation hodoscope. The numbers above the planes are the counter numbers, those below the planes give the widths in mm.

The front–end electronic channel for each counter (Fig. 2.6) includes a linear fan–out and a constant fraction discriminator/meantimer (CFD/MT) [39]. From each counter two analog signals (from the *upper* and *lower* SEMs) and three logical signals (two from CFDs of the *upper* and *lower* SEMs and one from MT) are available for digitization in QDCs and TDCs and recording as well as for triggering purposes [40].

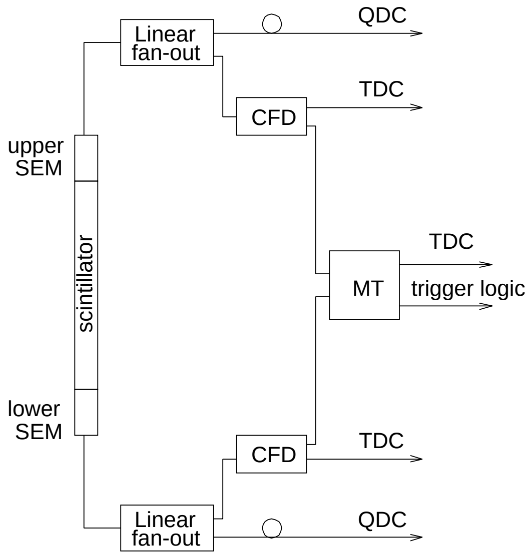

Figure 2.6: Scheme of the electronic readout of a FH counter (see text).

[1]Philips Components, Burchardstraße 19, D–20095 Hamburg

The time resolution of the counters under experimental conditions lies in the range σ =100–150 ps, the lower value corresponds to the counters with thicker scintillators. These values allow measurements of time–of–flight (TOF) differences between counters within the FH or between counters in the FH and counters in the other detector systems. No absolute TOF values can be measured, because of the absence of trigger detectors near to the target.

Using the time information from the upper and lower CFD channels of a counter, one obtains the vertical hit coordinate Y of the detected particle. The vertical spatial resolution obtained with this method, is σ_Y = 1.5–2.2 cm. The horizontal accuracy in the hodoscope is defined by the counter widths. Taking into account the shift between the two planes FH1 and FH2, the horizontal uncertainty is close to half the counter width, if signals from both planes are used. The coordinates, obtained this way, are used in the first step of the track–reconstruction procedure in the FD proportional chambers. The achieved coordinate resolution of the FH is sufficient to define a track search corridor and thus to exclude most of the spurious tracks.

The amplitude information from the FH is used in the off–line analysis for particle identification and event selection of the processes under study. The particle identification by energy losses is described below in Sec. 3.5.2.

2.2.3 Detector Acceptance

The horizontal acceptance of the forward detector is shown in Fig. 2.7. The vertical acceptance is ±3.5 degree, given by the D2 gap height of 20 cm and the 175 cm trajectory length between target and D2 exit. The trigger rate from counts in the hodoscope results mainly from elastically and quasielastically scattered protons, from protons associated with meson production and, at beam energies below 1 GeV, from deuterons produced in the $pp \to d\pi^+$ reaction. Events with two registered particles contributed little to the total trigger rate and were selected off–line. Protons from the deuteron breakup process $pd \to ppn$ with excitation energy $E_{pp} < 3$ MeV could be detected with the experimental setup for laboratory polar angles between 0 and 7 degrees at all beam energies.

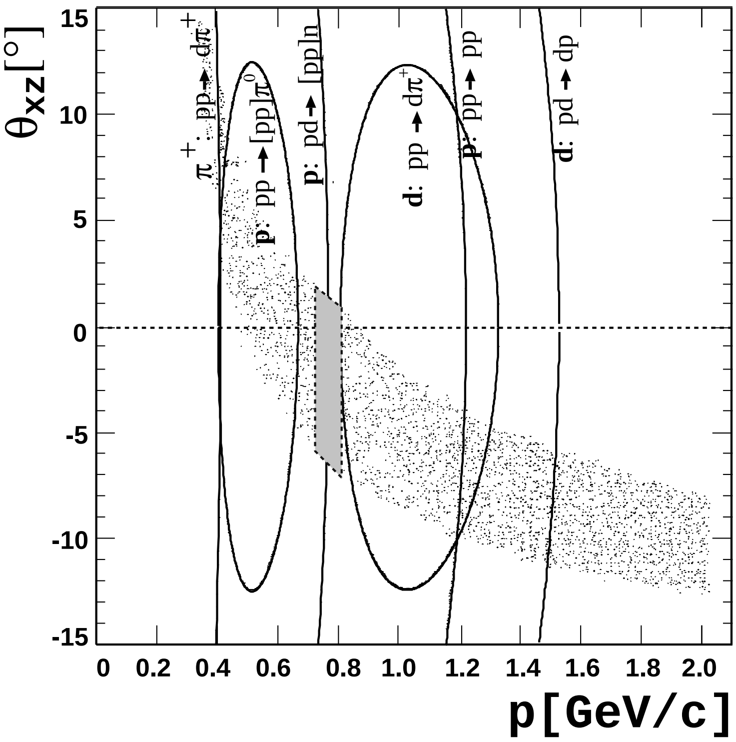

Figure 2.7: Plot of the acceptance of the setup from a MC simulation (dotted area) showing the projection of the polar angle θ_{xz} on the horizontal plane vs ejectile momentum for $T_p = 0.6$ GeV beam energy. The curves show kinematical loci for π^+, p, and d from the given reactions. The symbol [pp] denotes pp pairs with zero excitation energy, while the grey area contains those events with $E_{pp} < 3$ MeV.

2.3 Silicon–Detector Telescope

The ANKE silicon–detector telescope [49] was developed to study reactions with deuterium as an effective neutron target. The silicon telescope consists of three layers of silicon detectors (Fig. 2.8): 60.9 μm and 300 μm thick surface barrier detectors and a 5.1 mm thick lithium–drifted strip detector [50]. The telescope is used to identify low–energy spectator protons in pd or dd collisions, down to a proton kinetic energies of 2 MeV. In addition, the separation of deuterons from pd elastic scattering provides the possibility to measure the luminosity and to determine the beam polarization.

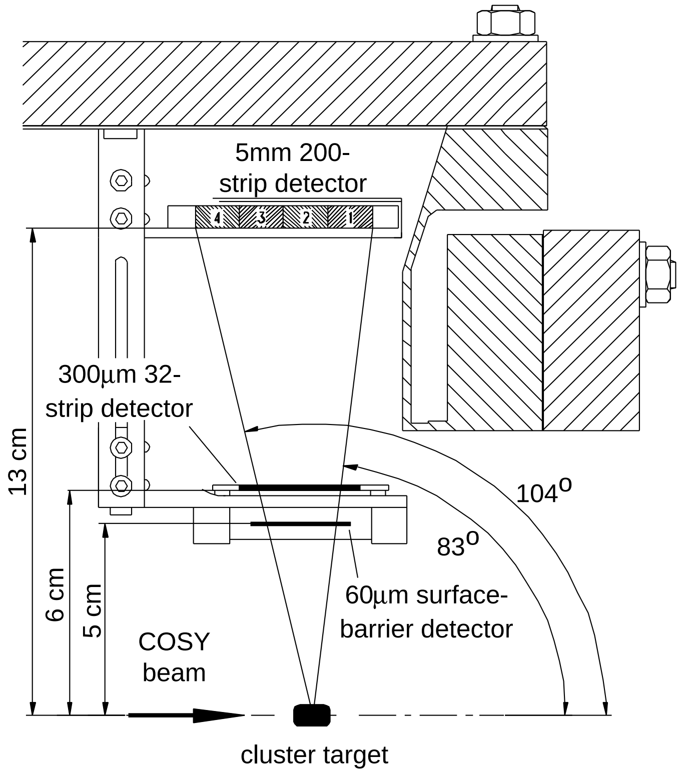

Figure 2.8: Top view of the silicon–detector telescope in the ANKE target chamber. The cluster beam crosses the COSY beam from above. The telescope consists of a circular Si surface barrier detector and two Si detectors with vertical strip structure.

The basic features of the Si detectors are listed in Table 2.2. The 60 μm detector and all 32 strips of the 300 μm detector are read out individually. The 5.1 mm thick detector is read out in four sections of 50 strips each by a resistor chain. The measurement of energy losses in each detector allows one not only to identify protons and deuterons but, also to measure their kinetic energies with 1% precision [49].

	1^{st} layer	2^{nd} layer	3^{rd} layer
sensitive thickness	60.9 μm	300 μm	5.1 mm
active dimensions	ø12.0 mm	32×15 mm	46.8×23 mm
number of strips	—	32	4×50
pitch	—	1 mm	235 μm

Table 2.2: Parameters of the silicon detectors in the telescope used at ANKE during the run in September 2001: the first layer is round and not segmented, whereas for the other layers the number of strips and their width (pitch) is given as well.

During the run in September 2001, the setup shown in Fig. 2.8 was positioned such that in the horizontal plane angles from 83 to 104° were covered. In the vertical direction ±10° and ±7° were covered by the second and third layers, respectively. This position was chosen for the ω production measurements in August 2001 [63]. In the July 2003 beam time the position of the detectors was optimized for the detection of deuterons from *pd* elastic scattering in the new target chamber in the angular range from 82° to 86° in the horizontal plane and about ±2° in the vertical plane.

2.4 Trigger and Data Acquisition

During the run in July 2003, four triggers were running in parallel:

- A single–particle trigger T_1, generated by a particle hitting a counter in the first FD hodoscope plane and one of the two counters in the second plane. This trigger, selecting mainly single protons, was used with a prescaling factor of three for the luminosity determination and for a continuous monitoring by measuring the spin(up)/spin(down) asymmetry of proton scattered by angles between 5.0° and 10.0°. A peak in the proton–momentum spectra at these angles corresponds to unresolved elastic and quasielastic scattering of protons.
- A double particle trigger T_2 with signals from a special coincidence unit [51] selecting events with hits in two different hodoscope counters or a twofold hit in a single counter with twice the energy loss.
- A trigger T_3 consisting of a coincidence of a signal from the silicon–detector telescope and a non–prescaled trigger signal T_1.
- A scaler trigger T_4, used to read out the scalers periodically ten times per second.

In the first unpolarized run in February 2001 the single particle trigger T_1 was used as the main trigger without any prescaling. T_3 trigger was used for the luminosity determination as discussed in Sec. 4.2.5. For each trigger signal except T_4 all sub–systems of ANKE were read out. This includes the full forward system and the silicon telescope.

By the use of single board PCs, connected via a synchronization bus, one achieves read–out times of about 100 μs. This is due to the fact that the data are labeled event–by–event but transferred as separate clusters of one sub–system to the central data acquisition and written to a DLT tape. Only thereafter, dedicated software disentangles the sub–events and combines them to a full event [52]. For the online analysis, a fraction of the events can be distributed to several data streams in order to run several analysis programs simultaneously.

3. Data Analysis Procedures

In this chapter the data analysis procedures, used for processing all experimental data, are described. Here mainly those procedures of the data analysis are considered that are common for all experiments with FD at ANKE. The details of the deuteron breakup event selection, extraction of the cross section and vector analyzing power are described in Secs. 4 and 5.

3.1 Track Reconstruction

The track reconstruction procedure, developed for the ANKE forward detector, is described in detail in Ref. [38]. Here, the main parts of the track search algorithm are discussed.

With the origin in the center of its gap, the positive X axis (pointing to the other side of the COSY ring), the Y axis (pointing up), and the Z axis form a right–handed Cartesian coordinate system as illustrated in Fig. 2.3.

The average width of clusters in the MWPC wire planes corresponds to about 1.1 wire spacing. The three planes determine three horizontal and three vertical track coordinates. In the planes with inclined strips, clusters of three strips on the average (≈ 1 cm cluster width) yield six additional track informations. Furthermore, each plane of the hodoscope provides input for the track search. The X coordinate is obtained with an accuracy of half a counter width (2–4 cm), the Y coordinate with an accuracy of 1.5–2.2 cm (see Sec. 2.2.2).

The particle trajectory between the first MWPC and the hodoscope is very close to a straight line. The deviation from a straight line is caused by the fringe field of the magnet and corresponds to 0.6 mm for particles with momenta of 0.4 GeV/c. Whereas multiple scattering of particles in the 0.5 mm thick aluminum exit window of D2 considerably affects the reconstructed momentum resolution, scattering in the air between the MWPCs and inside the MWPCs can be neglected during the track search. A straight line for the track is assumed in the region between the first MWPC and the hodoscope. The line is described by four parameters $\vec{T} = (\tan\theta_{xz}, \tan\theta_{yz}, x_w, y_w)$. Here θ_{xz}, θ_{yz} are polar angles projected onto the planes indicated by indices and x_w, y_w are the X and Y track coordinates at the surface of the D2 exit window which lies in a XY plane.

With the simplest triggering for at least one particle detected in the FD, more than 99% of the events produce only one track in the MWPCs. On the other hand, the average number of clusters in a wire plane is 1.7 per event (the events where this plane is efficient are considered). These figures reflect the situation of normal background conditions and normal level of noise from the MWPC readout electronics.

In order to achieve the required accuracy of three–momentum reconstruction, one has to draw the straight track through the wire clusters. Due to threshold effects in the MWPC readout, it is not possible to require the presence of clusters from all the wire and strip planes in a track. Consequently, a track is selected in the MWPCs by a combination of clusters at least from two X and two Y wire planes. In the best cases information from all the wire and strip planes are available. Because of a soft requirement on the minimum track content, several concurrent track candidates can be constructed. Among different solutions, the most probable track is found by the following criteria:

- it contains the largest number of wire clusters,
- it yields the best confidence level of the straight line fit,
- the number of observed clusters in the track is in best agreement with what is expected according to the known 12 local wire– and strip–plane efficiencies ε_i. This criterion is applied by selecting the track with the maximum value of $\prod(1-\varepsilon_i)$. Here the product includes those planes, where no cluster is observed in a track. A high value of the product indicates agreement with a reduced number of clusters in a track due to low local efficiency.

A track is derived in the following sequence: in the beginning we use only information from the wire planes and the hodoscope to draw a straight line in space. The horizontal projection including clusters in two X wire planes and fired counters is drawn first, and clusters in two Y wire planes are included then to define the vertical projection. The information from the planes with inclined strips then is used to resolve ambiguities.

3.2 Chamber Efficiency Determination

The average efficiency of a sensitive plane is varying in the range of $80-90\%$. This is caused by the short duration of the signal from the wire planes, which is not optimal for the readout electronics used. Under these conditions, the properties of the high–resistive foil lead to an inhomogeneous efficiency distribution over the plane surface. To account for such inhomogeneities one has to know the efficiency at each point of each sensitive plane. The correction factor can be calculated for each event using the efficiency for the plane region crossed by the track.

In order to obtain the efficiency map of a sensitive plane, the sensitive area is divided into 20×20 rectangular cells (of 2–3 cm size), and the efficiency is calculated for each cell. To do that, we fix tracks using single–cluster events in the other two MWPCs, and from all tracks crossing this cell the probability to find a hit is calculated. This procedure requires a large amount of experimental data to achieve reasonable statistics in each cell on each plane. The statistical error of the efficiency value is below 1% for the central part of the chambers, and about 10% for near–the–edges cells for in total 10^6 events used. The sources of systematic errors are

- presence of noise clusters in the plane for which ε is determined,
- false tracks used for the hit search,
- a significant change of ε within a single cell,
- dependence of the detection efficiency on the energy loss.

A dedicated study showed that in the first two cases the errors do not exceed 2–3 %. The third factor can be suppressed by exclusion of the most inhomogeneous parts of the MWPC planes from the data analysis. The last factor can be controlled by selecting the particle type and momentum of the particles used for determination of ε. An example of the angular dependence of the track efficiency for diffractively scattered protons is shown in Fig. 3.1.

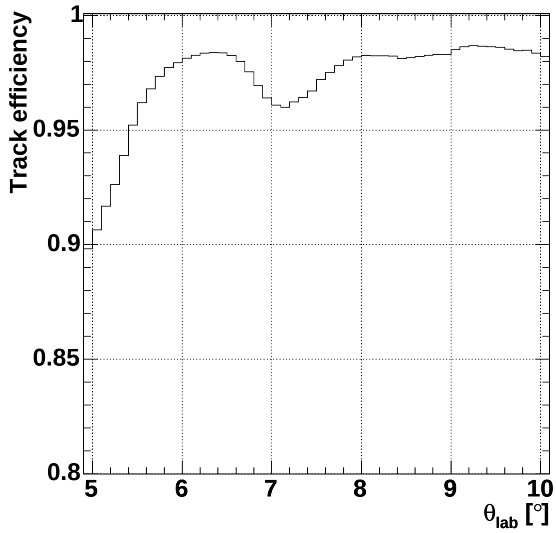

Figure 3.1: MWPC track efficiency.

The track efficiency is rather high due to the combinatoric possibilities taken into account, i.e. track reconstruction from a combination of clusters of at least two of three X and two of three Y wire planes.

3.3 Momentum Reconstruction

The magnetic field of D2 is known on a three–dimensional grid, allowing one to reconstruct the ejectile 3–momenta at the production point. A number of reconstruction methods have been adopted for the ANKE forward detector, such as box–field approximation, tracing with the Runge–Kutta method, use of neural networks, and a polynomial approximation. The latter method has been chosen for the data analysis due to the high speed in the calculations, and the sufficient accuracy of the approximation. The method expresses the components of the 3–momentum in form of a polynomial of the measured parameters. We use its modification similar to the one described in Ref. [53].

Each of the momentum components is approximated by a full polynomial of the third degree of the four track parameters $\vec{T}$. The polynomial coefficients are found from a teaching sample of events, produced by a GEANT–based simulation program. The sample is generated for every combination of magnetic field value, the beam direction, and the target position.

The accuracy of the reconstruction method was studied on a set of simulated events obtained without smearing by multiple scattering, MWPC coordinate resolution, and size of the beam–target overlap. For such events the accuracy (RMS) of the reconstructed momentum was 5 to 10 times better than for a set obtained with full smearing. The momentum resolution with full smearing is shown in Fig. 3.2 as a function of the ejectile momentum. This figure also shows that the uncertainty of the reconstructed momentum due to uncertainties in the input data lies below 0.1 % which is confirmed by the measured resolutions for elastically scattered protons.

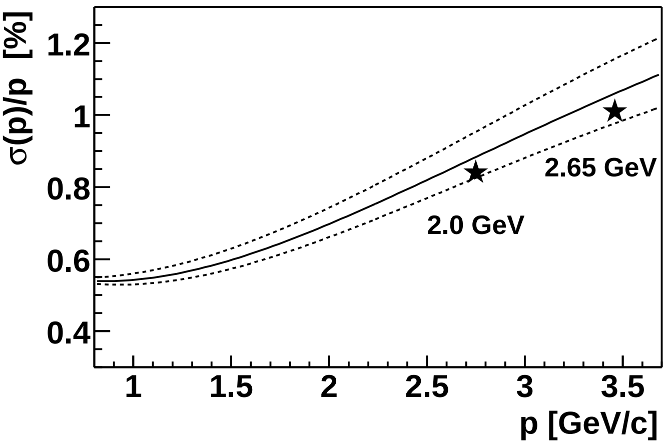

Figure 3.2: Calculated (solid line) and measured momentum resolution for protons. The stars represent the experimental resolution for elastically scattered protons for T_p=2.0 and 2.65 GeV. The dashed curves give the uncertainty of the calculated resolution.

The accuracy of the momentum reconstruction allows one to select reliably proton pairs with small excitation energy $E_{pp} < 3$ MeV. Figure 3.3 shows the E_{pp} resolution as a function of E_{pp}.

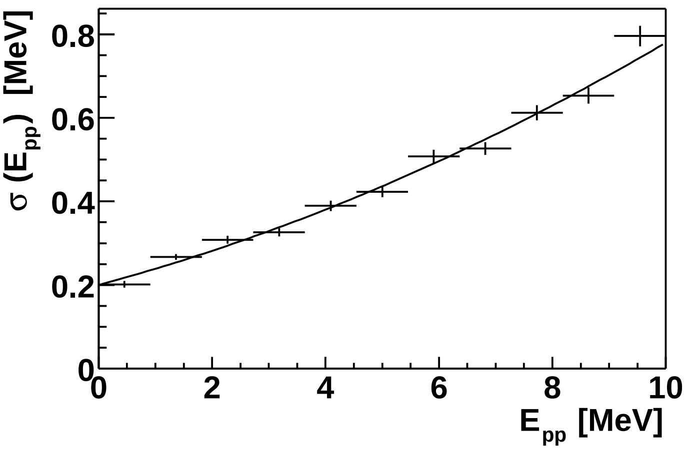

Figure 3.3: Resolution of the excitation energy E_{pp} in the reaction $pd \rightarrow ppn$ at $T_p = 0.7$ GeV resulting from simulations. The line is a second–order polynomial fit to the points.

3.4 Momentum Scale Calibration

The trajectory bending angle in the magnetic field for the particles detected in the FD is rather small ($\approx 20°$). Together with a rather small distance between the chambers, this leads to a high sensitivity of the reconstructed momentum value to the measured positions of the MWPCs. In the ANKE coordinate system, they are known with a precision better than 2 mm. However, a horizontal shift of the first MWPC by 2 mm would result in a change of the reconstructed momentum of a 2 GeV/c particle by 100 MeV/c. This value has to be compared with the required momentum accuracy of <10 MeV/c. Therefore, in order to reach the needed accuracy, a procedure has to be applied to improve the accuracy of the experimental setup parameters.

The X coordinates of a pair of MWPCs have been chosen as adjustable setup parameters, since the reconstructed momentum value is most sensitive to them. These coordinates are used as effective parameters. All other eventual inaccuracies are corrected by an appropriate determination of these parameters. It is sufficient to determine the position of one pair of MWPCs, because the position of the third chamber then can be fixed by using straight tracks.

In order to calibrate the momentum scale, processes with completely reconstructed kinematics are selected, and the effective parameters are fitted such to yield the correct missing mass values in these reactions. Among the processes with one particle detected in the FD are the reactions $pp \to pp$ and $pp \to d\pi^+$. One can use also several reactions with two detected particles, like $pp \to d\pi^+$, $pp \to pp\pi^0$ and $pp \to pn\pi^+$ with the H_2 target, and $pd \to dn\pi^+$, $pd \to ppn$ and $pd \to {}^3H\pi^+$ with the D_2 target. Examples are discussed in Sec. 3.5.

For illustration, the results of this procedure are shown for a data set obtained during the July 2003 beam time with the H_2 and D_2 targets at 0.5 and 0.8 GeV beam energies. Events from the $pp \to pp$, $pp \to d\pi^+$ processes, $pp \to pn\pi^+$, $pd \to pd$, $pd \to dn\pi^+$, and $pd \to {}^3H\pi^+$ were used. A detailed study of the accuracies achieved by the parameter tuning has been done in these cases. It has shown that the remaining deviations ΔM_{miss} of the missing mass mean value ΔM_{miss} are smaller than half the missing mass resolution $\sigma(M_{miss})$ and did not exceed 4 MeV (Table 3.1). In Fig. 3.4 examples of missing mass distribution are shown.

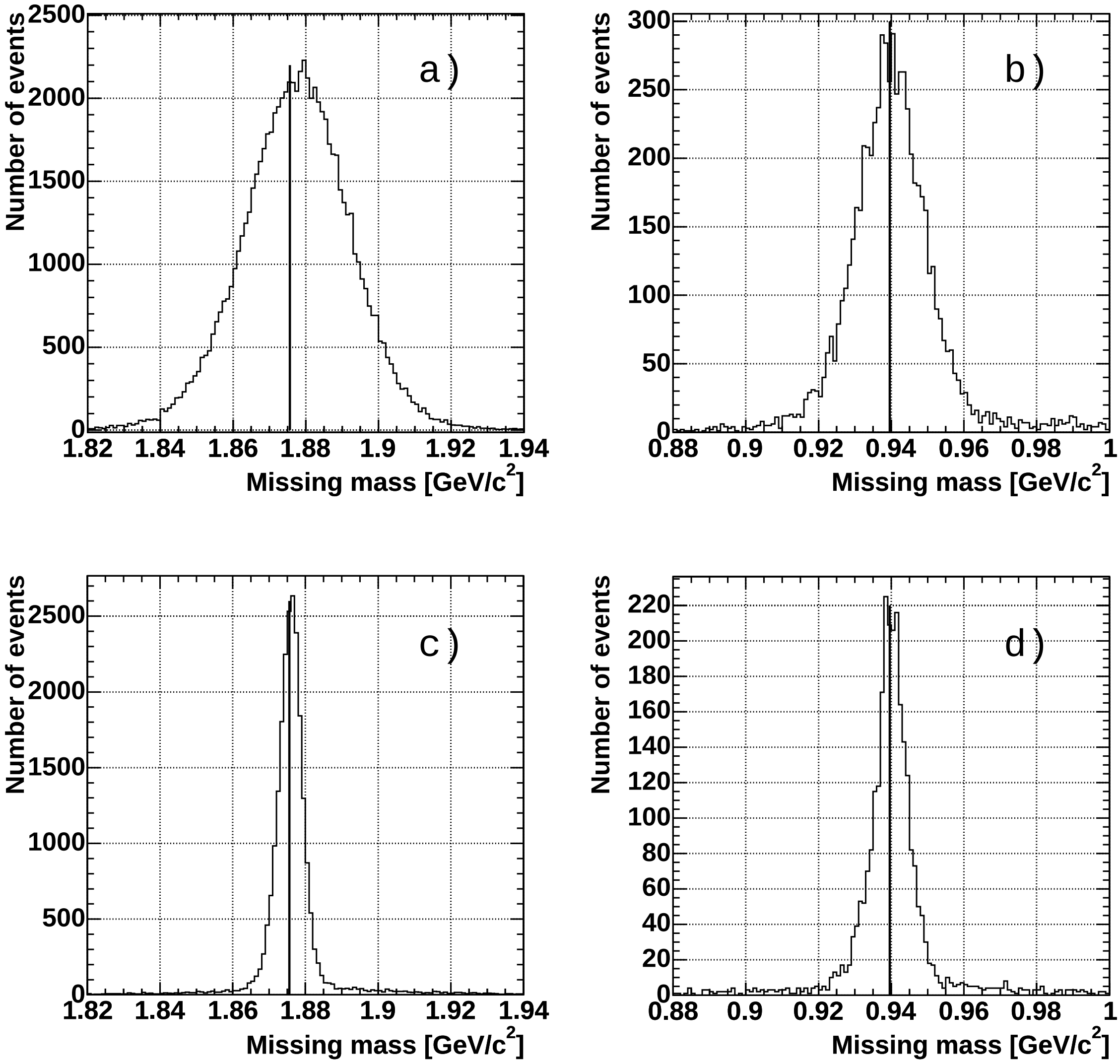

Figure 3.4: Missing mass distributions achieved by tuning of the horizontal positions of one pair of FD MWPCs for the reactions: $pd \to pd$ (a), $pd \to d\pi^+n$ (b), $pp \to \pi^+d$ (c), and $pp \to p\pi^+n$ (d). Lines show the literature values [54] of the masses.

Reaction	Beam Energy T_p [GeV]	M_{miss} [GeV/c^2]	$\sigma(M_{miss})$ [MeV/c^2]	ΔM_{miss} [MeV/c^2]
$pd \rightarrow p\mathbf{d}$	0.8	1.877	14.6	1.4
$pd \rightarrow d\mathbf{n}\pi^+$	0.8	0.9396	9.7	< 0.1
$pd \rightarrow \ ^{\mathbf{3}}\mathbf{H}\pi^+$	0.8	2.810	4.6	0.8
$pp \rightarrow \mathbf{p}p$	0.8	0.9343	18.0	-4.0
$pp \rightarrow \mathbf{d}\pi^+$	0.8	1.876	3.5	0.4
$pp \rightarrow p\mathbf{n}\pi^+$	0.8	0.9399	5.2	0.3
$pd \rightarrow p\mathbf{d}$	0.5	1.878	11.9	2.4
$pd \rightarrow d\mathbf{n}\pi^+$	0.5	0.9408	8.0	1.2
$pd \rightarrow \ ^{\mathbf{3}}\mathbf{H}\pi^+$	0.5	2.810	2.9	0.8

Table 3.1: Results of the missing mass determination achieved by tuning of the positions of the FD MWPCs. The particles which were not measured are given bold–faced.

3.5 Particle Identification

3.5.1 Momentum–Momentum Correlation

The absolute values (p_1 and p_2) of the momenta of two particles in any 3–particle final state process are strictly correlated if the particles are emitted at fixed directions (θ_1, ϕ_1) and (θ_2, ϕ_2). The correlation is conserved to some extent if the emission angles vary slightly within small solid angular ranges around (θ_1, ϕ_1) and (θ_2, ϕ_2). The rather limited angular acceptance of the FD results in a significant correlation between the momenta of two detected particles in any 3–particle final state. The advantage of such kinematical correlations consists in a distinctive clustering of the observed events with different masses in a plot of p_1 vs p_2. Therefore, a separation of the processes can be achieved without identification of the particles.

Figure 3.5 demonstrates such correlation. The processes $pp \rightarrow pp\pi^o$, $pp \rightarrow d\pi^+$ and $pp \rightarrow p\pi^+n$ (left panel) are well separated in spite of the fact that only the particle momenta have been used. With the D_2 target (right panel) one observes some smearing of the corresponding groups due to the Fermi motion in the quasifree scattering processes on nucleons in the deuteron. The additional processes $pd \rightarrow ppn$ and $pd \rightarrow \ ^3H\pi^+$ on the deuterium target appear in the plot. The observed correlation can be used to identify the processes and the masses of particles involved.

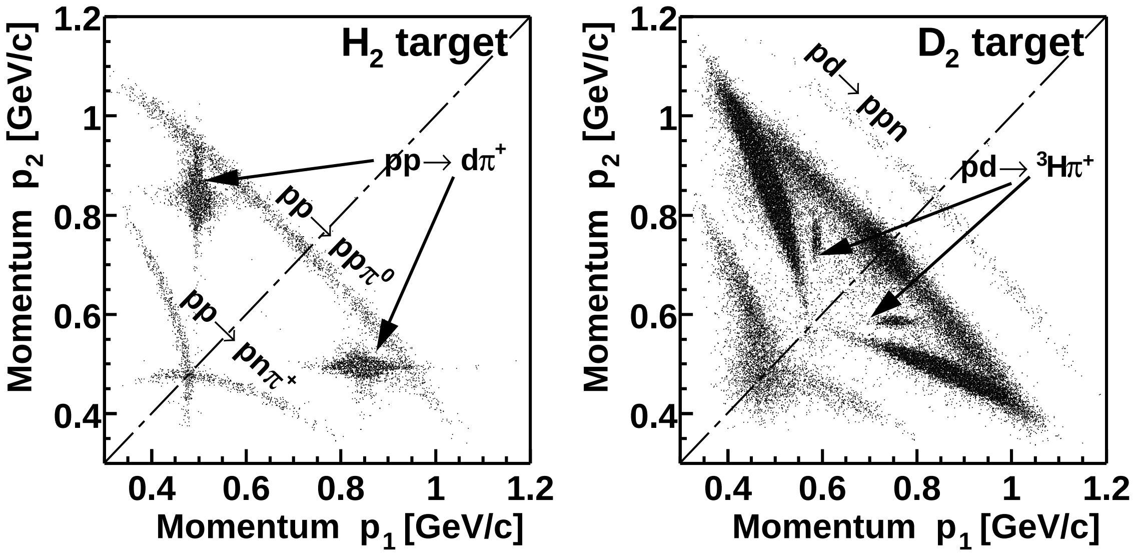

Figure 3.5: Momentum correlation distributions of double–track events for data taken with H_2 (left) and D_2 target (right) at a beam energy of T_p = 0.7 GeV. Dashed–dotted lines show symmetry axes. The distributions are not exactly symmetric because particles are not sorted by momenta.

3.5.2 Energy Losses in the Forward Hodoscope

At intermediate energies the energy losses in the counters depend considerably on the particle type and momentum. For this reason a special calibration procedure has been developed [41] with the aim of obtaining for each counter the relation between the measured charges in the QDC channels and the energy losses ΔE in units of MeV/cm. Events from binary processes, where all momenta are well defined, are identified and the most probable values of the corresponding peaks in the charge distributions are determined. The processes used are the $pp \to d\pi^+$ reaction at a beam energy 0.5 GeV with detection of the forward or backward emitted deuteron (in the c.m. frame) and the elastic pp scattering at beam energies $T_p = 0.5$, 1.0 and 2.0 GeV. The measured peak values can be related to ΔE as the particle types and momenta are defined and hence the energy losses are well known. These sets of five peak values for each counter (independent for signals of the *upper* and *lower* SEM) are used to find the ΔE as a polynomial function of the amplitude and the coordinate of the hit in the counter. The final calibration function for a counter is the average of the two functions obtained from independent fits for both counter amplitudes.

In Fig. 3.6 an example of the energy–loss distribution in counter 3 in the FH1 and the counter 4 behind it in the FH2 is shown. The data were collected for a hydrogen target at a beam energy of 0.5 GeV. Among the three prominent peaks in the spectrum the low–lying one corresponds to protons from *pp* elastic scattering while the medium and the higher–lying peaks correspond to deuterons from the two kinematical branches of the $pp \to d\pi^+$ process, i.e. the forward and backward deuteron emission in the c.m. frame. The small peak below the proton peak is due to pions. The spectrum contains also the continuum caused by detection of protons from the pion production processes in which the protons are widely spread in energy. So, the energy loss distribution as a whole reflects the dominant reactions. The widths (FWHM) of the peaks in the ΔE distribution vary from 11% to 17% with the deposited energies ΔE from 9.6 MeV/cm to 2.8 MeV/cm.

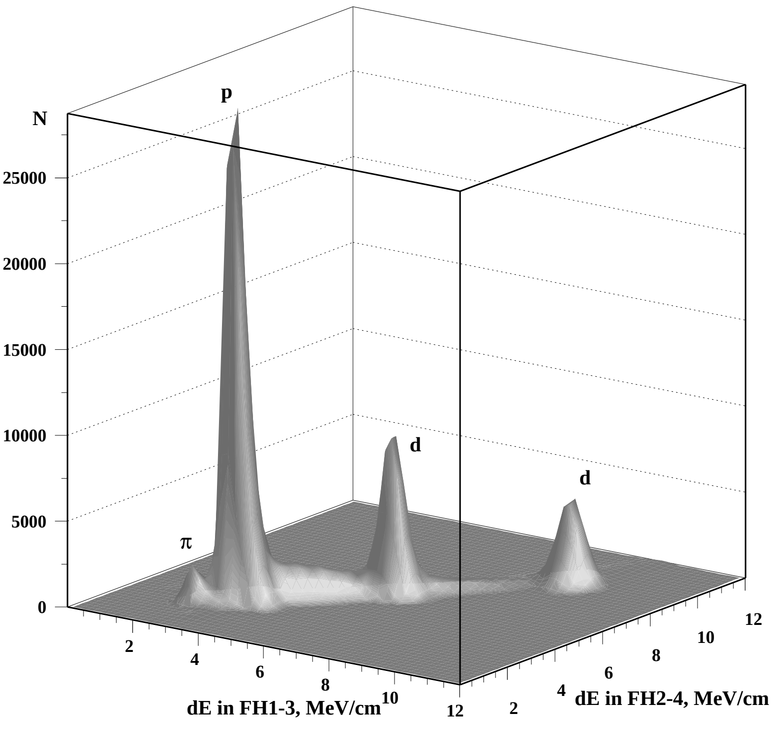

Figure 3.6: Energy–loss distribution in the counter FH1–3 and the counter FH2–4 in the two scintillation hodoscope layers (Fig. 2.5), measured at beam energy T_p = 0.5 GeV with a hydrogen target.

3.5.3 Time–of–Flight Difference

The two–particle events allow one to obtain the time–of–flight information, even when only the forward detector without any other detector group of the spectrometer is used. For events with particles hitting two different hodoscope counters, the arrival time difference Δt_{meas} can be measured by using the meantimer units (Fig. 2.6). On the other hand, assuming a definite mass value for both particles one can calculate the time–of–flight difference $\Delta t_{tof}(p_1, p_2)$ corresponding to their measured 3–momenta. Then, if the mass assumption is correct, Δt_{tof} should be equal to Δt_{meas}. Figure 3.7 shows a distribution of pairs in a plot of Δt_{meas} vs Δt_{tof}, obtained under the assumption that both particles are protons. It reveals a clustering of the pp events along the bisector $\Delta t_{tof} = \Delta t_{meas}$, while pairs of the other final states masses occupy different areas of the plot. By choosing appropriate cuts one can suppress the background and select the desired particle pairs.

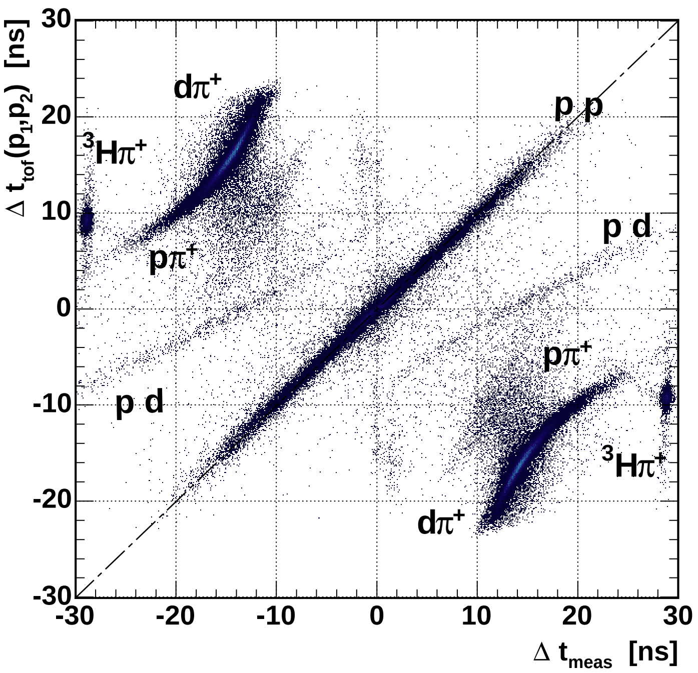

Figure 3.7: Time–of–flight difference Δt_{meas} measured in the hodoscope vs Δt_{tof} calculated under the assumption that both particles are protons. Data were taken with the D_2 target at $T_p = 0.5$ GeV. Dashed–dotted line shows a symmetry axis.

3.6 Background Rejection Criteria

To reject the background, some obvious cuts, common for all experiments, are applied to the tracks reconstructed in the FD:

- A cut on the Y coordinate of tracks in the hodoscope plane, taking into account the limits set by the target, the magnet gap, and the hodoscope geometry. If two particles hit the same counter within the resolving time, the up-down timing information, discussed in the previous section, may by distorted. Therefore, this cut is not used during the track search, but rather applied when it is sure that the counter is hit by a single particle.

- A cut to fulfill the requirement that the track has to cross the D2 exit window.

- Appropriate cuts in the correlated track parameters to confine the vertical vertex coordinate in the target region. This vertical cut is enabled by the weakness of the B_x and B_z components of the magnetic field strength of the spectrometer dipole D2. The projection of the whole trajectory onto the YZ plane can be approximated by a straight line crossing the beam–target intersection area. A typical experimental distribution of the track parameters in the YZ plane at the position of the D2 exit window vs the Y coordinate is shown in Fig. 3.8. The area inside the tetragon contains the accepted events. The width of the distribution along $\tan\theta_{YZ} = 0$ of about 2 cm reflects the vertical COSY beam dimension, the effects of MWPCs resolution, and the effects of multiple small–angle scattering.

After applying the criteria mentioned above and the determination of the momentum, one can reconstruct the vertical track coordinate in the target region, corrected for the magnetic field (Fig. 3.9). This is done in the same polynomial approximation as the three–momentum reconstruction, and allows one to apply a more refined background rejection criterion.

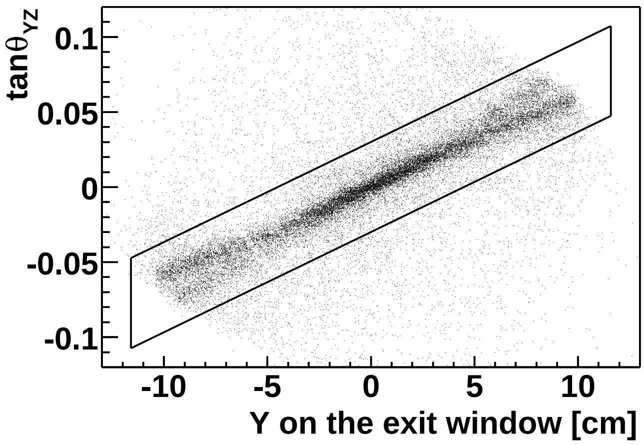

Figure 3.8: Correlation of the track parameters in YZ plane vs. the Y coordinate at the position of the exit window.

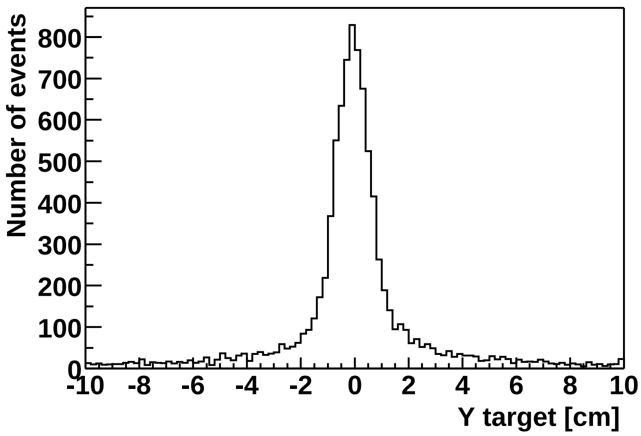

Figure 3.9: Reconstructed Y coordinate of the track at the target position.

4. Measurement of the Differential Cross Section

The measurement of the differential cross section of the deuteron breakup $pd \to (pp)n$ was performed at six beam energies $T_p = 0.6$, 0.7, 0.8, 0.95, 1.35, and 1.9 GeV during the February 2001 beam time. The energies have been chosen in order to investigate the main peculiarities of the energy dependence of the cross section expected in the theoretical model [18], i.e. a dip at 0.8 GeV and a plateau in the 1.2 – 2.5 GeV energy range. In this chapter the experimental conditions, methods of luminosity determination, the determination of the acceptance for the setup, and the identification of the process are described. The results are compared with predictions of theoretical model. The recent theoretical analyses of the data are reviewed.

4.1 Experimental Conditions

The experimental settings of the ANKE spectrometer, namely the beam momentum $p_{\rm beam}$, the inclination angle $\alpha_{\rm ANKE}$ of the COSY beam in the ANKE magnet system, the maximum magnetic field $B_{\max}$ in the ANKE dipole D2, and the integrated luminosity L^{int} during the run in February 2001, discussed in Sec. 4.2, are listed in Table 4.1.

$p_{\rm beam}$ [GeV/c]	1.219	1.342	1.463	1.639	2.087	2.679
$\alpha_{\rm ANKE}$ [°]	7.4	7.4	7.4	7.4	7.4	7.4
$B_{\max}$ [T]	0.6771	0.7464	0.8138	0.9123	1.1667	1.5141
L^{int} [1/pb]	70.9	51.8	42.0	78.1	144.9	135.1

Table 4.1: Experimental conditions during the February 2001 beam time: Beam momenta $p_{\rm beam}$, inclination angle $\alpha_{\rm ANKE}$ of the COSY beam in the ANKE magnet system (see Fig. 2.2), the maximum magnetic field $B_{\max}$ set in the ANKE dipole D2, and the integrated luminosity L^{int} recorded are shown.

In addition, during the January 2001 beam time on a_0^+ production [33] data with a hydrogen cluster jet target at beam energies of 0.5 and 2.65 GeV were collected for calibration purposes. These data allowed us to calibrate the energy losses in the scintillation hodoscope and to apply software corrections to the positions of the multiwire proportional chambers. The data–taking was performed with 10^{10} protons stored in the COSY ring and a target density of about 10^{13} cm^{-2} which provided a typical luminosity of about 5×10^{29} cm^{-2}s^{-1}.

4.2 Luminosity Determination

The integrated luminosity L^{int} was obtained by counting protons, elastically and quasi–elastically scattered at small laboratory angles between 5 and 10 degrees. It is not possible to distinguish these processes experimentally at ANKE, but the momentum resolution achieved enables a clean separation from the meson production continuum. The number of events obtained was compared to a simulation using the calculated small angle $pd \to pX$ cross section. The calculation takes into account the sum of elastic and inelastic terms in closure approximation of the Glauber–Franco theory [55]. The luminosity was determined for 6 beam energies of the February 2001 beam time at T_p = 0.6, 0.7, 0.8, 1.1, 1.4, and 2.0 GeV. The cluster target operation was not stable during that time. Therefore, the luminosity was calculated for each individual run. In this section, the procedure of luminosity determination is described and results and comparisons with other methods are presented.

4.2.1 Diffractive *pd* Scattering Differential Cross Section

The cross sections of the *pd* forward scattering were calculated [56] in the approximation of the Glauber–Franko theory. The *pd* scattering cross section consists of elastic and inelastic terms. The general expression of the cross–section was obtained in closure approximation, which includes the sum over the complete set of final *pn* states. Thereby the final state *pn* interaction is taken into account properly. In order to estimate the obtained accuracy, the cross sections, calculated for elastic *pd* scattering and inclusive $pd \to pX$ scattering within the same framework, were compared with the experimental data of Refs. [57, 58, 59, 60, 61] and [62], respectively, in the appropriate energy and angle ranges (for details about this comparison see Appendix D). The resulting $\chi^2/n.d.f.$=0.85 ($n.d.f.$=64) and $\chi^2/n.d.f.$=0.73 ($n.d.f.$=8), respectively, yield a 7% uncertainty of the cross section values used for the determination of the luminosity.

4.2.2 Selection of pd Diffractive Scattering Events

The event selection of pd forward scattering was done among single track events in the data taken with FD trigger. The horizontal and vertical limitations on the track coordinates at the D2 exit window and a vertical cut on the target position were applied. Because this process has a very large cross section and is not suppressed much by the acceptance of the setup, it can be observed in the momentum and angle–momentum spectra and is thus easily selected. Nevertheless, the energy loss cuts were applied to suppress deuteron background from the $pd \to dn\pi^+$ reaction.

The separation of protons and deuterons by their different energy loss in the forward hodoscope (FH) was achieved using the following method. The particle masses are calculated from the energy loss and momentum for each of the two planes of the FH. In Fig. 4.1a the mass M_1 determined using energy losses in the first plane of the FH vs the mass M_2 determined using energy losses in the second plane of the FH is shown. It is seen that by applying the cut (lines) it is possible to select protons (or deuterons). Such a cut corresponds to a cut in a one dimensional distribution of the minimal mass $M_{min} = min(M_1, M_2)$ (Fig. 4.1b). In Fig. 4.2 distributions of the energy losses in the FH vs momentum are shown for different cuts on the minimal mass distribution to select protons and deuterons.

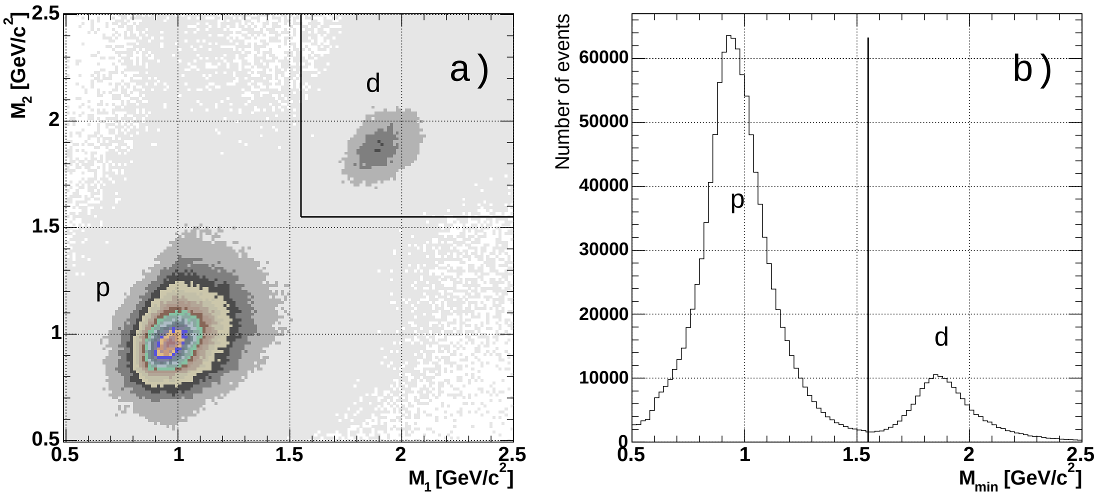

Figure 4.1: Proton and deuteron separation by energy loss: a) Particle mass calculated by energy loss in the first plane of the FH vs the mass calculated by energy loss in the second plane. b) Minimal mass distribution.

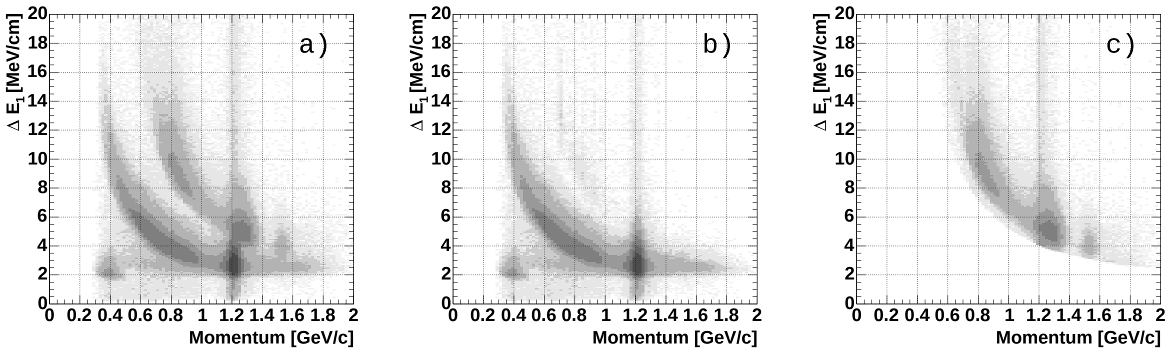

Figure 4.2: Distributions of energy losses in the FH vs momentum for different criteria: a) for all particles, b) for protons selected by minimal mass criterion, c) for deuterons selected by minimal mass criterion.

After selection of protons by energy loss the momentum spectra in different polar angle intervals of 0.2° width in the range $\theta_{lab} = 5.6° - 9.6°$ were analyzed. The peak region of the momentum spectra was fitted by the sum of a Gaussian distribution and a straight line, and events were selected within $\pm 2\sigma$ from the fitted mean momentum value. In Fig. 4.3 an example of such a fit is shown.

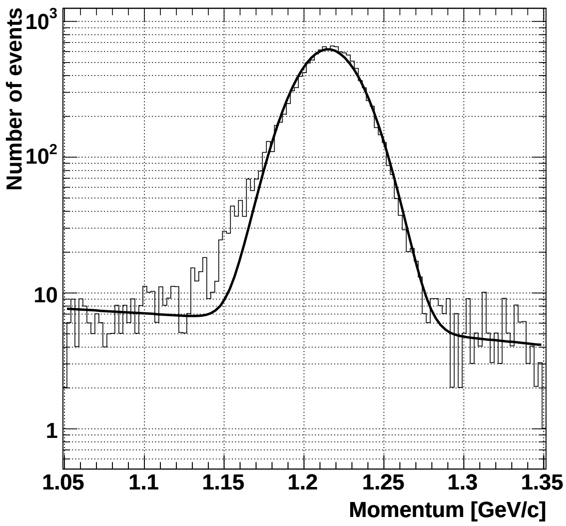

Figure 4.3: Momentum spectrum of protons from pd diffractive scattering at $T_p = 0.6$ GeV after selection by energy losses.

The deviation from a Gaussian at the low end of the momentum distribution was observed (Fig. 4.3) at all energies. This effect is related to the fact that the momentum distribution for inelastically scattered protons is slightly shifted in comparison with elastic *pd* events. A correction factor of 1.025 ± 0.010 was introduced to take this effect into account. Subsequently the counting rates for the different polar angles were calculated taking into account the DAQ dead time correction. It should be stressed that the same correction factors arise in counting of the particles used for the luminosity determination and in counting the breakup proton pairs. Therefore, the corrections completely compensate each other for the breakup cross section determination. Nevertheless, in order to provide the absolute values of the luminosity the dead time corrections were applied during the luminosity determination. The dead time depended on the trigger conditions and ranged from 10%–50%.

4.2.3 Acceptance Calculations

The FD acceptance was calculated using a GEANT–based simulation program, that includes a realistic description of the D2 dipole and the FD. Events with *pd* elastic kinematics were generated in a polar angle interval of forward emitted protons ranging from $\theta_{lab} = 0° - 20°$ where the azimuth ϕ was randomly distributed in the range of $0 - 2\pi$. The criteria for accepting an event during the simulation were:

- Particles emitted do not hit constructional elements of D2, in particular the poles of the magnet.

- Particles exit through the forward window of D2.

- Particles cross the sensitive region of the forward MWPCs, that is, the number of hit wires calculated from the track intercept is in the valid range.

- Particles cross the first and the second plane of the FD hodoscope, which corresponds to the hardware trigger condition.

As a result we obtained the acceptance as a function of the polar angle, shown in Fig. 4.4a. The limiting values of θ coincide well with experimental data. For the luminosity determination the range $\theta_{lab} = 5.6 - 9.6°$ was chosen, where the acceptance changes smoothly. For this angular range the acceptance was calculated with high statistical accuracy (Fig. 4.4b).

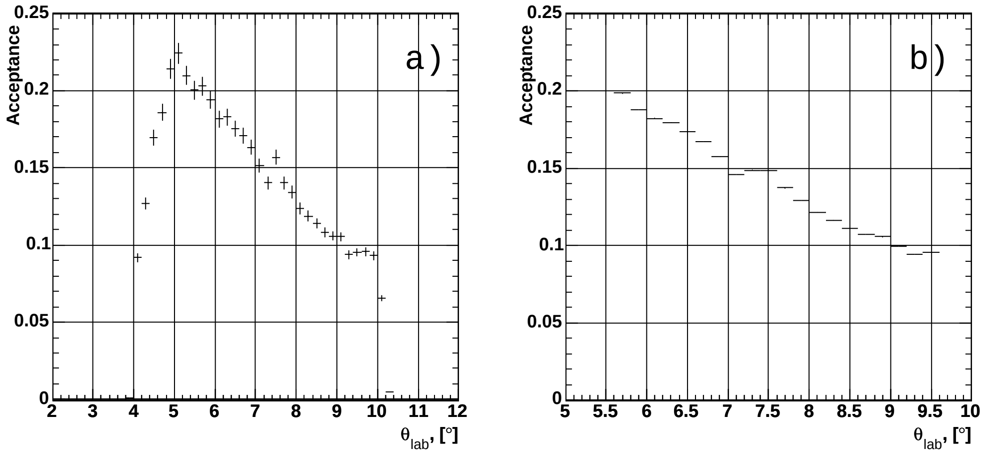

Figure 4.4: FD acceptance for pd elastic scattering: a) acceptance in the full angular range, b) precisely calculated acceptance in the chosen angular range $\theta_{lab} = 5.6 - 9.6$.

4.2.4 Results of Luminosity Determination

Finally, using count rates and theoretically calculated differential cross sections, corrected to the FD acceptance, the luminosity for the different polar angle bins was determined. In Fig. 4.5 the dependence of the luminosity on the polar angle is shown.

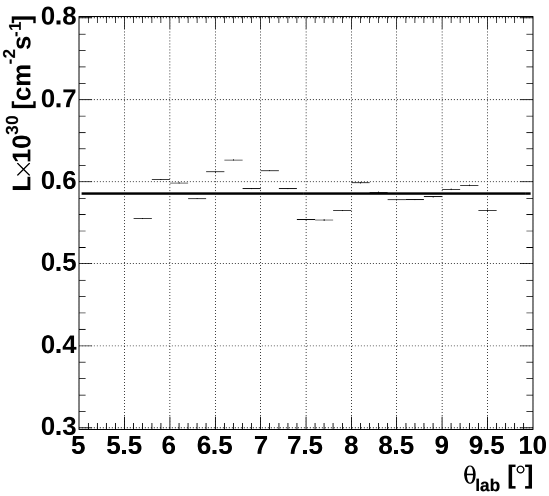

Figure 4.5: Luminosity angular dependence. The solid line shows the mean value of the luminosity.

Averaging the luminosity over the polar angle interval the mean luminosities values are obtained, which are listed in Table 4.2. The errors correspond to the root mean squared deviations of the luminosities determined for individual angle bins from the expected constant value. These errors were considered as one source of systematic uncertainties. All systematic uncertainties from different sources are listed in Table 4.2. The statistical errors are negligible in comparison with the systematic ones.

T_p, GeV	σ_1^L [%]	σ_2^L [%]	σ_3^L [%]	σ_4^L [%]	σ_{tot}^L [%]	$L \times 10^{30}$ [cm^{-2}s^{-1}]
0.6	3.6	7	3	1	8.5	0.59 ± 0.05
0.7	3.8	7	3	1	8.6	0.36 ± 0.03
0.8	3.9	7	3	1	8.6	0.40 ± 0.03
0.95	4.1	7	3	1	8.7	0.35 ± 0.03
1.35	3.6	7	3	1	8.5	0.45 ± 0.04
1.9	4.2	7	3	1	8.8	0.51 ± 0.04

Table 4.2: Systematic uncertainties of the luminosity determination: σ_1^L is the rms value of the squared variation observed in the angular dependence of the luminosity, σ_2^L is the accuracy of the theoretical calculation of the $pd \to pX$ differential cross section, which is discussed in detail in Appendix D, σ_3^L is the error of the efficiency correction of the MWPC, σ_4^L is the error of the correction factor for the low–momentum cut in the momentum spectra (Fig. 4.3).

4.2.5 Comparison with Other Methods

For comparison of the luminosity determination two cross checks were performed. One cross check at a beam energy $T_p = 1.9$ GeV could make use of the silicon–detector telescope (ST). The forward trigger alone allowed us to determine the luminosity using *pd* diffractive scattering and simultaneously *pd* elastic scattering with detection of protons in the FD and deuterons in the ST. The method of luminosity determination by *pd* elastic scattering was used for the ω production experiment [63]. The results of the luminosity determination by *pd* diffractive scattering are shown in the second column of Table 4.3. In the third column the results of the luminosity determination using *pd* elastic scattering are shown. The obtained values of the luminosity for the different methods agree well within errors.

Run number	$L \times 10^{30}$ [cm^{-2}s^{-1}] ($pd \to pX$)	$L \times 10^{30}$ [cm^{-2}s^{-1}] ($pd \to pd$)
3407	0.30 ± 0.03 (sys)	0.24 ± 0.03 (stat) ± 0.05 (sys)
3408	0.43 ± 0.04 (sys)	0.36 ± 0.03 (stat) ± 0.07 (sys)
3409	0.36 ± 0.03 (sys)	0.34 ± 0.03 (stat) ± 0.07 (sys)
3410	0.70 ± 0.07 (sys)	0.71 ± 0.05 (stat) ± 0.14 (sys)
3411	1.21 ± 0.11 (sys)	1.14 ± 0.07 (stat) ± 0.22 (sys)

Table 4.3: Comparison of two methods of luminosity determination at a beam energy of $T_p = 1.9$ GeV.

Another cross check at beam energies of $T_p = 0.6$ and 0.8 GeV used the $pd \to dp$ process. Events of pd backward elastic scattering were selected after identification of deuterons in the FD by energy loss (Fig. 4.2c). Clear peaks in the deuteron momentum spectra are observed for different angular bins. As an example, in Fig. 4.6 the momentum spectrum is shown for the angular range of $\theta_{lab} = 10° - 11°$.

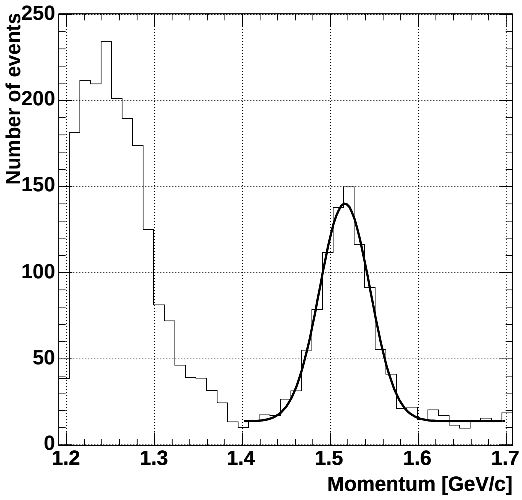

Figure 4.6: Momentum spectrum of deuterons from pd backward scattering at $T_p = 0.6$ GeV for the angular range of $\theta_{lab} = 10° - 11°$.

For normalization the experimental data on the differential cross section at beam energies of $T_p = 0.6$ [64] and 0.8 GeV [65] were used. In Table 4.4 the comparison of the results using the two methods is shown. The obtained values of the luminosity agree well within errors.

T_p [GeV]	$L \times 10^{30}$ [cm^{-2}s^{-1}] ($pd \to pX$)	$L \times 10^{30}$ [cm^{-2}s^{-1}] ($pd \to dp$)
0.6	0.59 ± 0.05 (sys)	0.56 ± 0.01 (stat) ± 0.08 (sys)
0.8	0.40 ± 0.03 (sys)	0.38 ± 0.01 (stat) ± 0.05 (sys)

Table 4.4: Comparison of two methods of luminosity determination at beam energies of 0.6 and 0.8 GeV.

4.3 Simulation of the $pd \to (pp)n$ Process and Acceptance Corrections

The kinematics of a reaction with a three–body final state 2 → 3 is defined by 5 independent variables. For the deuteron breakup reaction the following ones were chosen: excitation energy of the two protons E_{pp}, the polar angle of the proton pair in the c.m. system $\theta_{pp}^{c.m.}$, the azimuthal angle of the proton pair in the c.m. system $\phi_{pp}^{c.m.}$, the polar angle of one proton in the rest frame of the two protons $\theta_k^{c.m.}$, the azimuthal angle of one proton in the rest frame of the two protons $\phi_k^{c.m.}$. In order to provide the event simulation these 5 variables were generated randomly in the following ranges: $E_{pp} \in \{0 < E_{pp} < 3\text{ MeV}\}$, $\cos\theta_{pp}^{c.m.} \in \{0.99 < \cos\theta_{pp}^{c.m.} < 1\}$, $\phi_{pp}^{c.m.} \in \{0 < \phi_{pp}^{c.m.} < 360°\}$, $\cos\theta_k^{c.m.} \in \{0 < \cos\theta_k^{c.m.} < 1\}$, $\phi_k^{c.m.} \in \{0 < \phi_k^{c.m.} < 360°\}$.

Each of the generated events was transformed to the laboratory system by kinematics of the $pd \to ppn$ process at a fixed beam energy T_p. Two protons with momenta $\vec{p}_1$ and $\vec{p}_2$ were traced through the ANKE dipole magnet D2 and the forward detector using the GEANT code. Multiple scattering, energy loss, and nuclear interactions of the protons have been taken into account during the tracing. All the events were checked for passing through the magnet, crossing the sensitive planes of the MWPCs and the counter planes of the forward detector scintillation hodoscope. The results were written into an output file. It allows one to calculate the acceptance as a function of different quantities with variable binning using the same event file without repetition of the time consuming part of the calculation, namely the tracing with GEANT. Thus, taking the chosen bin "b" in the 5–dimensional phase space, one can find the ratio $A_b = N_b^{acc}/N_b^{tot}$, where N_b^{tot} is the total number of events generated in the bin and N_b^{acc} is the number of accepted events. In this way, the acceptance A as a surface $A(E_{pp}, \cos\theta_{pp}^{c.m.}, \phi_{pp}^{c.m.}, \cos\theta_k^{c.m.}, \phi_k^{c.m.})$ in the 5–dimension phase space is obtained. The acceptance was obtained for each beam energy by generation of 10^8 events. The acceptance as a function of a specific variable is the projection of the surface A on this variable axis. The obtained one–dimensional acceptances for E_{pp} and $\cos\theta_{pp}^{c.m.}$ are shown for 0.6 GeV in Fig. 4.7 a), c) and for 1.9 GeV in Fig. 4.7 b), d). It is observed that the acceptance changes substantially within the considered range of the variables, so that an acceptance correction is absolutely mandatory to determine the differential cross sections.

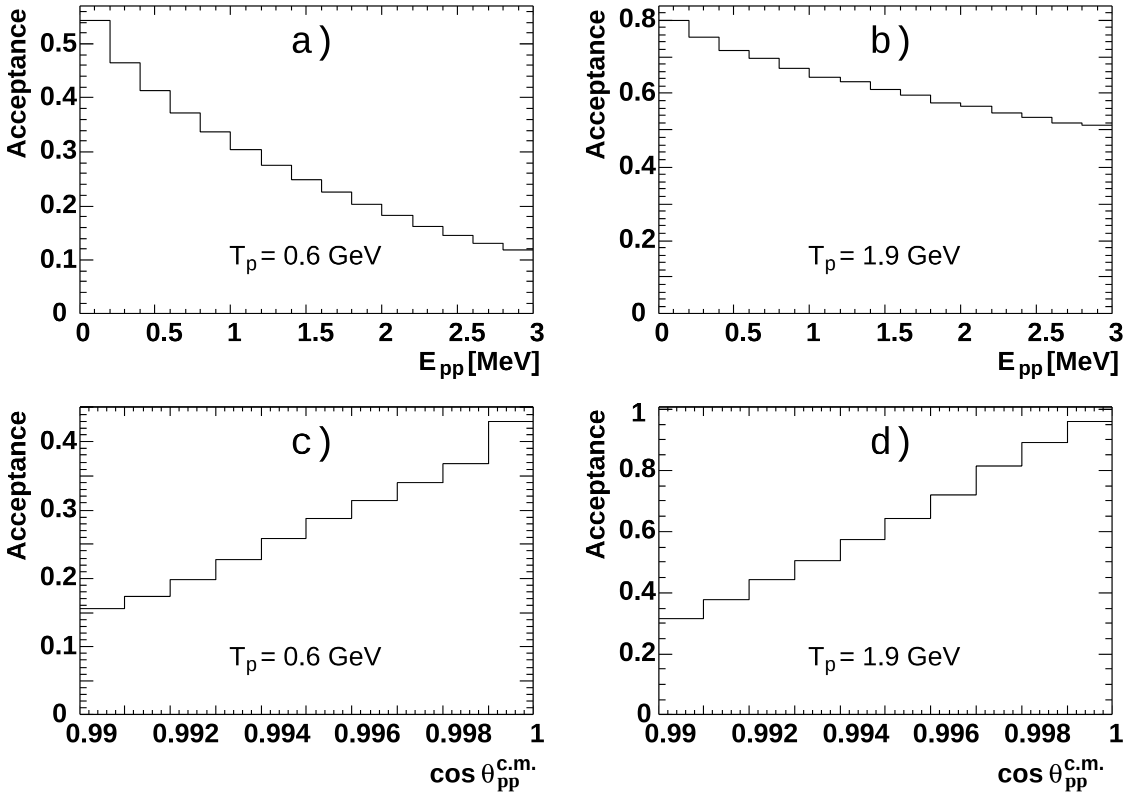

Figure 4.7: One–dimensional acceptances as a function of E_{pp} and $\cos\theta_{pp}^{c.m.}$ for $T_p =$ 0.6 GeV (a, c) and 1.9 GeV (b, d).

In the case of an unpolarized proton beam and spin–averaged measurements of the final protons in ${}^1S_0$ state one can consider the cross section distribution over $\phi_{pp}^{c.m.}$, $\cos\theta_k^{c.m.}$, and $\phi_k^{c.m.}$ as isotropic, i.e. independent of these variables. Therefore, we can restrict the determination of the cross sections to two variables: E_{pp} and $\cos\theta_{pp}^{c.m.}$. The assumed independence of the cross section on $\phi_{pp}^{c.m.}$, $\cos\theta_k^{c.m.}$, and $\phi_k^{c.m.}$ allows one to take out the cross section from the integral over these variables. For this reason all the following considerations were performed with a two–dimensional acceptance correction function only. In Fig. 4.8 an example of the acceptance function calculated for a beam energy $T_p = 0.6$ GeV is shown.

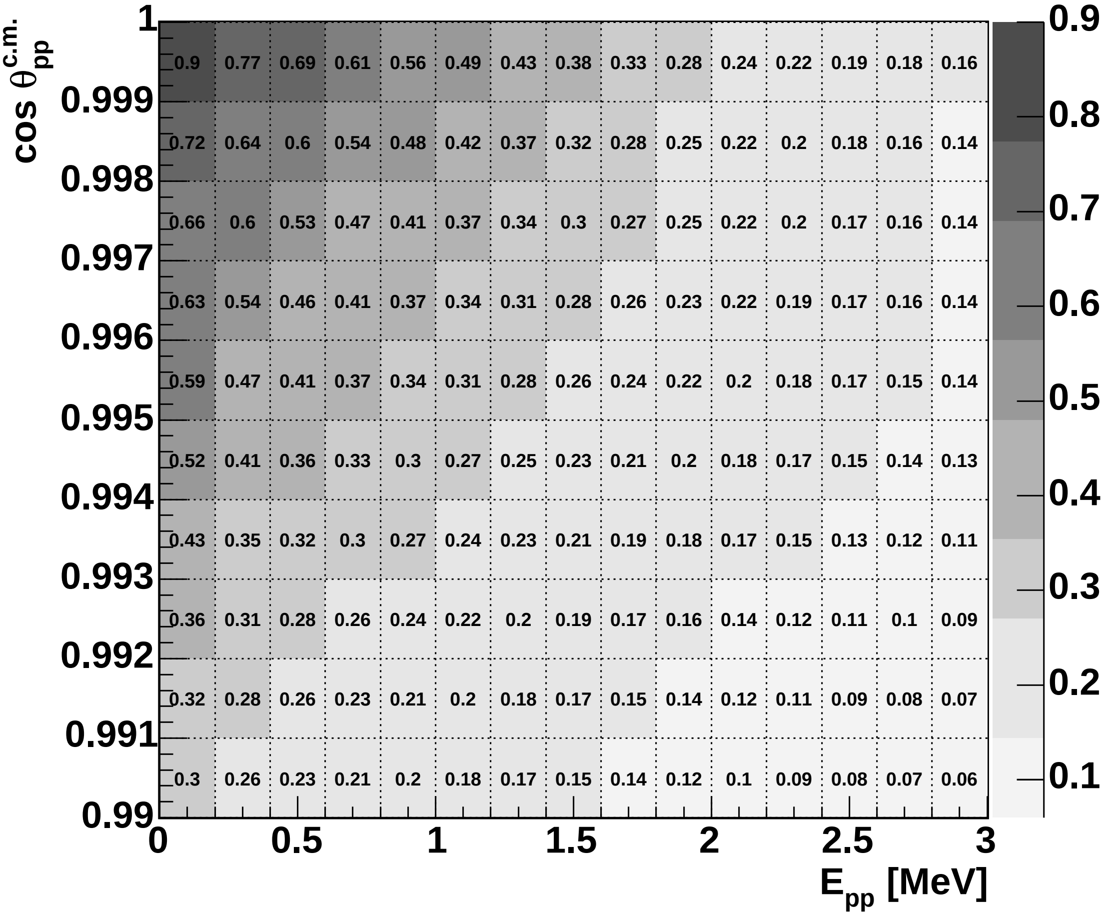

Figure 4.8: Acceptance as a function of E_{pp} and $\cos\theta_{pp}^{c.m.}$ at beam energy of 0.6 GeV. The numbers in the boxes indicate the acceptance value.

The differential cross section is thus expressed by

$$\frac{d\sigma}{dE_{pp}\ d\cos\theta_{pp}^{c.m.}} = \frac{d\sigma^{obs}}{dE_{pp}\ d\cos\theta_{pp}^{c.m.}} \cdot \frac{1}{A(E_{pp}, \cos\theta_{pp}^{c.m.})}.$$

There is one significant effect which can cause substantial distortions of the results in the employed acceptance correction procedure. In case of poor statistics of the measured events and in presence of large values of the acceptance correction factor $1/A$ in the bins with very low statistics, the fluctuation of the result can be magnified by the correction procedure. Therefore, the procedure can produce systematic errors in the determined cross sections. To eliminate this systematic effect a special simulation has been performed. A fixed number of events N_{ini} was generated with a distribution over the kinematical variables extracted from experimental data. Then the number of events in each bin in two–dimensional space E_{pp}, $\cos\theta_{pp}^{c.m.}$ was multiplied by the value of the acceptance function in this bin and counts were simulated according to a Poisson distribution. As a result the number of accepted events N_{acc} was distributed according to a Poisson law. In this simulation the mean number of events N_{acc} was chosen to equal the number of registered deuteron breakup events at each beam energy. For these simulated events the acceptance correction procedure was applied and the obtained number of events N_{cor} was compared with N_{ini}. This procedure was repeated 10000 times. The obtained number of events N_{cor} was found to be distributed according to a Poisson law with mean values equal to N_{ini} and σ_{cor} which is larger slightly than expected from the purely statistical error σ_{ini}. In Table 4.5 the values of these errors are shown for six beam energies. The systematic uncertainties of the acceptance correction procedure can be extracted using $\sigma_{sys} = \sqrt{\sigma_{cor}^2 - \sigma_{ini}^2}$.

T_p [GeV]	N_{acc}	σ_{cor} [%]	σ_{ini} [%]	σ_{sys} [%]
0.6	339	5.87	5.43	2.23
0.7	227	7.37	6.64	3.19
0.8	305	6.23	5.73	2.42
0.95	112	10.34	9.45	4.19
1.35	16	27.17	25.00	10.64
1.90	9	35.97	33.33	13.52

Table 4.5: Systematic uncertainties of the acceptance correction procedure. The number of accepted events N_{acc} used in the simulation, the relative error of the number of events obtained after acceptance correction σ_{cor}, the pure statistical relative error σ_{ini} expected from the simulation, and the extracted systematic uncertainty $\sigma_{sys} = \sqrt{\sigma_{cor}^2 - \sigma_{ini}^2}$ of the acceptance correction procedure are listed.

4.4 Identification of the $pd \to (pp)n$ Reaction

Protons from the breakup process $pd \to ppn$ with an excitation energy $E_{pp} < 3$ MeV could be detected with the experimental setup for laboratory polar angles between 0 and 7° at all energies. Among those events with two registered particles, breakup events are identified by the determination of the missing–mass value, calculated under the assumption that these particles are protons. At all energies the missing–mass spectra reveal a well defined peak at the neutron mass with an rms value of about 20 MeV/c^2 (Fig. 4.9). The peak is clearly separated from the one at 1.1–1.2 GeV/c^2, caused by proton pairs from the $pd \to pp\pi^0 n$ or $pd \to pp\pi^- p$ reactions.

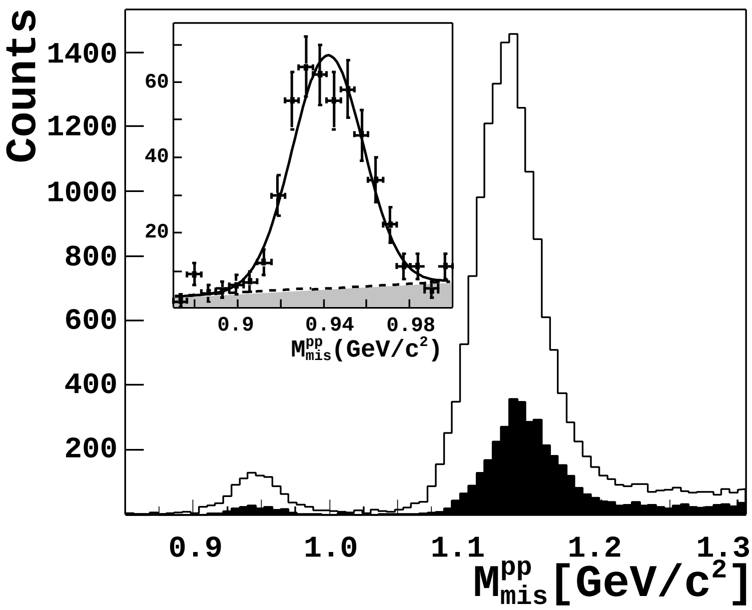

Figure 4.9: Missing–mass distribution at $T_p = 0.8$ GeV of all identified proton pairs (unfilled histogram). The black histogram denotes identified pp pairs with excitation energy of less than 3 MeV. The inset shows the distribution near the neutron mass without particle identification for pairs with $E_{pp} < 3$ MeV. The background contribution is shown in grey.

A direct identification of the particle type is possible for those events for which the two particles hit different counters in the hodoscope. These amount to about 60% of all events in the peak at the neutron mass. For $E_{pp} < 3$ MeV, the fraction varies from 60 to 22% for $T_p = 0.6$ to 1.9 GeV. The time–of–flight (TOF) difference Δt_{meas} measured in the hodoscope was compared to the difference $\Delta t_{tof}(p_1, p_2)$ obtained from the reconstructed particle momenta p_1 and p_2, again assuming that the two particles are protons (as described in Sec.3). Applying a 2σ cut to the peak of the $\Delta t_{meas} - \Delta t_{tof}(p_1, p_2)$ distribution, proton pairs could be selected such that the contribution from other pairs was less than 1%. When both tracks hit the same counter, the energy loss distributions were analyzed and found to be in agreement with the assumption that both registered particles were protons. However, the energy loss cut was not used, since the proton separation from other particles was not quite perfect. In this case we relied on the fact that misidentified pairs ($p\pi^+$, $d\pi^+$, dp or $^3H\pi^+$) show up only at substantially higher missing mass values and therefore cannot contribute to the peak at the neutron mass.

For background subtraction, the spectra in the vicinity of the neutron mass were fitted by the sum of a Gaussian and a straight line (see inset in Fig. 4.9). The number of proton pairs and the signal–to–background ratio $N_{\mathrm{sig}}/N_{\mathrm{bg}}$ were determined in a $\pm 2\sigma$ range around the neutron mass. The distribution of distances between hits by the proton pairs ($E_{pp} < 3$ MeV) in the MWPCs yields rms values of 4.9 and 3.3 cm at 0.6 and 1.9 GeV beam energies, respectively. Therefore, a significant loss of pp pairs due to the two tracks being too close is expected to occur only below $E_{pp} = 0.2$ MeV. Since a resolution of 0.2 (0.3) MeV at $E_{pp} = 0.5$ (3) MeV was achieved, proton pairs with $E_{pp} < 3$ MeV could be reliably selected.

4.5 Energy Dependence of the Cross Section

The data allowed us to deduce the three–fold differential cross sections $d^3\sigma/(d\cos\theta_{pp}^{c.m.} \cdot d\phi_{pp}^{c.m.} \cdot dE_{pp})$, where $\theta_{pp}^{c.m.}$ and $\phi_{pp}^{c.m.}$ are the polar and azimuthal center of mass angles of the total momentum of the pp pair, respectively. The neutron emission angles correspond to $\theta_n^{c.m.} = 180° - \theta_{pp}^{c.m.}$. Figure 4.10 shows the excitation energy distribution of the events for $\theta_{pp}^{c.m.}$ from 0 to 8° and $\phi_{pp}^{c.m.}$ from 0 to 360°, summed over the beam energies 0.6, 0.7, and 0.8 GeV. The shape of the spectrum is well reproduced ($\chi^2/n.d.f.$=0.99) by a phase space distribution multiplied by the Migdal–Watson factor describing the $^1S_0$ final state interaction (fsi) [66] including Coulomb effects.

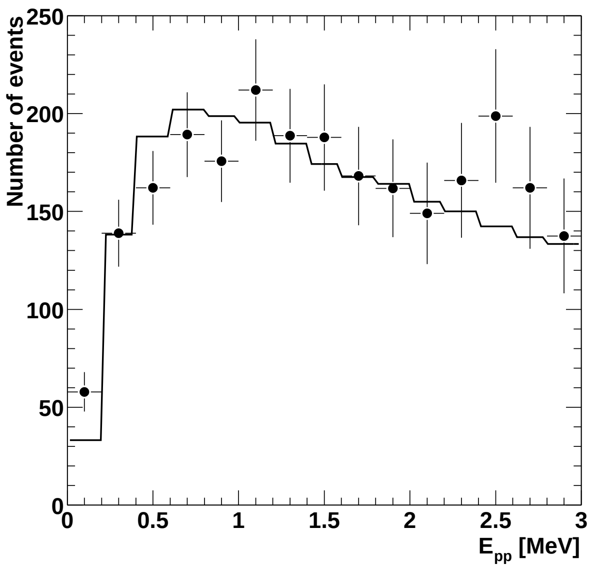

Figure 4.10: Excitation energy distribution in comparison with the theoretical expectation (histogram) from fsi. The deuteron breakup events were summed over the beam energies 0.6, 0.7, and 0.8 GeV.

The event distribution over the cosine of the angle between the relative momentum of the proton pair and its total momentum, shown in Fig. 4.11, is nearly isotropic ($\chi^2/n.d.f.$=1.03), but would allow a few percent of non–isotropic contamination to the differential cross section. From this experimental observation, we can conclude that the two–proton system with $E_{pp} < 3$ MeV is in a relative S–wave ($^1S_0$ state).

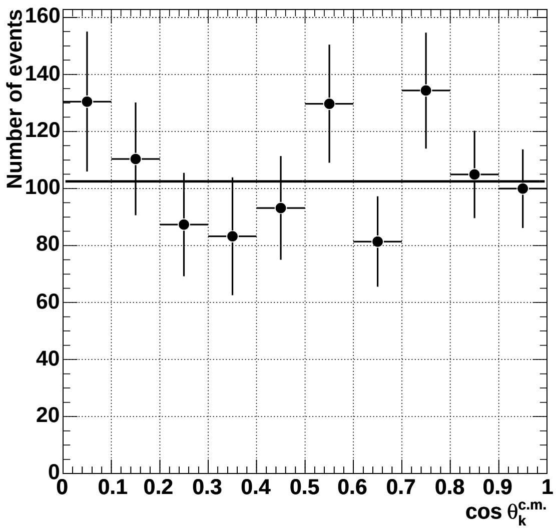

Figure 4.11: The event distribution over the cosine of the angle between the relative momentum of the proton pair and its total momentum at a beam energy T_p = 0.8 GeV for $E_{pp} < 3$ MeV. Solid line shows a polynomial fit to the data.

The counting rates at high energies (1.35 and 1.9 GeV) were rather low. Therefore, in order to present the energy dependence of the process for all measured beam energies, the three–fold cross section was integrated over the interval $0 < E_{pp} <$ 3 MeV and averaged over the angular range $0 < \theta_{pp}^{c.m.} < 8°$, resulting in

$$\overline{\left(\frac{d\sigma}{d\Omega_{pp}^{c.m.}}\right)} = \frac{N_{\rm cor}}{L^{\rm int} \cdot \Delta\Omega_{pp}^{c.m.}} \cdot \frac{N_{\rm sig}}{N_{\rm sig} + N_{\rm bg}} \cdot f \tag{4.1}$$

Here $N_{\rm cor} = \sum_{i=1}^{N} 1/(A_i \cdot \varepsilon_i)$, N is the number of selected proton pairs, A_i and ε_i correspond to acceptance and detector efficiency for registration of the i–th pair. In Table 4.6 a summary of the experimental results is presented. The acceptance was calculated as a function of E_{pp} and $\theta_{pp}^{c.m.}$ assuming a uniform distribution over $\phi_{pp}^{c.m.}$ and isotropy in the two proton system. The average detector efficiency was $\varepsilon \approx 90\%$. The correction factor $f = 1.16 \pm 0.02$ accounts for several soft cuts applied during data processing, 2σ cuts in selection of the process by missing mass and TOF, and track search inefficiency.

T_p [GeV]	L^{int} [$\mathrm{cm}^{-2} \cdot 10^{34}$]	N	N_{cor}	$\frac{N_{\mathrm{sig}}}{N_{\mathrm{sig}}+N_{\mathrm{bg}}}$	$\overline{d\sigma/d\Omega_{pp}^{c.m.}} \pm \sigma^{\mathrm{stat}} \pm \sigma^{\mathrm{syst}}$ [μb/sr]
0.6	1.41±0.12	339	1403	0.94 ± 0.05	$1.72 \pm 0.09 \pm 0.17$
0.7	1.93±0.17	227	872	0.87 ± 0.05	$0.72 \pm 0.05 \pm 0.08$
0.8	2.38±0.20	305	1050	0.89 ± 0.04	$0.72 \pm 0.04 \pm 0.07$
0.95	1.28±0.11	112	337	0.85 ± 0.07	$0.41 \pm 0.04 \pm 0.05$
1.35	0.69±0.06	16	45	0.79 ± 0.22	$0.10 \pm 0.02 \pm 0.03$
1.90	0.74±0.07	9	18	0.62 ± 0.27	$0.03 \pm 0.01 \pm 0.01$

Table 4.6: Summary of the experimental results. T_p denotes the beam energy, L^{int} the integrated luminosity, N the number of events with $E_{pp} < 3$ MeV and pair emission angle $\theta_{pp}^{c.m.} < 8^\circ$, N_{cor} gives the number of events N, corrected for acceptance and detector efficiency, $N_{\mathrm{sig}}/(N_{\mathrm{sig}}+N_{\mathrm{bg}})$ is the background correction, and $\overline{d\sigma/d\Omega_{pp}^{c.m.}}$ denotes the cross section from Eq.(4.1) with statistical errors and systematic uncertainties.

The systematic uncertainties from different sources are listed in Table 4.7. Shown are uncertainties of luminosity (σ_L), uncertainties of the correction factor f accounting for several data processing soft cuts (σ_f), uncertainties of the effect–to–background ratio determination (σ_N), and the uncertainties of the acceptance correction (σ_A).

T_p [GeV]	σ_L [%]	σ_f [%]	σ_N [%]	σ_A [%]	σ_{tot} [%]
0.6	8.5	2.	5.0	2.2	10.3
0.7	8.6	2.	6.0	3.2	11.1
0.8	8.6	2.	5.0	2.4	10.4
0.95	8.7	2.	8.6	4.2	13.0
1.35	8.5	2.	27.8	10.6	31.0
1.90	8.8	2.	43.5	13.5	46.4

Table 4.7: Summary of systematic uncertainties.

4.6 Comparison with Theoretical Predictions

The recently published differential cross section [67] obtained as a function of beam energy is shown in Fig. 4.12.

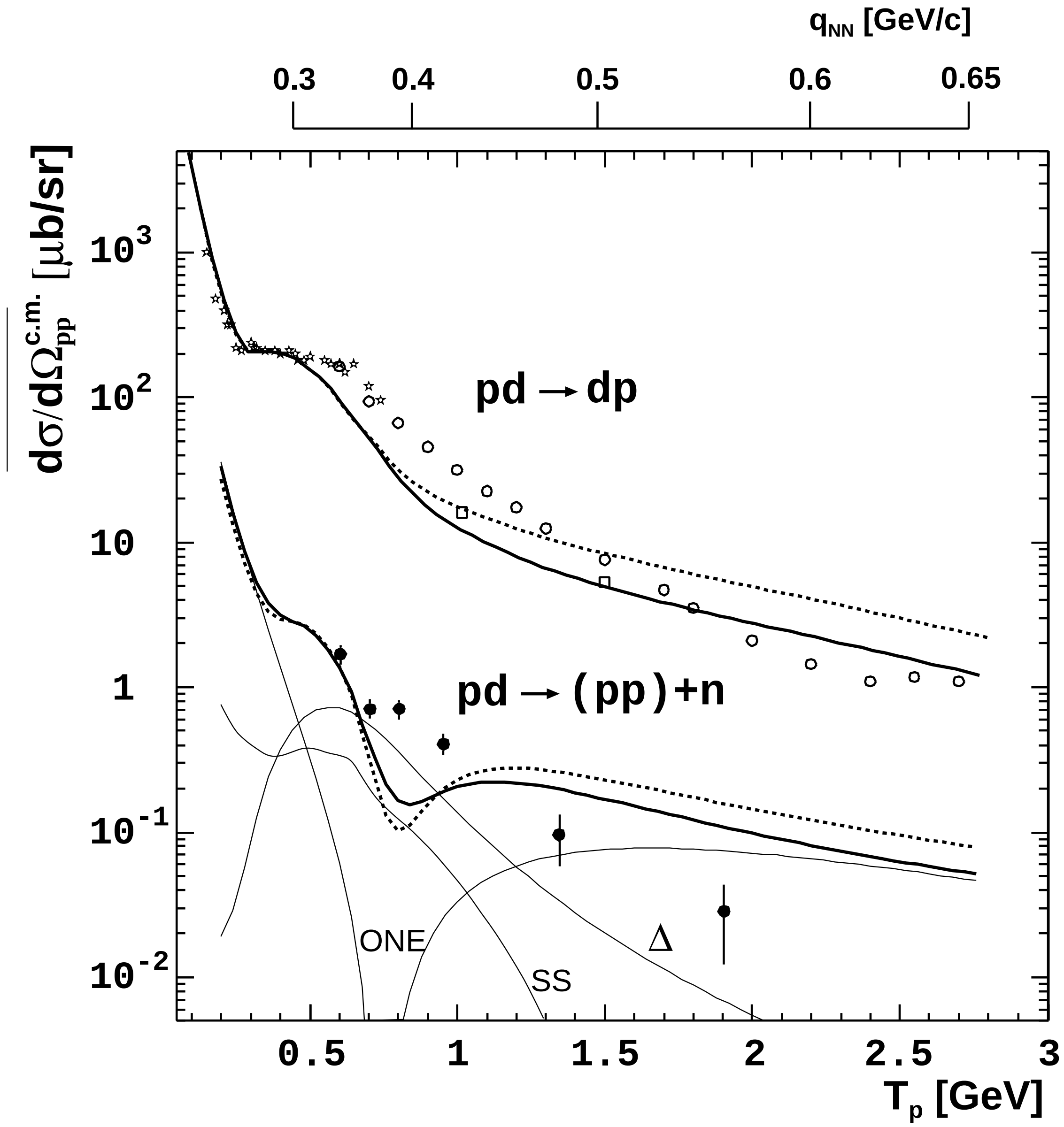

Figure 4.12: Measured cross section of the process $pd \to (pp) + n$ for $E_{pp} < 3$ MeV versus proton–beam energy. The error bars include both statistical and systematic uncertainties (Table 4.6). Shown also are the $pd \to dp$ data ($d\sigma/d\Omega_p^{c.m.}$) taken from Refs. [68, 69, 70]. The calculations with the ONE+SS+Δ model are performed using the NN potentials RSC (dotted line) and Paris (solid) [18] (note also Ref. [73]). The individual contributions of the ONE+SS+Δ model with the Paris potential are shown by thin full lines. The upper scale indicates the internal momentum of the nucleons inside the deuteron for ONE in collinear kinematics at $E_{pp} = 3$ MeV.

The energy dependence of the measured cross section is similar to that of the $pd \to dp$ process, but its absolute value is smaller by about two orders of magnitude. There is no indication for the predicted dip in the breakup cross section. A comparison of the experimental results with the ONE+SS+Δ calculations is shown also. At the lowest energies (0.6–0.7 GeV) the results for the Reid Soft Core (RSC) [71] and the Paris [72] potential reproduce rather well the measured breakup cross section. This energy range corresponds to the region where the $\Delta(1232)$ dominates in the $pd \to dp$ cross section. The theoretical curves for the breakup process exhibit a shoulder at ~ 0.5 GeV as well. This indicates that in spite of the isospin suppression, the contribution from the Δ is still important because of the nearby minimum of the ONE cross section. At higher energies, including the region of the expected dip at 0.7–0.8 GeV, the model is in strong disagreement with the data. One should note that the ONE+SS+Δ model underestimates the $pd \to dp$ cross section in the dip region ($T_p \sim 0.8$ GeV) as well [73]. A possible explanation for this discrepancy is discussed in Ref. [6], where the contributions of NN^* components of the deuteron wave function are evaluated on the basis of a six quark model. Correspondingly for the breakup, effects from N^* exchanges and the contribution of the $\Delta\Delta$ component of the deuteron can possibly increase the cross section in this region and fill the dip. Other sizable contributions may arise from intermediate states of the pp pair at $E_{pp} > 3$ MeV, de–excited by rescattering on the neutron in the final state.

Recently, it was shown in Ref. [74] that the same ONE+SS+Δ model with use of the modern highly–accurate CD Bonn NN potential [75] is in reasonable agreement with our data. The authors show in Ref. [74] that the unpolarized cross section of this reaction is very sensitive to the behavior of the NN interaction at short distances as reflected in the high–momentum components of the deuteron and pp wave functions. Due to the relative smallness of the high momentum component of the CD Bonn wave functions in the ${}^3S_1 -{}^3 D_1$ and ${}^1S_0$ states a much better agreement with the breakup data is achieved than for models with less–soft wave functions like the RSC or Paris potentials (Fig. 4.13).

The role of the relativistic P–wave component that couples to the ${}^1S_0$ state was studied in Ref. [76] in a covariant Bethe–Salpeter approach. According to Ref. [76] the contribution of this P–wave completely masks the dip of the $pd \to (pp)n$ cross section and makes the pp scattering amplitude properly small to achieve agreement with the experiment at higher energies. However, only the ONE mechanism was discussed in Ref. [76] and, moreover, without rescattering effects. The inclusion of the Δ contribution may change the result obtained in Ref. [76] significantly.

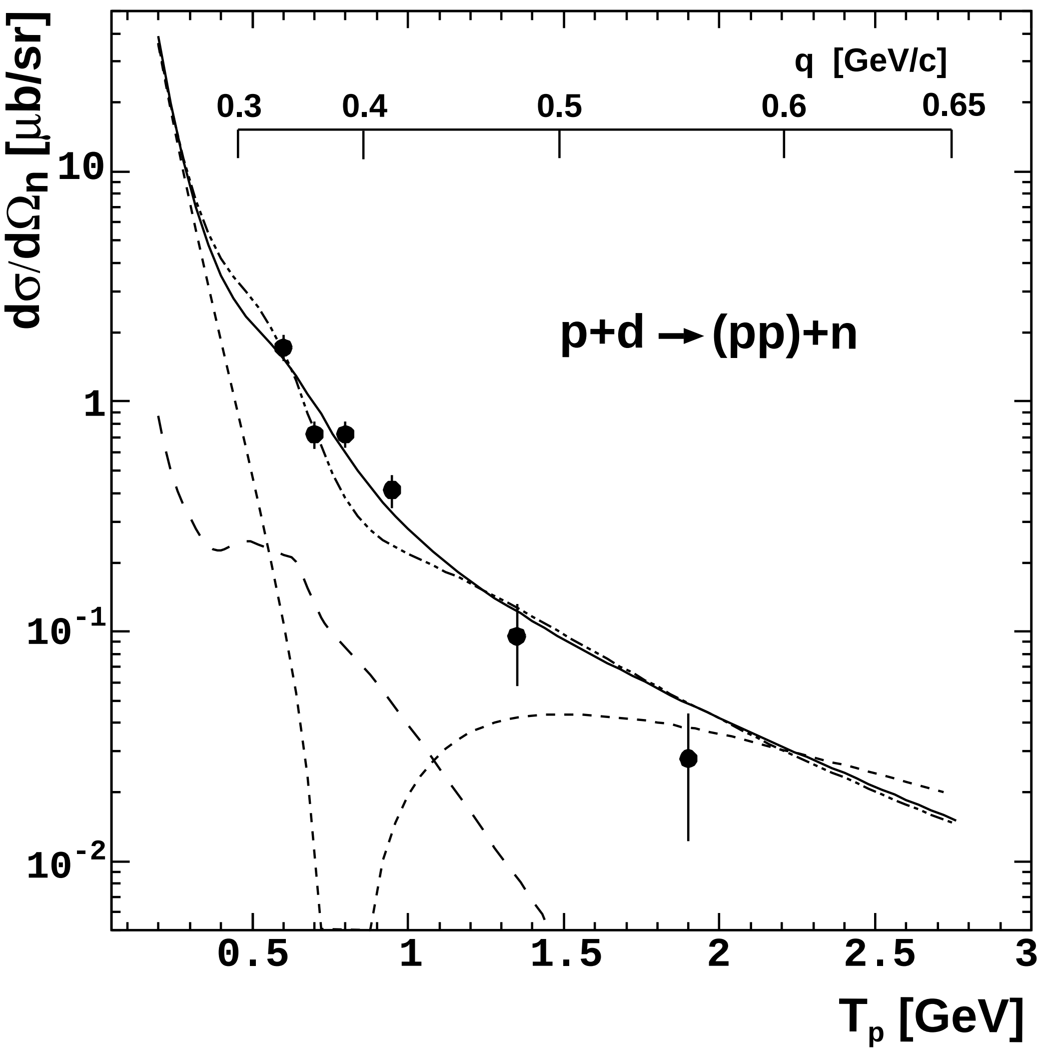

Figure 4.13: Contributions of the reaction mechanisms to the c.m. differential cross section of the reaction $p+d \to (pp)+n$ at neutron scattering angle $\theta_n^{c.m.} = 172-180°$ and relative energies $E_{pp} = 0-3$ MeV of the two forward protons using the CD Bonn NN potential. ONE — short–dashed line; SS — long–dashed line; coherent sum of ONE+Δ with Coulomb effects included — solid line; ONE+SS+Δ with Coulomb effects included — dashed–double dotted line. In the latter two cases distortions in the ONE contribution are also included. The upper scale shows the internal momentum of the nucleons in the deuteron for the ONE [74]

5. Measurement of the Vector Analyzing Power

The vector analyzing power in the reaction $\vec{p}d \to (pp)n$ was measured at the beam energies of 0.5 and 0.8 GeV during the July 2003 beam time. The energies were chosen because the theory predicts [19] a significant change of the analyzing power at these energies. Therefore, the measurement constitutes a sensitive test of validity of the model. In this chapter the notations, the measurement conditions, methods of on–line monitoring and the determination of the absolute beam polarization determination are described. In addition, the obtained experimental results are compared with the theoretical predictions.

5.1 Notations

If the beam is made up of spin–$\frac{1}{2}$ particles with transverse polarization $\vec{\boldsymbol{P}}$, the spin–dependent yield for a reaction induced on an unpolarized target can be written [77] (see Appendix B for details)

$$I(\theta, \phi) = I_0(\theta)(1 + A_y(\theta)\vec{\boldsymbol{P}} \cdot \vec{\boldsymbol{n}}) = I_0(\theta)(1 + A_y(\theta)Pcos\phi),$$

where $I_0(\theta)$ is the unpolarized yield at scattering angle θ, $A_y(\theta)$ is the analyzing power of the reaction, $\vec{n}$ is a unit vector along $\vec{\boldsymbol{k}}_{in} \times \vec{\boldsymbol{k}}_{out}$. The incident and scattered beams have momenta $\vec{\boldsymbol{p}}_{in} = \hbar\vec{\boldsymbol{k}}_{in}$ and $\vec{\boldsymbol{p}}_{out} = \hbar\vec{\boldsymbol{k}}_{out}$, respectively. The symbol ϕ denotes the angle between $\vec{\boldsymbol{P}}$ and $\vec{\boldsymbol{n}}$.

In case of a ϕ–symmetric setup the yield for scattering to the left ($\phi = 0$) is denoted by L and for scattering to the right ($\phi = \pi$) by R, where the direction of $\vec{\boldsymbol{P}} = (P_x, P_y, P_z) = (0, P, 0)$ defines the "up" direction. Then

$$L = I_0(1 + PA_y \cdot cos(\phi = 0)) = I_0(1 + PA_y),$$

$$R = I_0(1 + PA_y \cdot cos(\phi = \pi)) = I_0(1 - PA_y).$$

The asymmetry $\varepsilon(\theta)$ is defined as

$$\varepsilon(\theta) = PA_y(\theta) = \frac{L - R}{L + R}. \tag{5.1}$$

The analyzing power is determined from $A_y = \varepsilon(\theta)/P$.

5.2 Experimental Conditions

The inherent absence of ϕ–symmetry in the experimental setup of the ANKE spectrometer does not permit us to measure a vector analyzing power from the usual determination of the left–right count rate asymmetry from Eq. 5.1. Therefore, we measured the analyzing power by changing the sign of the COSY beam polarization at fixed acceptance of the setup. The sign was alternated every two COSY cycles of 5 min duration each. The asymmetry $\varepsilon(\theta) = PA^p_y(\theta)$ is introduced in this case by

$$\varepsilon(\theta) = A^p_y(\theta) \cdot P = \frac{1}{\overline{(cos\phi)}_\theta} \frac{N_\uparrow(\theta)/L_\uparrow - N_\downarrow(\theta)/L_\downarrow}{N_\uparrow(\theta)/L_\uparrow + N_\downarrow(\theta)/L_\downarrow}. \tag{5.2}$$

Here $N_\uparrow(\theta)/L_\uparrow$ and $N_\downarrow(\theta)/L_\downarrow$ denote the luminosity–normalized numbers of counts for the two orientations of the beam polarization. $\overline{(cos\phi)}_\theta$, defined as the average over all events for the θ interval, reflects the azimuthal spread of the detector acceptance. The measurements with the low energy polarimeter at COSY (Fig. 2.1) show that the absolute value of the beam polarization for up and down orientation was the same with accuracy of $\Delta P = 0.0125$ [78]. The beam polarization up/down inequality affects the measured asymmetry as a first order quantity [79]. The inequality of beam polarization modules defined as $P_{\uparrow(\downarrow)} = P \pm \Delta P$, changes the measured analyzing power by a factor

$$(1 + \Delta P \cdot A^p_y)^{-1}. \tag{5.3}$$

The resulting uncertainty was taken into account during the determination of the analyzing power for all processes described below. The luminosity decreased through a cycle due to the beam–target interaction by not more than $\sim 6\%$. As already discussed in Sec. 2.4, four types of triggers were running in parallel, a prescaled single particle trigger (T_1), a double particle trigger (T_2), a coincidence of a silicon telescope (ST) signal with a non–prescaled T_1 trigger signal (T_3), and a scaler trigger (T_4). Dead time losses of the DAQ cancell in the asymmetry determination by the procedure of luminosity monitoring. The data taking was performed with 3×10^9 protons stored in the COSY ring and target density of about 2×10^{14} which provided a typical luminosity of about 10^{30} cm^{-2}s^{-1}.

5.3 Beam Polarimetry

The absolute value of the beam polarization at 0.8 GeV was determined simultaneously by measuring the asymmetry of elastic $\vec{p}d$ scattering. In order to fix the value of the beam polarization the asymmetry of protons produced by small angle diffractive scattering $\vec{p}d \to pX$ for laboratory angles between 5° and 10° was used.

5.3.1 Relative Luminosity Determination

The luminosity for different signs of the spin orientation was also measured in parallel by counting single protons emitted with momenta ranging from 0.40 to 0.65 GeV/c at 0.5 GeV (0.6 - 1.05 GeV/c at 0.8 GeV) at polar angles close to zero ($0° < \theta \leq 0.5°$ and $0.5° < \theta \leq 1°$). Alternatively, the single protons counted at the azimuthal angles $\phi = 90° \pm 5°$ and $\phi = 270° \pm 5°$ were used. The relative luminosities $f = L_\uparrow / L_\downarrow$ determined by these four independent methods agree well within statistical errors. In Fig. 5.1 the difference between the relative luminosities determined at polar angles $\theta < 1°$ and azimuthal angles ($90° \pm 5°$ and $270° \pm 5°$) is shown for individual runs at beam energy $T_p = 0.8$ GeV. The distribution of differences is compatible with a constant ($\chi^2/n.d.f = 0.99$).

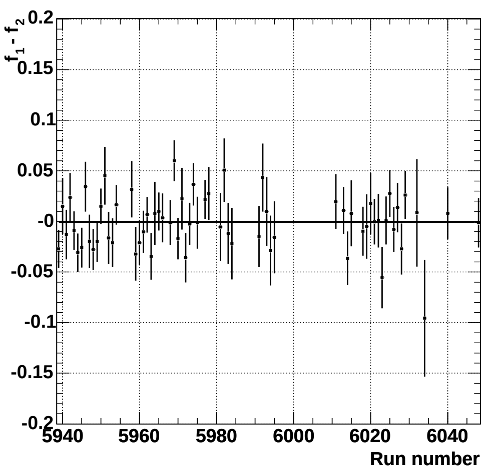

Figure 5.1: The difference between the relative luminosities determined at polar angles $\theta < 1°$ and azimuthal angles ($90° \pm 5°$ or $270° \pm 5°$) as a function of run number at a beam energy of $T_p = 0.8$ GeV.

The typical statistical error of the relative luminosity during a one–hour run is about 0.5%. The systematic uncertainty caused by the relative luminosity was taken into account during the determination of the analyzing power.

5.3.2 Beam Polarization Determination

For the measurement of the absolute value of the beam polarization at ANKE it is necessary to use a process with known analyzing power which can be clearly separated from the background. This can be achieved by a measurement of the asymmetry in small angle $\vec{p}d$ elastic scattering. The asymmetry of $\vec{p}d$ elastic scattering together with the known analyzing power at 0.796 GeV [59], corrected using its energy dependence to account for the small difference in beam energy (4 MeV) yields the beam polarization at 0.8 GeV. The value of this correction ($\Delta A_y^p = -0.0024$), which does not depend upon angle, was obtained using the experimental data at $T_p = 0.796$ GeV [59] and at 0.5 GeV (see Sec. 5.3.4). In Fig. 5.2 a second order polynomial fit ($\chi^2/n.d.f = 0.4$) to the analyzing power data is shown. This polynomial function was used for the determination of the beam polarization.

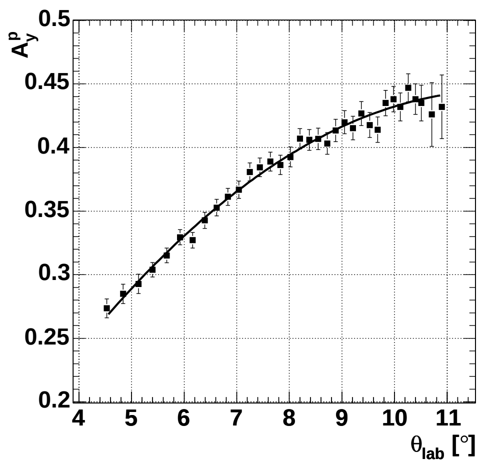

Figure 5.2: The vector analyzing power in $\vec{p}d$ elastic scattering at 0.796 GeV as a function of proton polar angle in the laboratory system [59]. The line shows a second order polynomial fit to the data.

Events of $\vec{p}d$ elastic scattering were identified using the ANKE forward detector (FD) and the silicon telescope (ST), described in Sec. 2.3. In Fig. 5.3 the energy losses in the first layer of the ST vs the energy losses in the second layer (a) and the energy losses in the second layer of the ST vs the energy losses in the third layer (b) are shown. From this correlation one can identify deuterons and protons. The energies of protons and deuterons can be determined for particles stopped in the second or the third layer of the ST. In Fig. 5.4 the energy of the deuteron in the ST vs the polar angle of the proton in the FD is shown.

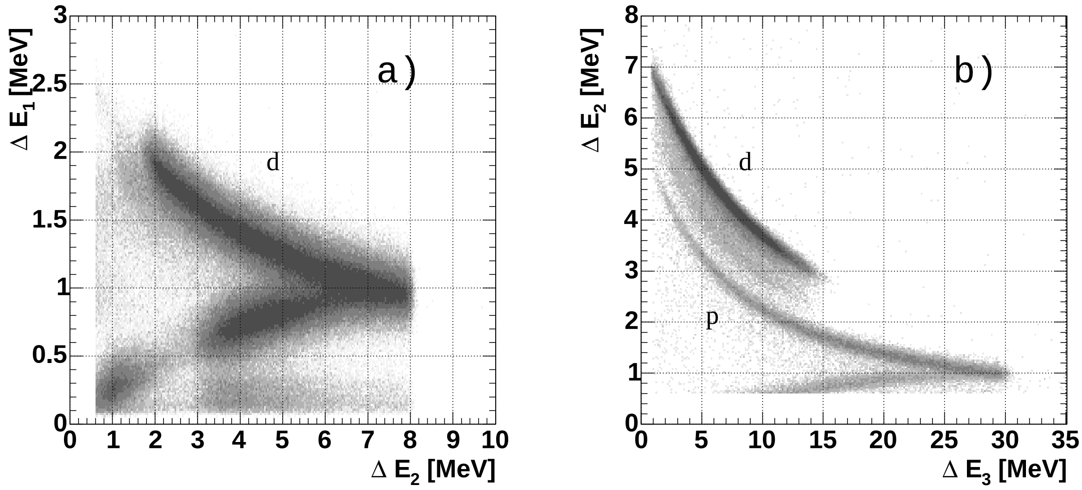

Figure 5.3: Selection of $\vec{p}d$ elastic scattering events at $T_p = 0.8$ GeV: a) Energy losses in the first layer of the ST vs the energy losses in the second layer, b) Energy losses in the second layer of the ST vs the energy losses in the third layer.

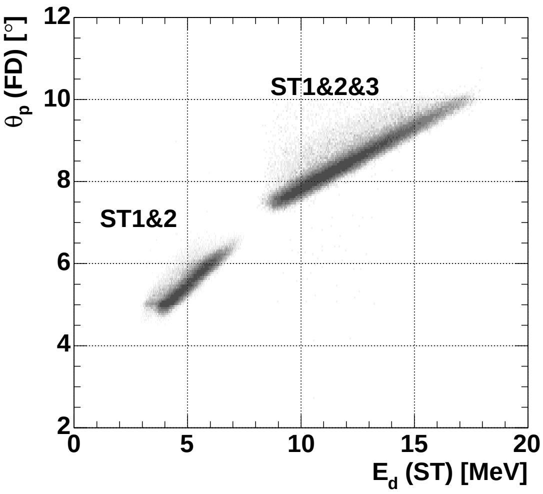

Figure 5.4: Polar angle of the proton in the FD vs energy of the recoil deuteron in the ST at $T_p = 0.8$ GeV. The deuteron energies were determined by energy losses in the first and the second layers of the ST (ST1&2) and energy losses in all tree layers of the ST (ST1&2&3).

The strong correlation of the forward proton and the recoil deuteron results in a well–defined locus, almost free of background. As an example the momentum distribution of protons in the FD in coincidence with deuterons in the ST is shown in Fig. 5.5 for the proton angular range of 8–8.5 degree. The background is negligible.

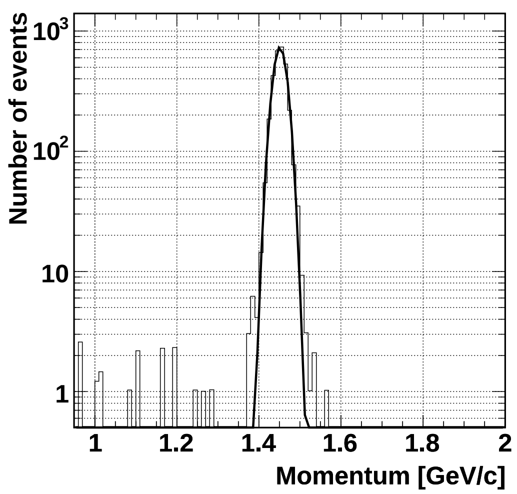

Figure 5.5: Momentum distribution of protons in the FD in coincidence with deuteron in the ST at $T_p = 0.8$ GeV. The proton polar angle is in the range of $8^\circ - 8.5^\circ$.

The two–body kinematics of *pd* elastic scattering allows one to determine either the kinematical parameters of each event from the reconstruction of the 3–momentum of the proton in the FD or alternatively by measuring the energy of deuteron in the ST. The angular resolution of the FD system for protons corresponds to about 0.2°. The ST allows one to measure the energy of deuterons with an accuracy of about 1% which corresponds to an angular resolution of 0.05° for protons. Therefore, the proton scattering angle θ_{lab} was determined from the energy of deuterons measured in the ST. The azimuthal angle ϕ of the proton was determined from the FD, because the ST does not allow one to measure the ϕ angle precisely enough.

For determination of the beam polarization the asymmetry of $\vec{p}d$ elastic scattering was calculated in the angular range $\theta_{lab} = 5^\circ - 10^\circ$ in 0.5° wide angular bins. The obtained value of the asymmetry in each bin was divided by the the value of the analyzing power determined from the polynomial function shown in Fig. 5.2 in the center of the corresponding angular bin. In Fig. 5.6 the beam polarization is shown as a function of laboratory polar angle. The obtained angular dependence of the beam polarization is compatible with a constant ($\chi^2/ndf = 7.57/7$).

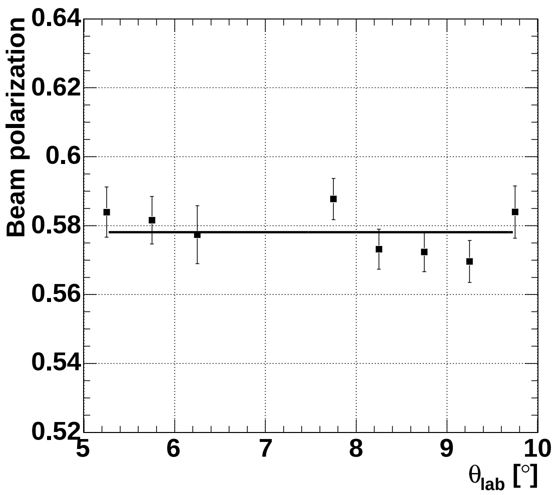

Figure 5.6: Beam polarization at $T_p = 0.8$ GeV as a function of laboratory polar angle. The absence of the data in the angular range $\theta_{lab} = 6.5 - 7.5$ is connected with the acceptance of the ST for selected deuterons (Fig. 5.4).

The resulting average beam polarization during data taking at 0.8 GeV was determined to be

$$P\ (0.8\text{GeV}) = 0.578 \pm 0.002\ (\text{stat}) \pm 0.006\ (\text{syst}).$$

Systematic uncertainty arises from the normalization to the reference data [59], the uncertainty of the proton scattering angle determination from the energy of deuterons measured in the ST, and the uncertainty from the beam polarization up/down inequality.

5.3.3 Measurement of A_y^p in $\vec{p}p$ Quasielastic Scattering

The obtained value of the beam polarization at 0.8 GeV was different from the beam polarization measured at EDDA. The measurements at EDDA were carried out at low beam intensity of about 10^8 during separate runs. A ratio $P_{EDDA}/P_{ANKE} = 1.25 \pm 0.03$ was obtained. There is no explanation of this discrepancy up to now. Because of this inconsistency the beam polarization obtained at ANKE was used in the analysis. However, the measurement of the analyzing power in $\vec{p}p$ quasielastic scattering from the deuteron allowed us to check independently the determination of the beam polarization. At a beam energy of $T_p = 0.8$ GeV the experimental data on the vector analyzing power A_y^p exist for the $\vec{p}p$ elastic and quasielastic scattering at angles in the ANKE acceptance range [81]. $\vec{p}p$ quasielastic events were selected by the detection of one proton in the ST and another proton in the FD. In Fig. 5.3b the selection of protons in the ST is shown. The main background for *pp* quasielastic events consists of *pd* elastic events with deuterons misidentified as protons. The *pd* elastic events were selected by two–body kinematics and excluded from the analysis. In Fig. 5.7 the angular dependence of the measured analyzing power is presented in comparison with existing experimental data [81] on A_y^p in $\vec{p}p$ elastic and quasielastic scattering and results of partial wave analysis calculations [82]. It is seen that our measurement agrees with existing experimental data and the partial wave analysis which confirms our measurement of the beam polarization based on $\vec{p}d$ scattering.

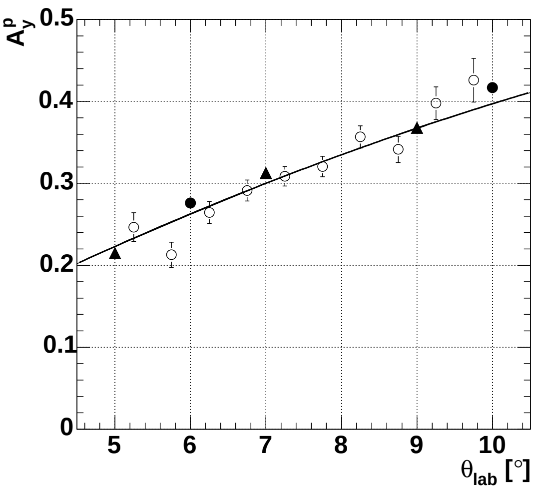

Figure 5.7: Comparison of the angular dependence of the vector analyzing power in quasielastic $\vec{p}p$ scattering measured at ANKE (open circles) at $T_p = 0.8$ GeV with experimental data on A_y^p in $\vec{p}p$ elastic (triangles) and quasielastic (circles) scattering [81] and results of partial wave analysis calculations (curve) for $\vec{p}p$ elastic scattering from [82].

5.3.4 Export of the Beam Polarization

Since there are no analyzing power data available at $T_p = 0.5$ GeV, we used the polarization export technique described in Ref. [80]. A beam cycle with a flat top at 0.8 GeV (I), deceleration of the beam to a flat top at 0.5 GeV (II) and subsequent reacceleration to a flat top at 0.8 GeV (III) was set up (Fig. 5.8).

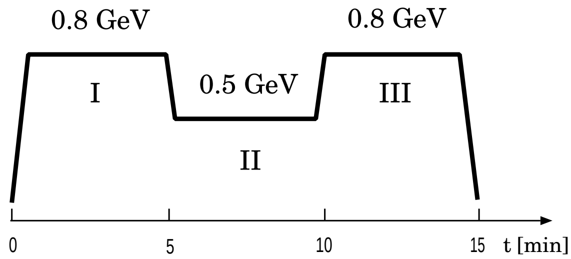

Figure 5.8: Cycle for the beam polarization export.

During the ramps between 0.5 GeV and 0.8 GeV the imperfection resonance at $T_p = 0.6318$ GeV is crossed in COSY (see Appendix C for details). The adiabatic spin flip technique used at COSY allowed us to cross the imperfection resonance without polarization losses. We determined for the beam polarization at the two flat tops at 0.8 GeV $P_I = 0.559 \pm 0.004(stat) \pm 0.006(syst)$ and $P_{III} = 0.555 \pm 0.005(stat) \pm 0.006(syst)$ (Fig. 5.9) using the method described in Sec. 5.3.2. The weighted average of P_I and P_{III} was used to export the beam polarization to the flat top II.

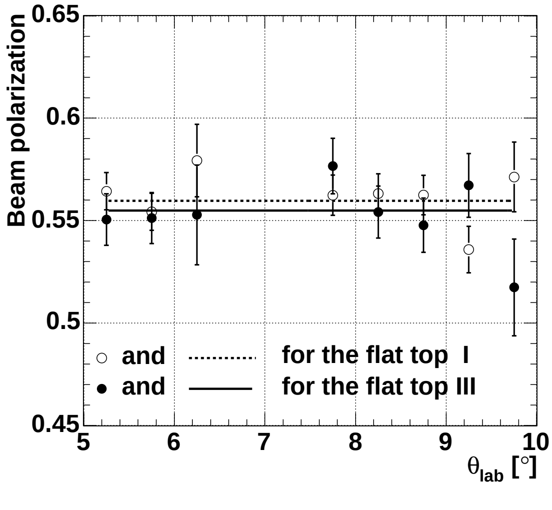

Figure 5.9: Beam polarization measured at the flat top I and the flat top III of the polarization export cycle. Points with error bars depict polarization measured in $\vec{p}d$ elastic scattering at angle θ, lines give the mean values.

In this way, the analyzing power of pd elastic scattering at 0.5 GeV could be determined by the asymmetry measured with a known beam polarization. In Fig. 5.10

the result of the measurement of A_y^p at ANKE at 0.5 GeV is shown. The analyzing power at 0.5 GeV (Table 5.1) was later used for the determination of the beam polarization using cycles consisting of only one flat top. The systematic uncertainty includes the uncertainty of the beam polarization determination during the polarization export cycles, the uncertainty of the proton scattering angle determination from the energy of deuterons measured in the ST, and the uncertainty of the up/down modules inequality of the beam polarization.

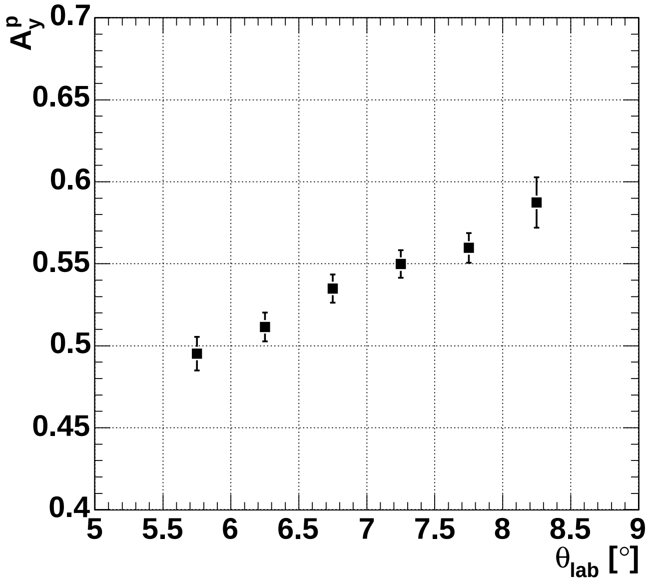

Figure 5.10: Angular dependence of the vector analyzing power in $\vec{p}d$ elastic scattering measured at ANKE at $T_p = 0.5$ GeV.

θ^p_{lab} [°]	$A_y^p \pm \sigma_{stat} \pm \sigma_{syst}$
6.25	$0.495 \pm 0.010 \pm 0.008$
6.75	$0.511 \pm 0.009 \pm 0.008$
7.25	$0.535 \pm 0.009 \pm 0.009$
7.75	$0.549 \pm 0.008 \pm 0.009$
8.25	$0.559 \pm 0.009 \pm 0.009$
8.75	$0.587 \pm 0.015 \pm 0.010$

Table 5.1: Experimental results for A_y^p in pd elastic scattering at 0.5 GeV.

Finally, the average beam polarization at $T_p = 0.5$ GeV during data taking was determined to be

$$P\ (0.5\text{GeV}) = 0.548 \pm 0.003\ (\text{stat}) \pm 0.010\ (\text{syst}).$$

5.3.5 On–line Monitoring of the Beam Polarization

During the experiment the beam polarization was continously monitored using small angle diffractive scattering $\vec{p}d \to pX$. This process was selected by the registration of protons scattered in the FD. The on–line measurement of the asymmetry allowed us to control the relative changes of the beam polarization during our measurements. Due to the high counting rate of protons from $\vec{p}d \to pX$ in the FD the asymmetry could be measured during 10 min with an accuracy of about 3%. After the beam polarization had been determined using $\vec{p}d$ elastic scattering, the vector analyzing power A_y^p in $\vec{p}d \to pX$ process was obtained at the two beam energies $T_p = 0.5$ and 0.8 GeV. The angular dependence of A_y^p is shown in Fig. 5.11 and listed in Table 5.2. The most important systematic uncertainty arises from the uncertainty of the proton scattering angle reconstruction in the FD (0.2°).

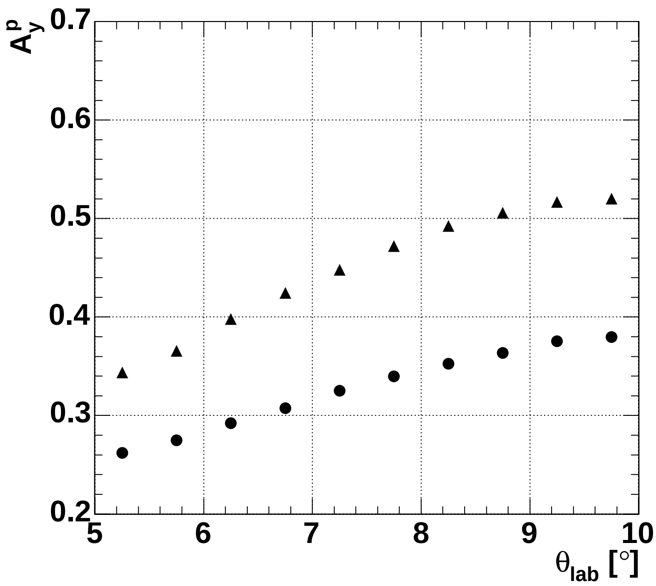

Figure 5.11: Angular dependence of the vector analyzing power in $\vec{p}d \to pX$ small angle diffractive scattering measured at ANKE at $T_p = 0.5$ GeV (triangles) and 0.8 GeV (circles).

θ_{lab} [°]	$A_y^p \pm \sigma_{stat} \pm \sigma_{syst}$ ($T_p = 0.5$ GeV)	$A_y^p \pm \sigma_{stat} \pm \sigma_{syst}$ ($T_p = 0.8$ GeV)
5.25	$0.3436 \pm 0.0011 \pm 0.014$	$0.2620 \pm 0.0004 \pm 0.008$
5.75	$0.3657 \pm 0.0010 \pm 0.013$	$0.2747 \pm 0.0004 \pm 0.008$
6.25	$0.3979 \pm 0.0010 \pm 0.013$	$0.2920 \pm 0.0004 \pm 0.008$
6.75	$0.4246 \pm 0.0010 \pm 0.013$	$0.3076 \pm 0.0004 \pm 0.007$
7.25	$0.4479 \pm 0.0010 \pm 0.013$	$0.3251 \pm 0.0004 \pm 0.007$
7.75	$0.4722 \pm 0.0010 \pm 0.012$	$0.3399 \pm 0.0004 \pm 0.006$
8.25	$0.4926 \pm 0.0010 \pm 0.011$	$0.3526 \pm 0.0004 \pm 0.006$
8.75	$0.5058 \pm 0.0011 \pm 0.010$	$0.3636 \pm 0.0004 \pm 0.006$
9.25	$0.5168 \pm 0.0011 \pm 0.010$	$0.3754 \pm 0.0005 \pm 0.006$
9.75	$0.5201 \pm 0.0012 \pm 0.009$	$0.3798 \pm 0.0005 \pm 0.004$

Table 5.2: Experimental results on A_y^p in $\vec{p}d \to pX$.

5.4 Identification of Deuteron Breakup Events

The procedure of the deuteron breakup event identification was in general quite similar to that used in the cross section measurement. The tracks in the MWPCs were reconstructed using a straight–line approximation and cuts that ensure the tracks passed the exit window of the D2 vacuum chamber. Also cuts over vertical coordinate of the tracks in the target plane were used (see Sec. 3.6 for details).

The breakup is identified as a process with a missing mass for the recorded proton pairs equal to the neutron mass. The missing mass spectra at both energies exhibit a peak at a proper position: $\langle M_{mis} \rangle = 940.0 \pm 0.5$ MeV at 0.5 GeV and 939.9 ± 0.6 MeV at 0.8 GeV. In Fig. 5.12 the missing mass distributions are shown for all pairs with reconstructed 3–momenta and for the proton pairs that pass the time–difference and energy loss conditions (see Sec. 3 for details). The peak width (16 MeV at 0.5 GeV and 19 MeV at 0.8 GeV) allows for its satisfactory separation from the neighboring peak corresponding to missing masses of nucleon plus pion.

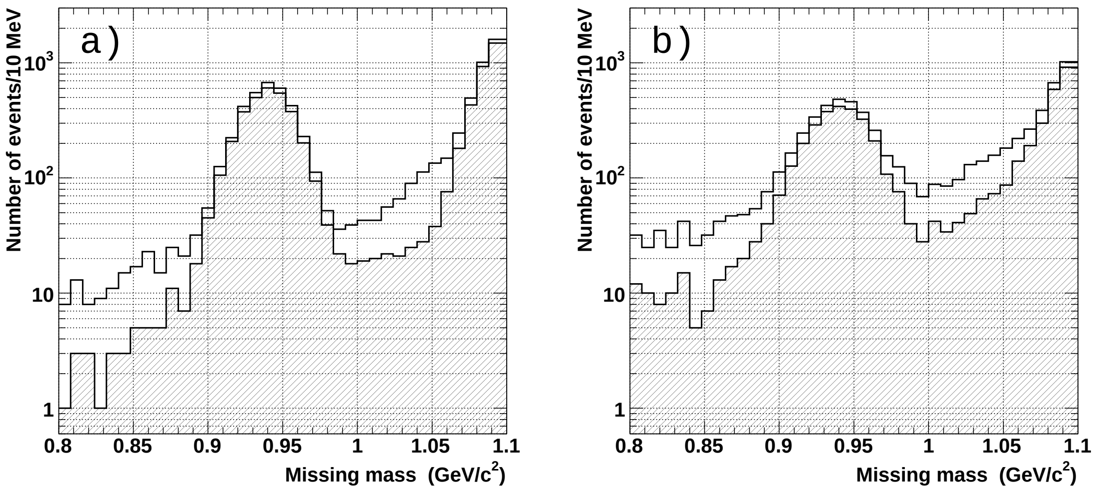

Figure 5.12: Missing mass spectra for the proton pairs with excitation energy $E_{pp} < 3$ MeV at $T_p = 0.5$ (a) and 0.8 GeV (b). The upper histograms show all pairs with reconstructed 3–momenta, while the hatched histograms show the proton pairs that pass the time–difference and energy loss conditions.

5.5 Experimental Results

Scattering and azimuthal angles θ and ϕ of the breakup reaction are determined with respect to the direction of the neutron in the c.m. system. $\vec{p}_n = -(\vec{p}_1 + \vec{p}_2)$ is the neutron momentum, where $\vec{p}_1$ and $\vec{p}_2$ are the momenta of the protons. The resulting yield is integrated over the direction of the relative momenta in the diproton rest frame and over excitation energies up to $E_{pp} = 3$ MeV. We restricted the ϕ interval applying the cut to the neutron azimuthal angle of $\pm 45°$.

To determine the numbers $N_\uparrow$ and $N_\downarrow$ we fitted the corresponding missing mass spectra for the proton pairs with $E_{pp} < 3$ MeV in the 0.88 – 1.01 GeV/c^2 range by the sum of a Gaussian and a straight line. The procedure was performed with the spectra obtained for the pairs without any additional cuts (upper lines in the spectra of Fig. 5.12) and for the pairs selected by the appropriate cuts at the Δt_{meas}, Δt_{tof} scatter plot (see Fig. 3.7) in case different counters were hit and selected by energy loss of the proton pair in case the same counter was hit (lower lines in Fig. 5.12). The background–to–signal ratios, determined from a fit with a Gaussian and straight line, corresponds to 2% at $T_p = 0.5$ GeV and 6% at $T_p = 0.8$ GeV in the 2σ interval.

Since an essential requirement of the experiment consists in a strict independence of the efficiency $E(\theta, \phi)$ from the sign of the beam polarization, we checked to which extent this requirement was fulfilled. The mean value of the elastic/quasielastic peak at all angles was the same within statistical errors. The mean value of the breakup missing mass peak was the same within statistical errors.

The following sources of systematic uncertainties in the asymmetry measurement are important: i) The uncertainty of the neutron angle determination (0.12°). The corresponding uncertainty in the asymmetry σ_θ was taken into account. ii) The uncertainty σ_P of the beam polarization up/down modules inequality discussed in Sec. 5.2. The uncertainty of the relative luminosity determination (Sec. 5.3.1) is negligible. In Table 5.3 the uncertainties are summarized.

	$T_p = 0.5$ GeV		$T_p = 0.8$ GeV	
$\theta_n^{c.m.}$ [°]	σ_θ	σ_P	σ_θ	σ_P
167	0.008	0.0052	0.002	0.0001
169	0.008	0.0025	0.002	0.0002
171	0.008	0.0024	0.002	0.0001
173	0.008	0.0012	0.002	0.0002
175	0.008	0.0010	0.002	0.0001
177	0.008	0.0002	0.002	0.0001
179	0.008	0.0001	0.002	0.0001

Table 5.3: The systematic uncertainties of asymmetry measurement for $pd \to (pp)n$.

In addition, the statistical errors and systematic uncertainties of the beam polarization determination

$$P(0.5\text{GeV}) = 0.548 \pm 0.003(stat) \pm 0.010(syst),$$

$$P(0.8\text{GeV}) = 0.578 \pm 0.002(stat) \pm 0.006(syst).$$

are considered as normalization uncertainty for the analyzing power A_y^p of the $pd \to (pp)n$ reaction.

The obtained angular dependence of A_y^p is given in Table 5.4 and plotted for $T_p =$ 0.5 and 0.8 GeV as a function of $\theta_n^{c.m.}$ in Fig. 5.13. The systematic uncertainties include the uncertainties of the asymmetry determination and the normalization uncertainties. The results in Table 5.4 are presented at the center of 2° angle bins. A correction is necessary because the values at the bin center differ slightly from the measured mean over the bin. For correction calculations it was assumed that the shape of the angular dependence of A_y^p can be taken from the fit of experimental data (without corrections) with a polynomial function. The values of the observables were calculated from this function in 0.2° intervals, and were weighted with the observed total yields in the corresponding 0.2° intervals. The correction is equal to the difference between the mean over the bin and the value from the fitting function at the beam center. The corrections are sizable only where the angular distributions of A_y^p and total yield show large slopes. However, the corrections were applied for all angles to obtained values.

$\theta_n^{c.m.}$ [°]	$A_y^p \pm \sigma_{stat} \pm \sigma_{syst}$ (T_p = 0.5 GeV)	$A_y^p \pm \sigma_{stat} \pm \sigma_{syst}$ (T_p = 0.8 GeV)
167	$0.83 \pm 0.19 \pm 0.020$	$0.12 \pm 0.19 \pm 0.002$
169	$0.56 \pm 0.10 \pm 0.014$	$0.11 \pm 0.11 \pm 0.003$
171	$0.55 \pm 0.08 \pm 0.014$	$0.06 \pm 0.09 \pm 0.002$
173	$0.46 \pm 0.07 \pm 0.011$	$0.14 \pm 0.08 \pm 0.003$
175	$0.35 \pm 0.07 \pm 0.011$	$0.05 \pm 0.09 \pm 0.002$
177	$0.12 \pm 0.09 \pm 0.009$	$0.03 \pm 0.11 \pm 0.002$
179	$-0.07 \pm 0.18 \pm 0.008$	$0.18 \pm 0.19 \pm 0.002$

Table 5.4: Experimental results on A_y^p in $\vec{p}d \to (pp)n$.

A peculiarity of the data at 0.5 GeV is the fast increase of A_y^p in a small angular interval from 180° to 167° up to a value of about 0.9. It should be noted, that the analyzing power of proton–deuteron elastic backward scattering measured [65, 83, 84] at 0.425, 0.68, 0.8 and 1.053 GeV proton energies does not exceed a value of 0.12 in the same angular interval. The second special feature of the data is the drastic decrease of A_y^p as the beam energy is increased from 0.5 to 0.8 GeV. This behavior of the breakup is also very different from that for the $\vec{p}d \to dp$ scattering where the analyzing power at all energies typically reaches values of $A_y^p \simeq 0.3$ before dropping to zero at 180°. There is an apparent tendency for that peak to be shifted towards backward angles at higher energies, but this shift occurs smoothly in contrast to what is observed here for the breakup reaction.

5.6 Comparison with Model Predictions

Figure 5.13 depicts a comparison of the experimental results with the ONE+SS+Δ model [18, 74] calculations. The calculations were performed [85] making use of the CD Bonn NN potentials. The model reproduces the sign of the A_y^p and the decrease from 0.5 to 0.8 GeV although it fails completely to reproduce the magnitude of A_y^p at 0.5 GeV. An improvement of the model by inclusion of the ONE+Δ+SS diagrams with charge exchange in the final state is in progress. An extension of the A_y^p measurements to higher energies is of obvious interest with respect to the determination of the momentum transfer at which the meson–nucleon approach loses its applicability for the description of the proton–deuteron interaction.

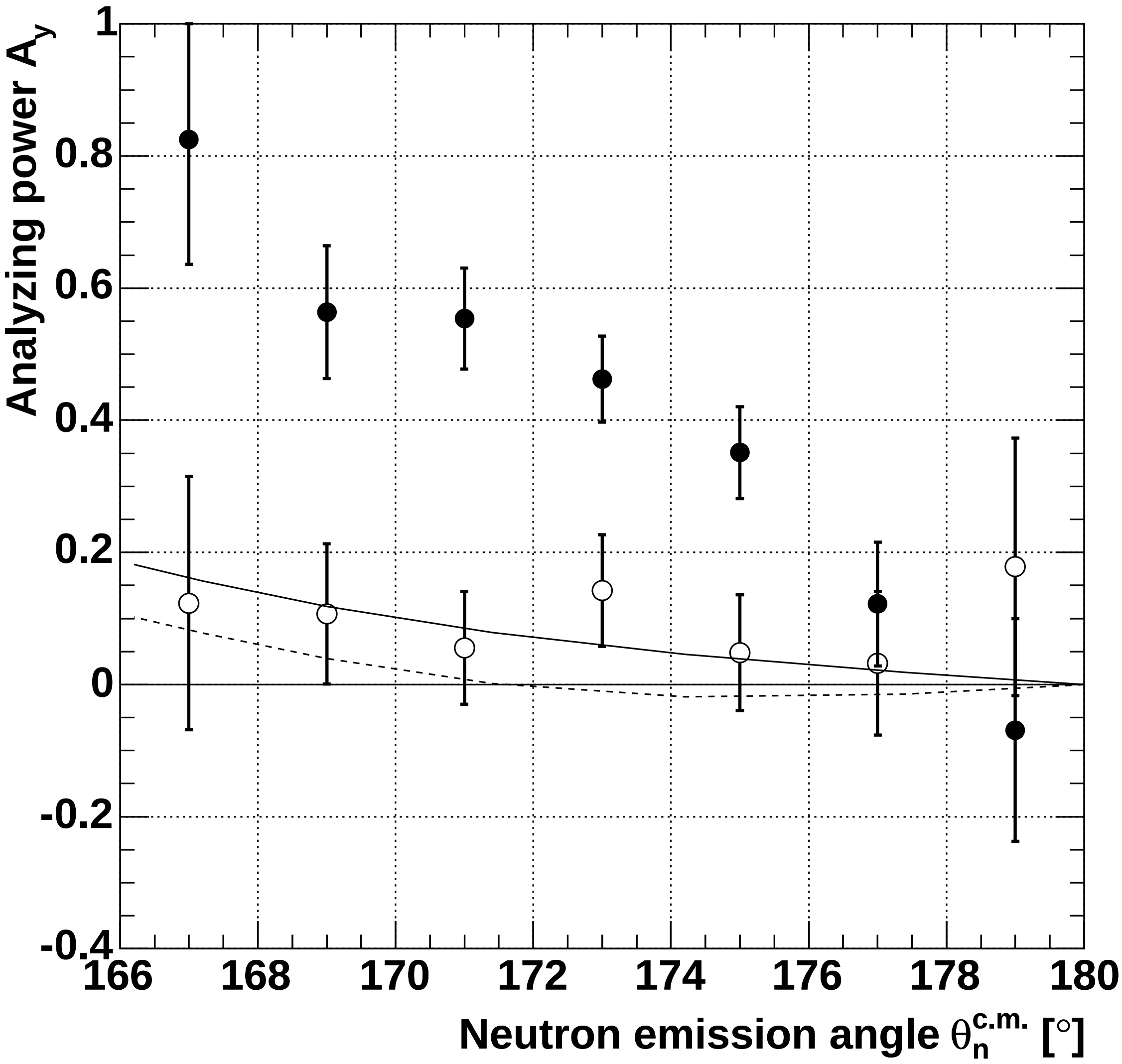

Figure 5.13: Angular dependence of the analyzing power at $T_p = 0.5$ GeV (closed circles) and 0.8 GeV (open circles) in $\vec{p}d \to (pp)n$. The solid line ($T_p = 0.5$ GeV) shows the ONE+SS+Δ model using the CD Bonn NN potential the dashed line is for $T_p = 0.8$ GeV.

6. Summary

A study of the deuteron breakup reaction $pd \to (pp)n$ with forward emission of a fast proton pair with small excitation energy $E_{pp} < 3$ MeV has been performed using the ANKE spectrometer at COSY–Jülich. The deuteron breakup process under such conditions has never been investigated experimentally before. An exclusive measurement was carried out by reconstructing the momenta of the two protons at six proton–beam energies $T_p = 0.6$, 0.7, 0.8, 0.95, 1.35, and 1.9 GeV with an unpolarized proton beam and at $T_p = 0.5$ and 0.8 GeV with a polarized beam. The differential cross section of the breakup reaction, averaged up to 8° over the c.m. polar angle of the total momentum of the pp pairs, has been obtained. The energy dependence of the differential cross section strongly contradicts predictions of a model based on the ONE, single pN scattering and Δ excitation mechanisms, and on the wave functions of the Reid soft core and Paris NN potentials. It was shown recently within the same model that for the CD Bonn NN potential there is qualitative agreement with the data [74]. The agreement is connected to a reduction of the one-nucleon exchange at energies above 1 GeV and an increase of the $\Delta(1232)$-isobar contribution, both related to short-range properties of the wave functions generated by this potential. In addition, experimental data at beam energies of 1.1, 1.4, and 2.0 GeV were collected during one week of beam time in July 2003. The data will allow us to obtain differential distributions of the cross section at these energies and to provide the energy dependence of the cross section with much better statistical accuracy. The analysis of these data is in progress.

In addition, the first experiment with a polarized proton beam at ANKE was carried out. The polarization measurement technique was developed by a simultaneous measurement of the asymmetry from small angle $\vec{p}d$ elastic scattering. The technique of on-line monitoring of the beam polarization was developed as well. The angular dependence of the analyzing power in the deuteron breakup $pd \to (pp)n$ was obtained in a 14° interval of the neutron emission angle (c.m.) below 180°. A large analyzing power was observed at 0.5 GeV and a value close to zero at 0.8 GeV. This differs qualitatively from the behavior of pd backward elastic scattering. The ONE+Δ+SS model reproduces the sign of A_y^p and its fast decrease towards the higher energy of $T_p = 0.8$ GeV, but fails to explain the large values of A_y^p at 0.5 GeV.

7. Outlook

A further critical test of the theoretical approach is expected from a measurement of the tensor analyzing power planned at ANKE. For such experiments a polarized internal target (PIT) is presently being prepared [28]. The PIT consists of a storage cell fed by an atomic beam source (ABS) [86] and a Lamb shift polarimeter (LSP) [87] for the measurement of the target polarization.

The development of the ABS for ANKE has been finalized. Beam intensities of 7.8×10^{16} hydrogen atoms per second in two hyperfine states have been reached with polarization of about 90%. For deuterium, where somewhat lower preliminary values have been reached until now, final tuning has to be carried out.

The LSP will be used to measure and monitor the nuclear polarization of the target gas by extracting a small fraction (about 10^{-4}) of the gas by a sample tube. The final development of the LSP itself has been performed with use of the direct ABS beam. With the full ABS beam intensity of 7.8×10^{16} $\vec{\mathrm{H}}$ atoms/s, the polarization of the PIT can be measured within 2 s with an accuracy better than 1%. At present studies are being performed with the LSP in a test setup employing feeding, storage, and sampling tubes made from teflon [88].

First storage cell tests at ANKE have been carried out to estimate the beam size at the ANKE target position since before these tests the size of the COSY beam at injection and after acceleration was rather uncertain. These findings are needed to design the storage cells for the polarized target and, depending on the size of the cells, determine how much beam will be lost at injection, and also to determine the target density. The cell tests will be continued in summer of 2004. At the same time a test experiment with all components of the PIT prior to installation at ANKE is planned.

A first commissioning experiment with PIT is planned within the framework of the deuteron breakup charge exchange study [36]. In the $dp \to (pp)n$ charge exchange reaction with small momentum transfer two protons with small excitation energy below 3 MeV have very similar kinematical parameters as in $pd \to (pp)n$ but the cross section of $dp \to (pp)n$ process is much higher. Such a commissioning experiment will allow us to investigate the experimental conditions for the future measurements of the tensor analyzing power and other polarization observables.

A. Kinematics of the $pd \rightarrow ppn$ Process

In this chapter the kinematics of the process $pd \rightarrow ppn$ is discussed. In order to describe a reaction with two initial particles and three particles in the final state ($A + B \rightarrow 1 + 2 + 3$) one has to define $3 \times (2 + 3)$ components of momenta. The momentum–energy conservation laws define four relations between momenta components of initial and final particles. In addition, the choice of c.m. system allows one to use three conditions for the initial particles $\boldsymbol{p}_A^{c.m.} + \boldsymbol{p}_B^{c.m.} = 0$ and three conditions for the particles in the final state $\boldsymbol{p}_1^{c.m.} + \boldsymbol{p}_2^{c.m.} + \boldsymbol{p}_3^{c.m.} = 0$. Therefore, the reaction is defined by $3 \times (2+3) - 4 - 3 - 3 = 5$ independent variables. For the description of the deuteron breakup reaction $pd \rightarrow (pp)n$ the following ones are used: excitation energy of the two protons E_{pp}, polar angle $\theta_{pp}^{c.m.}$ and azimuthal angle $\phi_{pp}^{c.m.}$ of proton pair in c.m. system, polar angle $\theta_k^{c.m.}$ and azimuthal angle $\phi_k^{c.m.}$ of the protons in the rest frame of the proton pair relative to the direction of the proton pair in c.m. system (Fig. A.1). The analyzing power is expressed in terms of the neutron scattering angle $\theta_n^{c.m.} = \pi - \theta_{pp}^{c.m.}$.

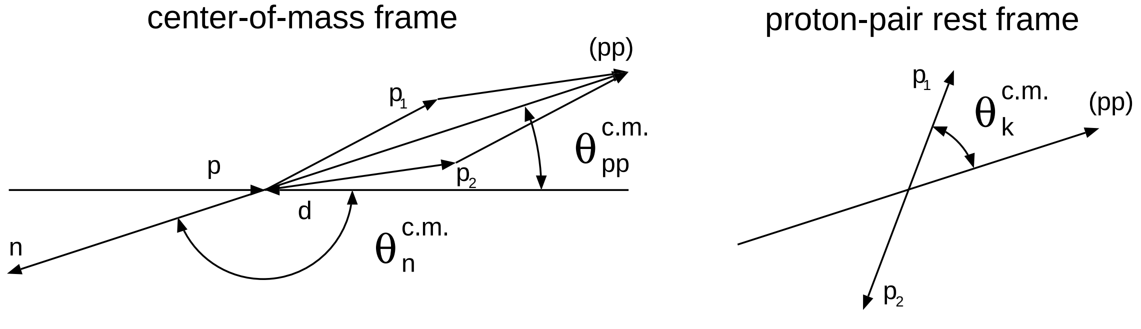

Figure A.1: Momentum vectors of reactions $pd \rightarrow (pp)n$ in the center–of–mass system and the rest frame of the two protons.

The excitation energy of the proton pair is defined as

$$E_{pp} = \sqrt{(E_{p_1} + E_{p_2})^2 - (\vec{p}_{p_1} + \vec{p}_{p_2})^2} - 2m_p,$$

where E_{p_1}, E_{p_2} are total energies and $\vec{p}_{p_1}$, $\vec{p}_{p_2}$ are the 3–momenta of the protons, m_p is the proton mass. The excitation energy E_{pp} is invariant under Lorentz transformation. From the measured 3–momenta of the two protons the missing mass of the neutron can be calculated from

$$M_{miss} = \sqrt{(E_p + m_d - E_{p_1} - E_{p_2})^2 - (\vec{p}_p - \vec{p}_{p_1} - \vec{p}_{p_2})^2}.$$

B. Polarization Observables in $\vec{p}\vec{d}$ Collisions

In this chapter the polarization observables of the type $\vec{\frac{1}{2}} + \vec{1}$ are discussed [77].

A single particle with spin $\frac{1}{2}$ can be represented by a Pauli spinor

$$\chi = \begin{pmatrix} a_1 \\ a_2 \end{pmatrix}.$$

The expectation value of an observable corresponding to a particular hermitian operator Ω is

$$\langle \Omega \rangle = \chi^{\dagger} \Omega \chi \equiv (a_1^* a_2^*) \left(\begin{array}{cc} \Omega_{11} & \Omega_{12} \\ \Omega_{12}^* & \Omega_{22} \end{array} \right) \begin{pmatrix} a_1 \\ a_2 \end{pmatrix} = |a_1|^2 \Omega_{11} + |a_2|^2 \Omega_{22} + 2Re\Omega_{12} a_1 a_2^*.$$

The density matrix is defined as

$$\rho = \left(\begin{array}{cc} |a_1|^2 & a_1 a_2^* \\ a_2 a_1^* & |a_2|^2 \end{array} \right),$$

resulting in

$$\langle \Omega \rangle = \mathrm{Tr} \rho \Omega.$$

If one considers an ensemble of N particles, the ensemble average of the expectation value of the operator Ω, denoted by $\overline{\langle \Omega \rangle}$, is

$$\overline{\langle \Omega \rangle} = \sum_{n=1}^{N} \chi^{\dagger (n)} \Omega \chi^{(n)},$$

where the spinor for the nth particle is

$$\chi^{(n)} = \begin{pmatrix} a_1^{(n)} \\ a_2^{(n)} \end{pmatrix}.$$

This can be written as

$$\overline{\langle \Omega \rangle} = \mathrm{Tr} \rho \Omega, \text{ where } \rho = \frac{1}{N} \left(\begin{array}{cc} \sum_{n=1}^{N} |a_1^{(n)}|^2 & \sum_{n=1}^{N} a_1^{(n)} a_2^{(n)*} \\ \sum_{n=1}^{N} a_2^{(n)} a_1^{(n)*} & \sum_{n=1}^{N} |a_2^{(n)}|^2 \end{array} \right).$$

The state of polarization of the ensemble is specified by the Pauli spin operators σ_x, σ_y and σ_z:

$$\sigma_x = 2S_x = \begin{pmatrix} 0 & 1 \\ 1 & 0 \end{pmatrix}$$

$$\sigma_y = 2S_y = \begin{pmatrix} 0 & -i \\ i & 0 \end{pmatrix}$$

$$\sigma_z = 2S_z = \begin{pmatrix} 1 & 0 \\ 0 & -1 \end{pmatrix}$$

where S_x, S_y and S_z are the spin $\frac{1}{2}$ angular momentum operators. The expectation values are

$$p_x \equiv \langle \sigma_x \rangle = \mathrm{Tr}\rho\sigma_x = \frac{1}{N}\sum_{n=1}^{N} 2\mathrm{Re}(a_1^{(n)} a_2^{(n)*})$$

$$p_y \equiv \langle \sigma_y \rangle = \mathrm{Tr}\rho\sigma_y = \frac{1}{N}\sum_{n=1}^{N} 2\mathrm{Im}(a_1^{(n)} a_2^{(n)*})$$

$$p_z \equiv \langle \sigma_z \rangle = \mathrm{Tr}\rho\sigma_z = \frac{1}{N}\sum_{n=1}^{N} (|a_1^{(n)}|^2 - |a_2^{(n)}|^2).$$

The expectation value of the unit matrix

$$I = \begin{pmatrix} 1 & 0 \\ 0 & 1 \end{pmatrix}$$

gives the normalization of the density matrix,

$$I = \mathrm{Tr}\rho = \frac{1}{N}\sum_{n=1}^{N} (|a_1^{(n)}|^2 + |a_2^{(n)}|^2) = 1.$$

The set of operators I, σ_x, σ_y, σ_z forms a complete set of hermitian matrices for the 2×2 space. Thus, a specification of the quantities p_x, p_y, p_z is a complete description of the polarization of the ensemble.

The spin $\frac{1}{2}$ density matrix, being hermitian, can itself be expanded in terms of the set of matrices I, σ_x, σ_y, σ_z:

$$\rho = \frac{1}{2}(I + p_x\sigma_x + p_y\sigma_y + p_z\sigma_z) \equiv \frac{1}{2}\left(I + \sum_{j=1}^{3} p_j \sigma_j \right). \tag{B.1}$$

Let us consider the simple case of a reaction with the spin structure $\vec{\frac{1}{2}} + 0 \to \vec{\frac{1}{2}} + 0$. The spinor that describes the outgoing spin $\frac{1}{2}$ particle is related linearly to the spinor that describes the incoming spin $\frac{1}{2}$ particle,

$$\chi_f = M\chi_i,$$

where M is the scattering matrix containing all the information about the interaction. The density matrices describing the initial and final states may be written

$$\rho_i = \sum_{n=1}^{N} \chi_i^{(n)} [\chi_i^{(n)\dagger}], \qquad \rho_f = \sum_{n=1}^{N} \chi_f^{(n)} [\chi_f^{(n)\dagger}].$$

Hence,

$$\rho_f = M \rho_i M^\dagger. \tag{B.2}$$

If ρ is normalized to unity, the differential cross section for a polarized beam is given by

$$I(\theta, \phi) = \mathrm{Tr}\rho_f = \mathrm{Tr} M \rho_i M^\dagger.$$

For the unpolarized beam

$$\rho_i = \frac{1}{2} \begin{pmatrix} 1 & 0 \\ 0 & 1 \end{pmatrix} \qquad \text{and} \qquad I_0(\theta) = \frac{1}{2} \mathrm{Tr} M M^\dagger.$$

From equations 5.1 and 5.2 one finds

$$\rho_f = \frac{1}{2} M M^\dagger + \frac{1}{2} \sum_{j=1}^{3} p_j M \sigma_j M^\dagger.$$

This yields

$$I(\theta, \phi) = \mathrm{Tr}\rho_f = I_0(\theta) \left(1 + \sum_{j=1}^{3} p_j A_j(\theta) \right),$$

where

$$A_j(\theta) = \frac{\mathrm{Tr} M \sigma_j M^\dagger}{\mathrm{Tr} M M^\dagger}$$

is the analyzing power of the reaction for the jth initial polarization component.

If the beam is made up of spin $\frac{1}{2}$ particles with transverse polarization $\vec{\boldsymbol{P}}$, the cross section for a reaction induced on an unpolarized target can be written

$$I(\theta, \phi) = I_0(\theta)(1 + A_y(\theta) \vec{\boldsymbol{P}} \vec{\boldsymbol{n}}) = I_0(\theta)(1 + A_y(\theta) |\vec{\boldsymbol{P}}| cos\phi),$$

where $I_0(\theta)$ is the cross section for scattering of an unpolarized beam at scattering angle θ, $A_y(\theta)$ is the analyzing power of the reaction, $\vec{n}$ is a unit vector along $\vec{\boldsymbol{k}}_{in} \times \vec{\boldsymbol{k}}_{out}$. The incident and scattered beams have momenta $\vec{\boldsymbol{p}}_{in} = \hbar \vec{\boldsymbol{k}}_{in}$ and $\vec{\boldsymbol{p}}_{out} = \hbar \vec{\boldsymbol{k}}_{out}$, respectively. The symbol ϕ denotes the angle between $\vec{\boldsymbol{P}}$ and $\vec{\boldsymbol{n}}$. This particular form of the cross section is a consequence of parity conservation in nuclear interactions.

The polarization analysis of a spin 1 particle is considerably more complicated than that for a spin $\frac{1}{2}$ particle. Here we present the general form of polarization observables $\vec{\frac{1}{2}} + \vec{1}$ of type without derivation. The most general form for the cross section in Cartesian coordinates for spin $\vec{\frac{1}{2}}$ (beam) + $\vec{1}$ (target) correlation experiments allowed by parity conservation is [77]

$$\begin{aligned} I = I_0(1 &+ p_yA_y + \frac{3}{2}p_xp_x^TC_{x,x} + \frac{3}{2}p_xp_z^TC_{x,z} + \frac{2}{3}p_xp_{xy}^TC_{x,xy} + \frac{2}{3}p_xp_{yz}^TC_{x,yz} \\ &+ \frac{3}{2}p_yp_y^TC_{y,y} + \frac{1}{3}p_yp_{xx}^TC_{y,xx} + \frac{2}{3}p_yp_{xz}^TC_{y,xz} + \frac{1}{3}p_yp_{yy}^TC_{y,yy} + \frac{1}{3}p_yp_{zz}^TC_{y,zz} \\ &+ \frac{3}{2}p_zp_x^TC_{z,x} + \frac{3}{2}p_zp_z^TC_{z,z} + \frac{2}{3}p_zp_{xy}^TC_{z,xy} + \frac{2}{3}p_zp_{yz}^TC_{z,yz} \\ &+ \frac{3}{2}p_y^TA_y^T + \frac{1}{3}p_{xx}^TA_{xx} + \frac{2}{3}p_{xz}^TA_{xz} + \frac{1}{3}p_{yy}^TA_{yy} + \frac{1}{3}p_{zz}^TA_{zz}), \end{aligned}$$

where p_i, p_i^T are the vector polarization of beam and target, respectively, p_{ij}^T is the tensor polarization of the target, A_i, A_{ij} are vector and tensor analyzing powers, $C_{i,j}$, $C_{i,jk}$ are spin correlation coefficients. In the case of unpolarized proton beam and longitudinally polarized deuterium target the spin–dependent cross section is

$$I = I_0(1 + \frac{1}{3}p_{zz}^TA_{zz}).$$

The relation between spherical and Cartesian analyzing powers is

$$\begin{aligned} iT_{11} &= \frac{\sqrt{3}}{2}A_y, \\ T_{20} &= \frac{1}{\sqrt{2}}A_{zz}, \\ T_{21} &= -\frac{1}{\sqrt{3}}A_{xz}, \\ T_{22} &= \frac{1}{2\sqrt{3}}(A_{xx} - A_{yy}). \end{aligned}$$

C. Acceleration of Polarized Proton Beams

In this chapter the acceleration of polarized proton beams, in particular at COSY, is discussed [89].

For an ideal planar circular accelerator with a vertical guide field, the particle spin vector precesses around the vertical axis. Thus the vertical beam polarization is preserved. The spin motion in an external electromagnetic field is governed by the Thomas–BMT equation [90], leading to a spin tune $\nu_{sp} = \gamma G$, which describes the number of spin precessions of the central beam per revolution in the ring. G is the anomalous magnetic moment of the particle, and $\gamma = E/m$ is the Lorentz factor. During acceleration of a polarized beam, depolarizing resonances are crossed if the precession frequency of the spin γG is equal to the frequency of the encountered spin–perturbing magnetic fields. In a strong–focusing synchrotron like COSY two different types of strong depolarizing resonances are excited, namely imperfection resonances caused by magnetic field errors and misalignments of the magnets, and intrinsic resonances excited by horizontal fields due to the vertical focusing.

In the momentum range of COSY, five imperfection resonances have to be crossed. The existing correction dipoles of COSY are utilized to overcome all imperfection resonances by exciting adiabatic spin flips without polarization losses. The number of intrinsic resonances depends on the superperiodicity of the lattice. The magnetic structure of COSY allows one to choose a superperiodicity of $P = 2$ or 6. A tune-jump system consisting of two fast quadrupoles has especially been developed to handle intrinsic resonances at COSY [89].

The imperfection resonances in the momentum range of COSY are listed in Table C.1. They are crossed during acceleration, if the number of spin precessions per revolution of the particles in the ring is an integer ($\gamma G = k, k$ is integer). The resonance strength depends on the vertical closed orbit deviation.

γG	T_p	p	y_{co}^{rms}	ϵ_r	P_f/P_i
	GeV	GeV/c	mm	10^{-3}	
2	0.1084	0.4638	2.3	0.95	-1.00
3	0.6318	1.2587	1.8	0.61	-0.88
4	1.1551	1.8712	1.6	0.96	-1.00
5	1.6785	2.4426	1.6	0.90	-1.00
6	2.2018	2.9964	1.4	0.46	-0.58

Table C.1: Resonance strength ϵ_r and the ratio of preserved polarization P_f/P_i at imperfection resonances for a typical vertical orbit deviation y_{co}^{rms}, without considering synchrotron oscillation.

A spin flip would occur at all resonances if synchrotron oscillation were not considered. However, the influence of synchrotron oscillation during resonance crossing cannot be neglected. At the first imperfection resonance, the calculated polarization with a momentum spread of $\Delta p/p = 1 \cdot 10^{-3}$ and a synchrotron frequency of $f_{syn} =$ 450 Hz is about $P_f/P_i \approx -0.85$. The resonance strength of the first imperfection resonance ($\gamma G = 2$) has to be enhanced to $\epsilon_r = 1.6 \cdot 10^{-3}$ to excite spin flips with polarization losses of less than 1%. At the other imperfection resonances the effect of synchrotron oscillation is smaller, due to the lower momentum spread at higher energies. Vertical correction dipoles or a partial snake can be used to preserve polarization at imperfection resonances by exciting adiabatic spin flips. Simulations indicate that an excitation of the vertical orbit with existing correction dipoles by 1 mrad is sufficient to adiabatically flip the spin at all imperfection resonances. In addition, the solenoids of the electron-cooler system inside COSY are available for use as a partial snake. They are able to rotate the spin around the longitudinal axis by about 8° at the maximum momentum of COSY. A rotation angle of less than 1° of the spin around the longitudinal axis already leads to a spin flip without polarization losses at all five imperfection resonances [91].

D. Comparison of $pd \to pX$ Cross Section Calculations with Data

The cross sections of pd forward scattering $pd \to pX$ were calculated [56] in the Glauber-Franko approximation. The pd scattering cross section consists of elastic and inelastic terms. The general expression of the cross-section was obtained in closure approximation, which includes the sum over the complete set of final pn states. In order to estimate the obtained accuracy, the cross sections, calculated for elastic scattering and inclusive $pd \to pX$ scattering within the same framework, were compared with the experimental data of Refs. [57, 58, 59, 60, 61] and [62] respectively, in the appropriate energy and angle ranges. The resulting $\chi^2/n.d.f.$=0.85 (n.d.f.=64) and $\chi^2/n.d.f.$=0.73 (n.d.f.=8), respectively, yield a 7% uncertainty of the cross section values used for the determination of the luminosity. In this chapter the results of this comparison are presented. For each angle θ_{lab} the χ^2 of the difference between calculated values of the cross section $d\sigma/d\Omega^{calc}_{c.m.}$ and the values from experimental data $d\sigma/d\Omega^{exp}_{c.m.}$ was calculated taking into account the statistical errors δ^{exp}_{stat} and the systematic uncertainties δ^{exp}_{syst} from the experimental data and the uncertainty of $\delta^{calc} = 7\%$ introduced for the theoretical calculations (Tables D.1 - D.6).

T_p [MeV]	θ_{lab} [°]	$d\sigma/d\Omega^{exp}_{c.m.}$ [mb/sr]	δ^{exp}_{stat} [%]	δ^{exp}_{syst} [%]	$d\sigma/d\Omega^{calc}_{c.m.}$ [mb/sr]	δ^{calc} [%]	χ^2
0.582	10.00	11.9	15.97	0	13.33	7	0.46
0.582	12.03	7.7	7.79	0	8.62	7	1.17
0.582	15.03	3.7	16.22	0	4.23	7	0.63
0.582	17.02	3.1	16.13	0	2.53	7	1.15

Table D.1: The comparison of the calculated cross section of pd elastic scattering with experimental data [57].

T_p [MeV]	θ_{lab} [°]	$d\sigma/d\Omega^{exp}_{c.m.}$ [mb/sr]	δ^{exp}_{stat} [%]	δ^{exp}_{syst} [%]	$d\sigma/d\Omega^{calc}_{c.m.}$ [mb/sr]	δ^{calc} [%]	χ^2
0.695	4.45	38.83	2	10	43.15	7	0.75
0.695	4.77	36.51	2	10	41.23	7	1.00
0.695	5.11	34.88	2	10	39.30	7	0.97
0.695	5.46	32.81	2	10	36.70	7	0.85
0.695	5.76	31.35	2	10	34.75	7	0.72
0.695	6.01	28.54	2	10	33.46	7	1.73
0.695	6.29	26.42	2	10	31.55	7	2.17
0.695	6.58	24.85	2	10	29.68	7	2.18
0.695	6.80	24.89	2	10	28.45	7	1.21
0.695	7.04	23.79	2	10	27.24	7	1.25
0.695	7.25	22.36	2	10	25.47	7	1.15
0.695	7.50	21.03	2	10	24.34	7	1.46
0.695	7.70	20.41	2	10	23.20	7	1.12
0.695	7.94	19.82	2	10	22.11	7	0.81
0.695	8.15	17.77	2	10	20.53	7	1.43
0.695	8.33	17.24	2	10	20.02	7	1.52
0.695	8.53	16.48	2	10	19.02	7	1.41
0.695	8.71	15.00	2	10	18.05	7	2.36
0.695	8.92	14.11	2	10	17.11	7	2.57

Table D.2: The comparison of the calculated cross section of *pd* elastic scattering with experimental data [58].

T_p [MeV]	θ_{lab} [°]	$d\sigma/d\Omega^{exp}_{c.m.}$	δ^{exp}_{stat} [%]	δ^{exp}_{syst} [%]	$d\sigma/d\Omega^{calc}_{c.m.}$	δ^{calc} [%]	χ^2
		[mb/sr]			[mb/sr]		
1.9958	5.17	28.2	5.32	7	27.6	7	0.04
1.9958	5.36	23.6	4.24	7	24.27	7	0.07
1.9958	6.52	11.3	4.42	7	11.34	7	0.001
1.9958	7.00	8.5	5.88	7	7.77	7	0.59
1.9958	7.48	5.7	8.77	7	5.21	7	0.44

Table D.3: The comparison of the calculated cross section of *pd* elastic scattering with experimental data [61].

T_p [MeV]	θ_{lab} [°]	$d\sigma/d\Omega^{exp}_{c.m.}$ [mb/sr]	δ^{exp}_{stat} [%]	δ^{exp}_{syst} [%]	$d\sigma/d\Omega^{calc}_{c.m.}$ [mb/sr]	δ^{calc} [%]	χ^2
0.796	4.84	42.30	0.77	3	44.71	7	0.51
0.796	5.13	39.56	0.83	3	41.94	7	0.56
0.796	5.40	37.56	0.76	3	39.23	7	0.32
0.796	5.67	35.96	0.61	3	36.62	7	0.06
0.796	5.92	34.58	0.63	3	34.93	7	0.016
0.796	6.16	32.16	0.68	3	32.48	7	0.017
0.796	6.39	30.41	0.64	3	30.91	7	0.04
0.796	6.62	29.32	0.67	3	29.39	7	0.001
0.796	6.83	27.07	0.73	3	27.92	7	0.16
0.796	7.04	25.89	0.76	3	26.50	7	0.09
0.796	7.25	24.64	0.71	3	24.80	7	0.007
0.796	7.44	22.92	0.76	3	23.80	7	0.24
0.796	7.64	22.13	0.79	3	22.55	7	0.06
0.796	7.83	20.58	0.85	3	21.34	7	0.22
0.796	8.02	19.51	0.78	3	20.18	7	0.19
0.796	8.20	18.48	0.83	3	19.96	7	0.96
0.796	8.38	17.63	0.87	3	18.00	7	0.07
0.796	8.55	16.78	0.91	3	16.98	7	0.024
0.796	8.72	15.97	0.96	3	16.50	7	0.18
0.796	8.88	14.88	0.88	3	15.50	7	0.28
0.796	9.05	14.53	0.90	3	14.64	7	0.01
0.796	9.21	13.65	0.96	3	14.20	7	0.25
0.796	9.37	12.96	1.01	3	13.36	7	0.16
0.796	9.53	12.23	1.07	3	12.96	7	0.54
0.796	9.68	11.78	1.11	3	12.18	7	0.19
0.796	9.83	11.12	1.18	3	12.80	7	3.03
0.796	9.98	10.62	1.03	3	11.08	7	0.30

Table D.4: The comparison of the calculated cross section of *pd* elastic scattering with experimental data [59].

T_p [MeV]	θ_{lab} [°]	$d\sigma/d\Omega^{exp}_{c.m.}$ [mb/sr]	δ^{exp}_{stat} [%]	δ^{exp}_{syst} [%]	$d\sigma/d\Omega^{calc}_{c.m.}$ [mb/sr]	δ^{calc} [%]	χ^2
1	5.48	57.8	10	3	42.14	7	5.44
1	5.94	45.9	10	3	37.62	7	2.29
1	7.15	27.9	10	3	26.08	7	0.28
1	7.43	22.5	10	3	23.66	7	0.16
1	7.54	20.9	10	3	22.9	7	0.55
1	8.04	16	10	3	19.36	7	2.44
1	8.48	18	10	3	16.28	7	0.61
1	10.31	9.61	10	3	9.35	7	0.05
1	10.70	7.54	10	3	7.10	7	0.23

Table D.5: The comparison of the calculated cross section of pd elastic scattering with experimental data [60].

T_p [MeV]	θ_{lab} [°]	$d\sigma/d\Omega^{exp}_{c.m.}$ [mb/sr]	δ^{exp}_{stat} [%]	δ^{exp}_{syst} [%]	$d\sigma/d\Omega^{calc}_{c.m.}$ [mb/sr]	δ^{calc} [%]	χ^2
0.956	2.46	5	50	10	7	7	0.59
0.956	4.27	30	8.33	10	23.8	7	2.13
0.956	5.52	51	5.88	10	43.2	7	1.38
0.956	6.54	62	4.84	10	61	7	0.015
0.956	7.82	74	5.41	10	80	7	0.35
0.956	8.36	80	6.25	10	85.5	7	0.24
0.956	8.79	101	4.95	10	90	7	0.73
0.956	9.00	101	4.95	10	95	7	0.21
0.956	10.24	101	4.95	10	95	7	0.21

Table D.6: The comparison of the calculated cross section of inclusive $pd \to pX$ scattering with experimental data [62].

Bibliography

[1] R. Gilman and F. Gross, J. Phys. **G 28** (2002) R37.

[2] M. Garcon and J. W. Van Orden, Adv. Nucl. Phys. **26** (2001), 293.

[3] A. K. Kerman, L. S. Kisslinger, Phys. Rev. **180** (1969) 1483.

[4] N. S. Craigie, C. Wilkin, Nucl. Phys. **B 14** (1969) 477.

[5] L. A. Kondratyuk, F. M. Lev, L. V. Shevchenko, Phys. Lett. **B 100** (1981) 448.

[6] Yu. N. Uzikov, Phys. Part. Nucl. **29** (1998) 583.

[7] A. Boudard, M. Dillig, Phys. Rev. **C 31** (1985) 302.

[8] J. Arvieux *et al.*, Nucl. Phys. **A 431** (1984) 613.

[9] L. S. Azhgirey *et al.*, Phys. Lett. **B 391** (1997) 22.

[10] M. Tanifuji, S. Ischikava, Y. Iseri, Phys. Rev. **C 57** (1998) 2493.

[11] V. M. Kolybasov, N. Ya. Smorodinskaya, Sov. J. Nucl. Phys. **17** (1973) 630.

[12] A. Nakamura, L. Satta, Nucl. Phys. **A 445** (1985) 706.

[13] O. Imambekov, Yu. N. Uzikov, L. V. Shevchenko, Z. Phys. **A 332** (1989) 349.

[14] O. Imambekov, Yu. N. Uzikov, Sov. J. Nucl. Phys. **47** (1988) 695.

[15] O. Imambekov, Yu. N. Uzikov, Sov. J. Nucl. Phys. **52** (1990) 862.

[16] A. V. Smirnov, Yu. N. Uzikov, Phys. Atom. Nucl. **61** (1998) 361.

[17] Yu. N. Uzikov, JETP Lett. **75** (2002) 5.

[18] Yu. N. Uzikov, J. Phys. G: Nucl. Part. Phys. **28** (2002) B13.

[19] Yu. N. Uzikov, ArXiv:nucl-th/0006067.

[20] V. Komarov *et al.* COSY Proposal #20 (1999), Spokespersons: V. Komarov, F. Rathmann.

[21] F. Bauer *et al.*, NIM **A 431** (1999) 385.

[22] R. Maier, NIM **A 390** (1997) 1.

[23] P. D. Eversheim *et al.*, The Polarized Ion–Source for COSY, Proc. International Symposium on High Energy Spin Physics SPIN 1996, Amsterdam (1996), published in World Scientific Singapore (1997).

[24] D. Prasuhn *et al.*, NIM **A 441** (2000) 167.

[25] D. Prasuhn *et al.*, Cooling at COSY, Workshop on Beam Cooling and Related Topics, Bad Honnef 2001, FZ Jülich, Matter and Material, V. **13**, ISBN 3-89336-316-5.

[26] S. Barsov *et al.*, NIM **A** 462 (2001) 364.

[27] A. Khoukaz *et al.*, Eur. Phys. J. **D 5** (1999) 275.

[28] F. Rathmann *et al.*, Proc. of the 15^{th} Int. Spin Physics Symposium, BNL, New York, 2002, AIP 0-7354-0136-5/03 (2003) 553.

[29] V. Koptev *et al.*, Phys. Rev. Lett. **87** (2001) 022301.

[30] M. Büscher *et al.*, NIM **A 481** (2002) 378.

[31] T. Kirchner *et al.*, COSY Proposal #21, 1996, spokesperson: H. Müller.

[32] M. Büscher *et al.*, COSY Proposal #104, 2001, spokesperson: M. Hartmann.

[33] V. Kleber *et al.*, Phys. Rev. Lett. **91** (2003) 172304.

[34] S. Barsov *et al.*, COSY Proposal #114, 2002, spokesperson: R. Schleichert.

[35] M. Büscher *et al.*, COSY Proposal #94, 2000, spokesperson: A. Khoukaz.

[36] A. Kacharava *et al.*, COSY proposal #125, spokespersons: A. Kacharava, F. Rathmann (2003).

[37] B. Chiladze *et al.*, Part. Nucl., Lett. **4** (2002) 95.

[38] S. Dymov *et al.*, Part. Nucl., Lett. **2** (2004) 40.

[39] R. Schleichert, A. Selikov, H. Seyfarth, IKP FZ–Jülich Annual Report 1995, Jül–3200, Jülich, 1996, p. 65.

[40] S. Dymov *et al.*, JINR Communication E10-2002-19, Dubna, 2002.

[41] V. Komarov, G. Macharashvili, IKP FZ–Jülich Annual Report 2000, Jül–3852, Jülich, 2001, p. 21.

[42] B. Zh. Zalikhanov *et al.*, IKP FZ–Jülich Annual Report 1993, Jül–2879, Jülich, 1994, p. 57.

[43] B. Zh. Zalikhanov *et al.*, IKP FZ–Jülich Annual Report 1995, Jül–3200, Jülich, 1996, p. 67.

[44] A. Yu. Petrus, B. Zh. Zalikhanov, NIM **A 485** (2002) 399.

[45] H. Kalmar *et al.*, NIM **A 307** (1991) 279.

[46] A. Yu. Petrus., JINR Communication E13-2002-14 (2002).

[47] G. Borchert *et al.*, IKP FZ–Jülich Annual Report 1997, Jül-3505, Jülich, 1998, p. 59.

[48] *GEANT – Detector Description and Simulation Tool.* CERN Program Library Long Writeup W5013.

[49] I. Lehmann *et al.*, to be published in NIM **A**.

[50] G. Riepe and D. Protić, NIM **A 226** (1984) 103.

[51] S. Dymov *et al.*, JINR Communication E10-2002-19, Dubna (2002).

[52] K. H. Watzlawik *et al.*, IEEE Trans. Nucl. Sci. **43** (1996) 44.

[53] A. D. Volkov *et al.*, NIM **A 306** (1991) 278.

[54] K. Hagiwara *et al.*, Phys. Rev. **D 66** (2002) 010001.

[55] V. Franco, R. J. Glauber, Phys. Rev. **142** (1966) 1195.

[56] Yu. Uzikov, IKP FZ-Jülich Annual Report 2001, Jül–3978, Jülich, 2002.

[57] E. T. Boschitz *et al.*, Phys. Rev. **C 6** (1972) 457.

[58] O. G. Grebenjuk *et al.*, Nucl. Phys. **A 500** (1989) 637.

[59] F. Irom *et al.*, Phys. Rev. **C 28** (1983) 2380.

[60] G. W. Bennet *et al.*, Phys. Rev. Lett. **19** (1967) 387.

[61] N. Dalkhazhav *et al.*, Sov. J. Nucl. Phys. **8** (1969) 196.

[62] B. S. Aladashvili *et al.*, J. Phys. **G 3** (1977) 7.

[63] S. Barsov *et al.*, to be published in EPJ **A**.

[64] J. C. Alder *et al.*, Phys. Rev. **C 6** (1972) 2010.

[65] E. Winkelmann *et al.*, Phys. Rev **C 21** (1980) 2535.

[66] K. M. Watson, Phys. Rev. **88** (1952) 1163;
A. B. Migdal, Sov. Phys. JETP **1** (1955) 2.

[67] V. Komarov *et al.*, Phys. Lett. **B 553** (2003) 179.

[68] L. Dubal et al., Phys. Rev. D 9 (1974) 597.

[69] A. Boudard, Thesis. CEA-N-2386, Saclay (1984).

[70] P. Berthet et al., J. Phys. G: Nucl. Phys. 8 (1982) L111.

[71] J. R. V. Reid, Ann. Phys. (NY) **50** (1968) 411.

[72] M. Lacombe *et al.*, Phys. Lett. **B 101** (1981) 139.

[73] According to Ref. [5] a coefficient of 0.8 in the ONE amplitude arising from the distortion of plane waves in the initial and final states is used to match the absolute value of the $pd \to dp$ cross section at $T_p < 0.3$ GeV.

[74] J. Haidenbauer, Yu. N. Uzikov, Phys. Lett. **B 562** (2003) 227.

[75] R. Machleidt, Phys. Rev. **C 61** 024001 (2001).

[76] L. Kaptari *et al.*, ArXiv:nucl-th/0212062.

[77] G. G. Ohlsen, Rep. Prog. Phys. **35** (1972) 717.

[78] R. Gebel, private communication.

[79] R. C. Hanna, In Proc. of the 2nd International Symp. on Polarization Phenomena of Nucleons., Karlsruhe 1965, ed. P. Huber, H. Schopper. p 280.

[80] R. E. Pollock *et al.*, Phys. Rev. **E 55**, 7606 (1997).

[81] M. L. Barlett *et al.*, Phys. Rev. **C 27**, N2 (1983) 682.

[82] www.said-hh.desy.de.

[83] N. E. Booth *et al.*, Phys. Rev. **D 4** (1971) 1261.

[84] E. Biegert *et al.*, Phys. Rev. Lett. **41** (1978) 1098.

[85] Yu. N. Uzikov, private communication.

[86] M. Mikirtytchiants *et al.*, in Proceedings of th 9th International Workshop on Polarized Sources and Targets (PST01), Nashville, edited by V.P. Derenchuk and B. Przhewoski (World Scientific, Singapore, 2002), p. 47.

[87] R. Engels *et al.*, Rev. Sci. Instr. **74** (2003) 4607.

[88] R. Engels *et al.*, IKP FZ–Jülich Annual report 2003, Jül–4107, Jülich, 2004.

[89] A. Lehrach *et al.*, Proc. of the 15^{th} Int. Spin Physics Symposium, BNL, New York, 2002, AIP 0-7354-0136-5/03 (2003) 153.

[90] L. H. Thomas, Phil. Mag. **3** (1927) 1; V. Bargman, L. Michel, V. L. Telegdi, Phys. Rev. Lett. **2** (1959) 43.

[91] A. Lehrach *et al.*, Status of the polarized beam at COSY, Proc. International Symposium on High Energy Spin Physics SPIN 1996, Amsterdam (1996), published in World Scientific Singapore (1997).

Acknowledgments

I would like to thank:

- Prof. Dr. E. Steffens for providing the possibility to work on PhD in the ANKE collaboration and to participate in interesting conferences, and for the consent to act as the referee,
- Prof. Dr. H. Ströher for the consent to act as the co–referee and for the good working atmosphere in IKP at FZ–Jülich,
- Prof. Dr. M. Dillig, Prof. Dr. U. Heber, Prof. Dr. U. Katz, and Prof. Dr. E. Steffens for the consent to act as the examiners,
- Dr. F. Rathmann for the permanent interest to this work, fruitful discussions and advises,
- Prof. Dr. V. Komarov for the interest to all details of the work, helpful advises and discussions,
- Dr. Yu. Uzikov for the theoretical motivation of our experimental studies,
- Drs. S. Dymov and G. Macharashvili for the large contribution to the data analysis,
- Dr. H. Seyfarth for the useful advises and help to solve any problems,
- Dr. A. Kacharava, Prof. Dr. V. Komarov, Dr. A. Kulikov, Dr. G. Macharashvili, Dr. F. Rathmann, Dr. H. Seyfarth, Dr. Yu. Uzikov, Prof. Dr. C. Wilkin for careful reading of the manuscript and useful corrections and comments,
- Drs. S. Barsov, I. Lehmann, S. Merzliakov, A. Mussgiller, and R. Schleichert for the development and perfect operation of the spectator detector telescope,
- COSY team for the high quality polarized and unpolarized beams,
- Drs. A. Khoukaz, N. Lang, and T. Mersmann for the stable target operation,
- All members of the ANKE collaboration for providing the detector, hardware and software operations during the beam times,
- Frau E. Haßler for taking care of all formalities connected with my travels, contracts, and examination,

and last but not least:

- My family for the permanent moral support.

Publikationen

- S. Yaschenko *et al.*, *"Experimental Results on the $pd \to (pp)_s + n$ Cross Sections from ANKE"*, talk at the 4th ANKE Workshop on Proton–Deuteron Interaction Studies, JINR, Dubna, Russia, July 9, 2002, published in Berichte des FZ–Juelich, Jül–4012, ISSN 0944–2952.

- S. Yaschenko, *"Current Possibilities for pd-study with Polarized Proton Beam"*, talk at the 4th ANKE Workshop on Proton–Deuteron Interaction Studies, JINR, Dubna, Russia, July 9, 2002, published in Berichte des FZ–Juelich Jül–4012, ISSN 0944–2952.

- V. Komarov *et al.*, *"Proton–Induced Deuteron Breakup at GeV Energies with Forward Emission of a Fast Proton Pair"*, Phys. Lett. **B 553** (2003) 179.

- S. Yaschenko *et al.*, *"Deuteron Breakup at High Momentum Transfer: First Experimental Results from ANKE at COSY and Development of Polarized Internal Gas Target"*, The 17th International IUPAP Conference on Few-Body Problems in Physics, Durham, North Carolina, USA June 5 - 10, 2003, to be published in Nucl. Phys. A.

Lebenslauf

Name:	**Sergey Yashchenko**
Geburtsdatum:	22 Mai 1971
Geburtsort:	Wolgograd, Russland
Staatsangehörigkeit:	Russisch
Eltern:	Ludmila Yashchenko, geboren Fedotova, Krankenschwester Vladimir Yashchenko, Baumeister
Familienstand:	Verheiratet, 1 Kind
Schulausbildung: 1878 – 1988	 Schule N 17, Wolgograd, Russland
Hauptstudium: 1988 – 1994	Moscow Ingeneering Physics Institute (Technical University) Wahlpflichtfächer: Experimental Kernphysik und Plasmaphysik
Diplom: 1993 – 1994	Joint Institute for Nuclear Research, Dubna, Russland “Anwendung phisikalischer Prozesse für die Entwicklung von Methoden zur Bestimmung des Impulses geladener Teilchen”
Ab April 1994	Wissenschaftlischer Angestellter an der Joint Institute for Nuclear Research, Dubna, Russland
Promotion: Ab Mai 2001	Friedrich–Alexander–Universität Erlangen–Nürnberg “Deuteron Breakup $\vec{p}d \rightarrow ppn$ with a Fast Forward Diproton Studied at ANKE–COSY”